VOLUME 39 FEBRUARY 1961 NUMBER 2

Canadian Journal of Physics

Published by THE NATIONAL RESEARCH COUNCIL

OTTAWA CANADA

CANADIAN JOURNAL OF PHYSICS

Under the authority of the Chairman of the Committee of the Privy Council on Scientific and Industrial Research, the National Research Council issues THE CANADIAN JOURNAL OF PHYSICS and five other journals devoted to the publication, in English or French, of the results of original scientific research. Matters of general policy concerning these journals are the responsibility of a joint Editorial Board consisting of: members representing the National Research Council of Canada; the Editors of the Journals; and members representing the Royal Society of Canada and four other scientific societies.

Manuscripts for publication should be submitted to Dr. H. E. Duckworth, Editor, Canadian Journal of Physics, Hamilton College, McMaster University, Hamilton, Ontario.
For instructions on preparation of copy, see **NOTES TO CONTRIBUTORS** (back cover).

Proof, correspondence concerning proof, and orders for reprints should be sent to the Manager, Editorial Office (Research Journals), Division of Administration and Awards, National Research Council, Ottawa 2, Canada.

Subscriptions, renewals, requests for single or back numbers, and all remittances should be sent to Division of Administration and Awards, National Research Council, Ottawa 2, Canada. Remittances should be made payable to the Receiver General of Canada, credit National Research Council.

The journals published, frequency of publication, and subscription prices are:

Canadian Journal of Biochemistry and Physiology	Monthly	$9.00 a year
Canadian Journal of Botany	Bimonthly	$6.00 a year
Canadian Journal of Chemistry	Monthly	$12.00 a year
Canadian Journal of Microbiology	Bimonthly	$6.00 a year
Canadian Journal of Physics	Monthly	$9.00 a year
Canadian Journal of Zoology	Bimonthly	$5.00 a year

The price of regular single numbers of all journals is $2.00.

Canadian Journal of Physics

Issued by THE NATIONAL RESEARCH COUNCIL OF CANADA

VOLUME 39 FEBRUARY 1961 NUMBER 2

THE EXTENSION OF HOUSTON'S METHOD WITH APPLICATION TO DEBYE Θ_0[1]

D. D. BETTS

ABSTRACT

Houston's method of integration over the unit sphere of functions of cubic symmetry is extended by developing integration formulas using 9 and 15 values of the integrand. The 3-, 6-, 9-, and 15-term Houston formulas are used to calculate Debye Θ_0 values for a number of cubic crystals. The convergence of the results is excellent except for the most anisotropic crystals.

INTRODUCTION

Houston (1948) proposed a method for integrating functions of complete cubic symmetry (corresponding to the identity representation of the point group O_h) over the unit sphere using only three appropriately weighted values of the integrand. Further such formulas using up to 6 values of the integrand have been presented by Betts, Bhatia, and Wyman (1956) and used to compute Debye Θ_0 values. Formulas for hexagonal, trigonal, and tetragonal symmetries have also been presented and used by Betts, Bhatia, and Horton (1956). Here we report on a further extension of Houston's method for cubic crystals, motivated on the one hand by the "good" Θ_0 values obtained using the 6-term formula for most crystals and on the other hand by the still uncertain values obtained for the elastically very anisotropic alkali metals.

DETERMINATION OF THE INTEGRATION FORMULAS

Suppose $I(\theta,\phi)$ has complete cubic symmetry and we require

$$J = \int_0^{2\pi} d\phi \int_0^{\pi} \sin\theta \, d\theta \, I(\theta,\phi). \tag{1}$$

Houston's method consists in expanding $I(\theta,\phi)$ in the Kubic Harmonics of Von der Lage and Bethe (1947) having the same symmetry, which we denote by $K_{lm}(\theta,\phi)$

$$I = \sum_{l,m} A_{lm} K_{lm}. \tag{2}$$

[1]Manuscript received October 3, 1960.
Contribution from the Department of Physics, University of Alberta, Edmonton, Alta.

The degree of the polynomial is $2l$ when expressed as is usual in terms of x, y, and z, the direction cosines of θ and ϕ; m distinguishes K's of the same degree.

As all the other K_{lm} are orthogonal over the sphere to $K_0 = 1$ the integral (1) becomes $J = 4\pi A_{00}$.

In practice the series (2) uses only a small number of polynomials up to a certain degree, $2L$. Then in (2) N special pairs of values of θ and ϕ (or N directions) are chosen for evaluating I and the K's. The resulting N equations determine the N unknowns A_{lm}. In particular A_{00} will be of the form

$$A_{00} = \sum_{i=1}^{N} w_i I(\theta_i, \phi_i). \tag{3}$$

For example Houston's original 3-term formula is

$$35A_{00}^{(3)} = 10I(100)+16I(110)+9I(111). \tag{4}$$

The further formulas of Betts, Bhatia, and Wyman (1956) use values of the integrand in the 210, 211, and 221 directions, culminating in the formula

$$\begin{aligned} 1081{,}080\,A_{00}^{(6)} = {} & 117{,}603I\,(100)+76{,}544I\,(110)+17{,}496I\,(111) \\ & +381{,}250I\,(210)+311{,}040I\,(211)+177{,}147I\,(221). \end{aligned} \tag{5}$$

A natural way of choosing further directions in extending the method appears from examination of the plane projection of 1/48th of the unit sphere shown in Fig. 1. The procedure is to divide the large triangle into smaller and

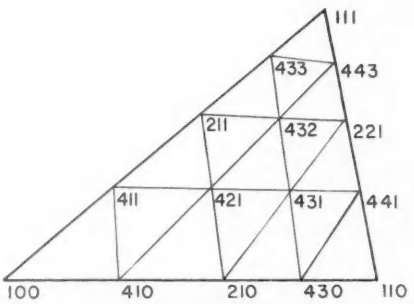

FIG. 1. Distribution over 1/48th of the unit sphere of points for evaluation of the integrand for use in Houston-type integration formulas.

smaller triangles each time using all the corner points. Thus the first approximation is formula (4), the third the 6-term formula (5) where the triangle is divided into four nearly similar triangles. Taking three further directions (411), (431), and (433) divides the original triangle into eight smaller triangles to give a 9-term approximation. Finally we obtain a 15-term approximation, by including the additional directions (410), (411), (430), (421), (432), and (443). The resulting formulas are

$$A_{00}^{(9)} = 0.05637817I\,(100)+0.04952710I\,(110)$$
$$-0.05588614I\,(111)+0.17827058I\,(210)$$
$$+0.10294771I\,(211)+0.07309875I\,(221)$$
$$+0.20711638I\,(411)+0.21376348I\,(431)$$
$$+0.17478397I\,(433) \tag{6}$$

$$A_{00}^{(15)} = +0.0436705I\,(100)+0.0229221I\,(410)$$
$$+0.3400264I\,(210)-0.8133145I\,(430)$$
$$+0.9623617I\,(110)+0.2285255I\,(411)$$
$$-0.5323867I\,(421)+2.2314783I\,(431)$$
$$-1.9823060I\,(441)+0.8005275I\,(411)$$
$$-3.2370533I\,(432)+2.3075765I\,(221)$$
$$+2.5033260I\,(433)-1.7484174I\,(443)$$
$$-0.1269366I\,(111). \tag{7}$$

The weights, w_i, in (6) and (7) had to be found approximately by inversion of the matrix of K's on the University of Alberta's LGP-30 electronic digital computer.* The inverses were checked by multiplication of the calculated inverses by the original matrices, and the entries in the top row of the product matrix were found to be unity or zero respectively to at least six decimal figures. Thus the weights can be regarded as correct to seven figures.

APPLICATIONS

It is well known that Houston-type formulas can be used to calculate Θ_0, the Debye characteristic temperature at 0° K. They have also been used by Horton and Schiff (1958) to calculate the coefficient B_2 in the low-temperature expansion of the Debye Θ given by

$$\Theta_T = \Theta_0 \sum_n B_{2n}(T/\Theta_0)^{2n} \tag{8}$$

and by Horton (1960) to calculate an average Grüneisen γ in the theory of thermal expansion of solids. Although the tables of de Launay (1956) provide an accurate and quick way of computing Debye Θ_0, they are not applicable to the calculation of any other physical quantities.

*Actually the completely orthogonalized K's need not be used but only polynomials of the form

$$k_{lmn} = x^{2l}y^{2m}z^{2n}+x^{2m}y^{2n}z^{2l}+x^{2n}y^{2l}z^{2m}+x^{2l}y^{2n}z^{2m}+x^{2m}y^{2l}z^{2n}+x^{2n}y^{2m}z^{2l}-b_{lmn}$$

where b_{lmn} is chosen to make the integral of k_{lmn} over the unit sphere vanish. The number of k's of a given degree to be used is determined by formula (A.10) of Betts, Bhatia, and Wyman (1956). The evaluation of the b's is trivial. The latter polynomials were the ones used to calculate formula (7).

TABLE I

Debye Θ_0 for four degrees of approximation

Substance	Density (g/cm^3) ρ	Elastic constants[a] (10^{11} dynes/cm^2) C_{11}	C_{12}	C_{44}	Anisotropy $\eta = \frac{2C_{44}}{C_{11}-C_{12}}$	Debye Θ_0's (° K) $\Theta_0^{(3)}$	$\Theta_0^{(6)}$	$\Theta_0^{(9)}$	$\Theta_0^{(15)}$
Potassium chloride	1.984	3.98	.62	.625	.372	216.8	222.8	223.6	
Galena	7.45	12.7	2.98	2.48	.511	226.44	229.45	229.70	
Silver chloride	5.56	6.01	3.62	.625	.523	143.50	145.77	145.99	
Barium nitrate	3.24	6.02	1.86	1.21	.571	286.81	289.41	289.58	
Silver bromide	6.473	5.62	3.28	.728	.622	134.43	135.57	135.64	
Thallium bromide	7.577	3.78	1.48	.756	.657	114.18	114.83	114.86	
Molybdenum	9.01	45.5	17.6	11	.788	466.62	467.45	467.47	
Strontium nitrate	2.986	4.73	2.18	1.46	1.145	303.54	303.714	303.712	
Aluminum*[b]	2.7365	12.3	7.08	3.09	1.190	427.776	428.205	428.197	
Magnesium oxide	3.58	28.6	8.7	14.8	1.44	917.47	920.89	920.79	
Lithium fluoride	2.601	11.9	4.58	1.297	1.48	682.83	685.63	685.54	
Diamond	3.52	95	39	43	1.54	1862.2	1871.6	1871.2	
Silicon	2.42	16.76	6.51	8.008	1.56	640.86	644.21	644.10	
Germanium	5.46	13.1	4.9	6.877	1.68	370.51	372.99	372.900	372.910
Zinc blende	4.102	10	6.5	3.4	1.94	305.55	310.30	310.03	
Nickel	8.75	24.36	14.95	11.96	2.30	438.5	450.8	450.0	
Gold*[c]	19.32	20.17	16.97	45.5	2.84	155.2	162.6	162.00	162.07
Copper*[c]	8.99	17.62	12.49	8.177	3.19	329.8	345.7	344.49	344.54
Silver*[c]	10.5	13.16	9.731	5.117	3.61	218.0	227.9	227.11	227.13
Lead†	11.34	4.8	4.1	1.4	4.00	82.97	89.96	89.365	89.350
Lithium[d]	.53	1.53	1.19	1.33	7.81	324	376	372	368
Sodium[d]	.97	.972	.829	.579	8.15	129	153	151	149

*Elastic constants for these substances were measured at 0° K.

†Extrapolated to 0° K. See Horton and Schiff (1958).

[a]Unless otherwise indicated elastic constants are obtained from the review article of Hearmon (1956). Often the values are averages of values by several workers. In all cases enough zeros were added in the calculation to give 8-figure values for the elastic constants and densities.

[b]Sutton (1953).

[c]Neighbours and Alers (1958).

[d]Blackman (1938).

We have used here formulas (4)–(6) to calculate successive approximations $\Theta_0^{(3)}$, $\Theta_0^{(6)}$, and $\Theta_0^{(9)}$ for 22 crystalline solids from the well-known formula of Debye

$$\Theta_0 = \frac{h}{k}\left(\frac{9}{4\pi}\frac{\rho}{MA_{00}}\right)^{1/3} \tag{9}$$

where h and k are Planck's and Boltzmann's constants, ρ is the density, and M the average mass of an atom of the substance. A_{00} is the average over the unit sphere of

$$I(\theta, \phi) = \sum_{i=1}^{3} \{v_i(\theta, \phi)\}^{-3} \tag{10}$$

where v_i are the elastic wave velocities. For seven of these substances including the most anisotropic we have also calculated the 15-term approximation, $\Theta_0^{(15)}$. Table I contains the results.

As a further check on the formulas (4)–(7) we have calculated approximately the integral

$$\Delta = \int_0^{2\pi} d\phi \int_0^{\pi} \sin\theta\, d\theta\, (\arcsin^2 x + \arcsin^2 y + \arcsin^2 z) \tag{11}$$
$$= 3\pi(\pi^2 - 8).$$

The results are presented in Table II.

TABLE II

Approximations to $\Delta = \int_0^{2\pi} d\phi \int_0^{\pi} \sin\theta\, d\theta x$ [arc $\sin^2 x$ + arc $\sin^2 y$ + arc $\sin^2 z$]

i (number of values of integrand used)	$\Delta^{(i)}$
3	19.619
6	18.096
9	17.797
15	17.739
Exact	17.621

DISCUSSION AND CONCLUSIONS

For substances with anisotropies from .5 to 2.0 the $\Theta_0^{(6)}$ and $\Theta_0^{(9)}$ approximations to Θ_0 agree to closer than 1/10th of a per cent. Hence we did not, in general, bother for such substances to calculate $\Theta_0^{(15)}$. For germanium, however, with $\eta = 1.68$, $\Theta_0^{(9)}$ and $\Theta_0^{(15)}$ agree to one part in the fifth figure. Even for such an anisotropic substance as lead $\Theta_0^{(9)}$ and $\Theta_0^{(15)}$ agree to better than two one-hundredths of a per cent. It is somewhat disappointing to see then that for sodium and lithium the 9-term approximation is no closer to the 15-term approximation than to the 6-term one. Probably a tremendously large number of terms in the harmonic expansion of $I(\theta,\phi)$ in these cases are needed to represent the function accurately.

Table II shows the satisfactory convergence of Houston's method for integration of a function whose series expansion is known to converge very slowly and for which the exact value of the integral is known.

We conclude that the present extension of Houston's method provides sufficiently accurate integration formulas for computing Debye Θ_0 of all substances but alkali metals. Although it would not be difficult to extend the method systematically to still higher degrees of approximation it is doubtful if the labor is worth while. The formulas may of course be used for the precise integration over the unit sphere of any function of complete cubic symmetry.

ACKNOWLEDGMENTS

The author would like to thank the staff of the Computation Center at the University of Alberta for carrying out the numerical work, in particular Messrs. A. Cseuz, P. Buckley, and D. Hunter. The author would also like to thank the National Research Council of Canada for financial assistance.

REFERENCES

BETTS, D. D., BHATIA, A. B., and HORTON, G. K. 1956. Phys. Rev. **104**, 42.
BETTS, D. D., BHATIA, A. B., and WYMAN, M. 1956. Phys. Rev. **104**, 37.
BLACKMAN, M. 1938. Proc. Roy. Soc. (London), A, **164**, 62.
HEARMON, R. F. S. 1956. Phil. Mag. Suppl. **5**, 323.
HORTON, G. K. 1960. To be published.
HORTON, G. K. and SCHIFF, H. 1958. Can. J. Phys. **36**, 1127.
HOUSTON, W. V. 1948. Revs. Modern Phys. **20**, 161.
VON DER LAGE, F. C. and BETHE, H. A. 1947. Phys. Rev. **71**, 612.
DE LAUNAY, J. 1956. Solid state physics, Vol. 2 (Academic Press, New York), p. 219.
NEIGHBOURS, J. R. and ALERS, G. A. 1958. Phys. Rev. **111**, 707.
SUTTON, P. M. 1953. Phys. Rev. **91**, 816.

ASYMMETRY IN THE RECOVERY FROM A VERY DEEP FORBUSH-TYPE DECREASE IN COSMIC-RAY INTENSITY[1]

D. C. Rose and S. M. Lapointe[2]

ABSTRACT

The intensity–time curves for cosmic rays recorded at some 30 stations distributed all over the world are examined for structure in the recovery period from the third in a series of three closely spaced Forbush-type decreases which occurred in the middle of July 1959. It is shown that the structure of intensity peaks is regular and that these occur at each station at the same effective local time. It is found that this is consistent with the hypothesis that recovery from a very deep Forbush-type decrease is first apparent in directions making 15° and 165° with the sun–earth line respectively. The analyses suggest further, that during recovery from this deep Forbush decrease temporary openings appeared in the intensity depressing mechanism which allowed intensity increases in limited directions.

I. INTRODUCTION

In the middle of July 1959 there occurred in close succession three large Forbush-type decreases. The complete intensity curves for that period at the six stations—Ottawa, Sulphur Mountain, Churchill, and Resolute, operated by the National Research Council of Canada; Deep River, operated by Atomic Energy of Canada Limited; and Thule, operated in close co-operation with the Canadian stations by the Bartol Research Foundation—have already been published (Carmichael and Steljes 1959; Wilson, Rose, and Pomerantz 1960). The first large Forbush decrease occurred on July 11 followed by a very slow recovery. Before recovery to the pre-event level a second decrease occurred on July 15. This was followed by an unusually rapid increase which has been interpreted by Steljes and Carmichael (1960) as a beam of solar injected particles. After this event, late on July 17, there occurred a third Forbush decrease bringing the intensity down to a very low point indeed. The recovery from this last decrease reveals some interesting structure. Among other features, attention has already been called to a peak in the hourly values of the intensity early on July 18 and marked D in the curves shown by Wilson, Rose, and Pomerantz (1960) and similarly marked in Fig. 1 of this paper. We would like here to attempt a detailed analysis of this peak and following events (E and F, Fig. 1) making use of data from a large number of stations.* This analysis will be limited mostly to variations in the nucleonic component of cosmic rays as measured by standard neutron monitors of the type designed for the International Geophysical Year.

[1]Manuscript received November 15, 1960.
Contribution from the Division of Pure Physics, National Research Council, Ottawa, Canada.
Issued as N.R.C. No. 6133.

[2]Department of Physics, University of Montreal, Montreal, Quebec.

*The data from about 30 stations in all were used. These data were obtained in most cases directly from the laboratories concerned by data exchange arrangements during the I.G.Y. and I.G.C. Carmichael and Steljes made a world-wide collection of data for this event and since our analysis of this event was carried out in close co-operation with them, in a few cases where we did not have the data ourselves their collection was used. In the final paragraph of this paper we have expressed appreciation to our many colleagues for making these data available.

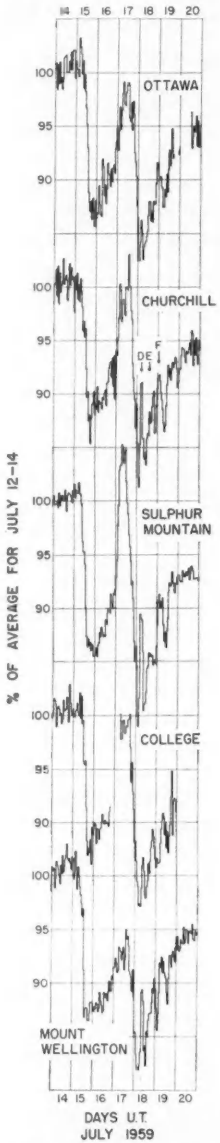

FIG. 1. Intensity–time curves on July 14 through 20, 1959, at: Ottawa, Churchill, Sulphur Mountain, College, and Mt. Wellington. Increasing geographic longitude to the west reading down. Average line through flat portion before the decrease on July 15 arbitrarily taken as 100%; other horizontal lines represent 5% variations. The time is universal time. The three peaks concerned here are marked D, E, and F, on the Churchill curve. They are clearly apparent on the other curves.

2. TIME OF OCCURRENCE OF PEAK "D"

The first point of interest is to determine where and when this sharp event occurred. Figure 1* shows the intensity–time curves from July 14 to July 20 at some stations at which the event is clearly present; they are arranged reading downward in order of geographic longitude increasing to the west. The time is universal time. An average line through the level portion before the decrease on July 15 arbitrarily represents 100% intensity; other horizontal lines represent 5% variations. For comparison Fig. 2 shows the intensity–time curves at other stations at which no sharp event is apparent early on July 18. These are divided in two groups; group A the high and low latitude stations, and group B the intermediate latitude ones. The stations in group B are also arranged in order of increasing geographic longitude to the west reading down. Figure 3 shows a map of the locations at which the early event "D" (Fig. 1) on July 18 did occur and those at which it did not. The positive events are seen to be well-grouped inside the oblong curve.

Let us consider next, the time at which this event occurred at the positive stations. The characteristic time is chosen as that represented by an intensity weighted mean time. This, expressed in universal time, as well as station local time, is shown in Table I together with the stations' geographic co-ordinates.

TABLE I

Intensity weighted mean time of occurrence of the sharp early event "D" on July 18, 1959, at 12 intermediate latitude stations (10 north, 2 south) expressed in U.T. (universal time) and L.T. (station local time). Increasing longitude to the west reading down

Station	Geographic		$T_{U.T.}$	$T_{L.T.}$
	Lat.	Long.		
Ottawa	45° N.	76° W.	0415±0005	23.3
Deep River	46° N.	78° W.	0505±0005	23.9
Chicago	42° N.	88° W.	0530±0030	23.6
Churchill	59° N.	94° W.	0555±0005	23.6
Lincoln	41° N.	97° W.	0555±0100	22.5
Climax	39° N.	106° W.	0615±0030	23.2
Sulphur Mt.	51° N.	116° W.	0645±0005	23.1
Berkeley	38° N.	122° W.	0600±0100	21.9
College	65° N.	148° W.	0830±0030	22.6
Sydney	34° S.	151° E.	0915±0100	19.4
Mt. Wellington	43° S.	147° E.	1045±0030	20.6
Mt. Norikura	36° N.	138° E.	0915±0100	18.5

It might be noted that the time at the five Canadian stations is given with less uncertainty than elsewhere since it was determined from 10-minute values of the intensity. The uncertainty is arbitrarily given as one-half the smallest interval of the intensity plot used. This amounts to 5 minutes for the Canadian stations, 30 minutes for stations giving hourly values, and 1 hour for stations giving bihourly values. The most striking feature of this table is the gradual increase of the characteristic time of the event (when expressed in U.T.) with

*We are grateful to Carmichael and Steljes for the original plotting of these curves. They have developed automatic plotting and normalization techniques which are very useful.

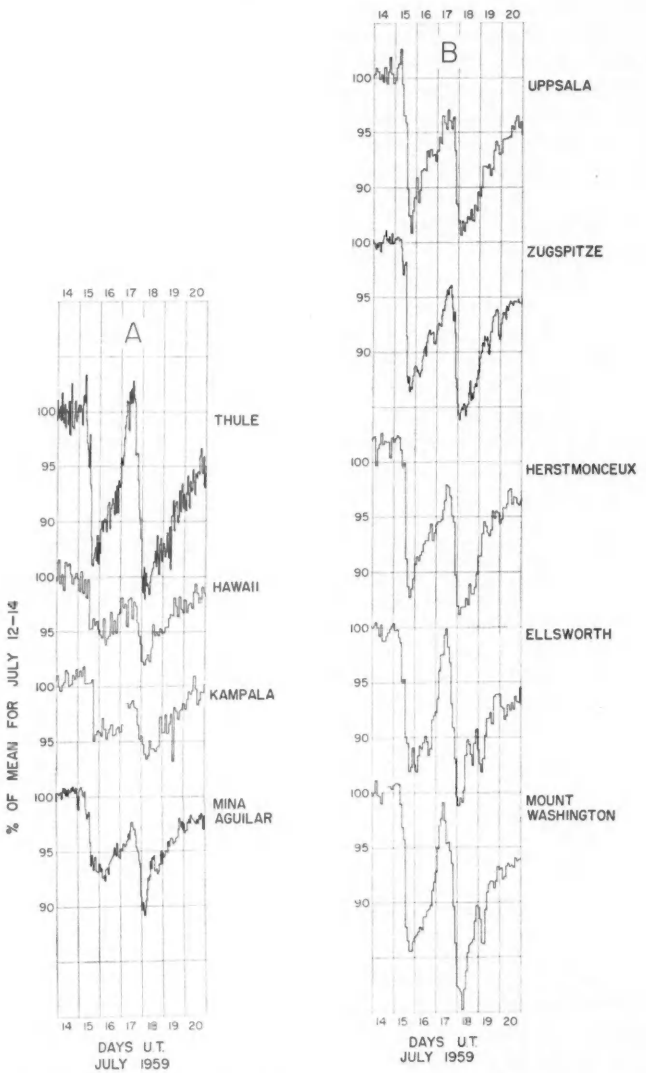

FIG. 2. Intensity–time curves on July 14 through 20, 1959. Group A, at Thule for high latitudes, Hawaii, Kampala, and Mina Aguilar for low latitudes. Group B, at Uppsala, Zugspitze, Herstmonceux, Ellsworth, and Mt. Washington for intermediate latitudes. Same co-ordinates as Fig. 1.

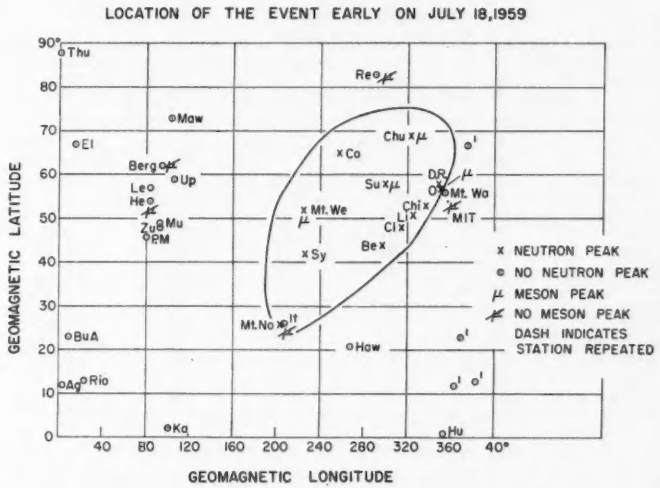

FIG. 3. Map of the stations at which the sharp event "D" did and did not occur early on July 18, 1959. × or μ means the event did occur in a neutron monitor or meson telescope respectively. ○ or μ with a stroke through it means the event did not occur. The oblong curve encircles the main region where the event occurred. The abbreviations for the station names are shown in Tables II and III.

increasing longitudes to the west, and the almost constant value of the mean time when expressed in local time. This indicates strongly that the beam of particles giving rise to the event did not arrive simultaneously from all directions on earth, but rather that it was limited in size, fixed in space, and that it appeared at a given station as the station passed through it due to the earth's daily rotation.

The fact that stations limited to the region shown by the oblong curve in Fig. 3 are the only ones showing this peak also indicates that primarily the beam was only of a few hours' duration. More details will be presented in Section 7 below.

3. INTEGRAL INTENSITY SPECTRUM IN PEAK "D"

The total intensity of the event measured at each one of the positive stations has been determined in the following way. First the intensity at each station has been expressed in per cent of the average of the intensity during the first 9 hours of July 15. Then a baseline was arbitrarily chosen in each case as that line which represented the smoothed intensity without the peak. The intensity in each time interval was then taken as the difference between the actual intensity and this imaginary baseline; the resulting intensity is a figure which was less than 10% for each time interval. The sum of these intensities for each 10-minute interval over the whole duration of the peak is taken to represent the total intensity. This total intensity is given in Table II for each one of the positive stations, together with the conventional geomagnetic co-ordinates and

TABLE II

Total intensity of the early July 18, 1959, event "D" at 11 stations; the unit is explained in the text. The first two and the last column give the conventional geomagnetic coordinates and the conventional cutoff energy of vertically incident protons at each station. Increasing geomagnetic latitude reading down

Station	Abbr. used in Figs.	Geomagnetic (degrees)		I_{Total}	Cutoff energy for protons in Bev
		Lat.	Long.		
Mt. Norikura	Mt. No	26	204	54	8.9
Sydney	Sy	−42	226	101	3.64
Berkeley	Be	44	298	83	3.12
Climax	Cl	48	315	130	2.14
Mt. Wellington	Mt. We	52	225	148	1.36
Chicago	Chi	53	337	82	1.21
Ottawa	O	57	351	151	0.65
Deep River	DR	58	349	122	0.54
Sulphur Mt.	Su Mt.	58	300	252	0.54
College	Co	65	257	81	0.12
Churchill	Chu	69	323	195	0.04

conventional cutoff energy for vertically incident protons at the station in question (centered dipole field). Although the event is not simultaneous at all stations, and although the beam intensity may vary with universal time and therefore also from station to station as they pass under the beam, nevertheless a plot of the intensity versus vertical cutoff energy may give some indication of the nature of the energy spectrum of the incoming particles. This has been done in Fig. 4. There is considerable variation in intensity with universal time but a comparison of stations with almost the same geographical longitude should give some indication of the shape of the spectrum when compared with a curve plotted from measurements on the ordinary total cosmic-ray spectrum. Such pairs of stations are Chicago and Churchill, Sulphur Mountain and Berkeley, Sydney and Mt. Wellington. Examine these, particularly in relation to the ordinary cosmic-ray spectrum represented by the solid line and, in fact, the general distribution of points suggests that the spectral distribution of peak "D" is somewhat flatter or at least no steeper than that for the ordinary cosmic-ray spectrum. The curve for the ordinary cosmic-ray spectrum was derived from Dorman (1957). Arbitrary units are used, therefore, the comparison is only relative. The consistent high intensity of this peak being limited to the stations in the Western Hemisphere (enclosed by the closed curve in Fig. 3), as each station passed through the zone of maximum activity, suggests that this beam or flow of particles lasted for only about 10 hours.

In view of the above evidence, we conclude that the beam giving rise to sharp peaks early on July 18, 1959, was made up of ordinary cosmic rays leaking through a "hole" in the modulating mechanism producing the Forbush decrease. For reasons mentioned in the last paragraph, comparisons of intensities in this way are subject to some criticism but there is additional evidence that the above conclusion is correct. An examination of the meson component shows that the peak "D" appears in this component at an intensity consistent with this conclusion. The times of occurrence at a number of stations where meson data have been studied are the same as that for the nucleon component

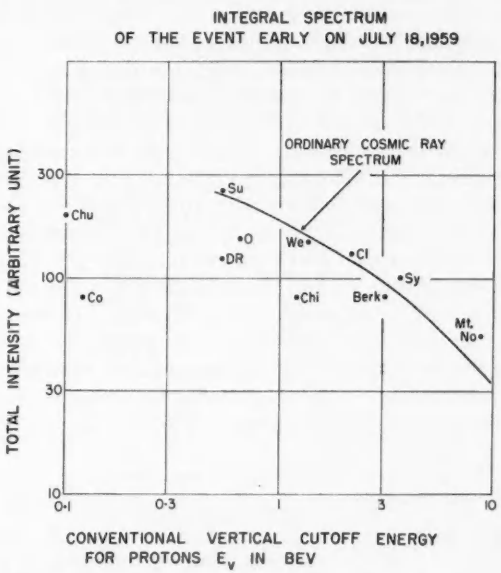

FIG. 4. Total intensity of the early July 18, 1959, event "D" at various stations as a function of conventional cutoff energy for vertically incident protons at that station. The solid line represents the integral intensity spectrum (arbitrary ordinate) of ordinary cosmic-ray protons (Dorman 1957). The abbreviations used for station names are shown in Tables II and III.

and the intensity, compared to the intensity of the nucleon peaks, is about that expected if the spectrum is that of the usual galactic cosmic rays. Ordinarily, the depth of a Forbush decrease is appreciably greater in the case of the nuclear component than for the meson component. The mean ratio for high latitude stations is about 2 though there is considerable variation (Fenton, Fenton, and Rose 1958). In the present case the depth of the Forbush decrease on July 17 is complicated by the large increase in the flux of soft particles occurring for a few hours before the July 17 decrease. The Forbush decrease on July 15, however, seems normal. The ratios of the depths of the decrease in nucleon intensity to the meson decrease for this event were 2.5, 2.3, and 2.1 respectively for Ottawa, Sulphur Mountain, and Churchill. The corresponding ratios for the peak "D" at these three stations are 1.0, 1.8, and 3.4 (obtained by numerical integration as explained above). These are within the ranges of expected values if the incoming particles have, at least approximately, the spectrum of normal galactic cosmic rays.

4. DIRECTIONAL SENSITIVITY OF THE DETECTORS

Because of the deflection of cosmic-ray particles in the earth's magnetic field their apparent impact direction at the earth's surface is not in general the direction in which they were travelling before entering the earth's magnetic

field. In a given impact direction particles of different energies come from different directions often spoken of as the asymptotic directions. A neutron monitor for instance detects particles arriving within a cone of half angle about 50° centered on the vertical, with sensitivity decreasing rapidly with increasing angle from the vertical. Taking all these factors into account, one can determine the average asymptotic direction from which particles of a given energy spectrum reach the recording equipment. This has been called the effective direction (Dorman 1957) or the direction of maximum response (Fenton, McCracken, Rose, and Wilson 1959). Most particles come from a direction east of the station (Brunberg and Dattner 1953). The effective direction is also east of the station, the amount depending on the station's geomagnetic latitude. We have calculated the effective directions of a neutron monitor covering all geomagnetic latitudes from the equator to the pole. The method of calculation and the results will be published elsewhere. From these calculations the effective directions are available for all the stations considered here and are listed in Table III. The accuracy of the calculations is adequate

TABLE III

Direction of maximum response to the east of the observing meridian expressed both in degrees and in time

Station	Abbr. used in Figs.	Geomagnetic lat. (degrees)	Shift to the east (degrees)	Time increment (hr)
Mt. Norikura	Mt. No.	26	71	4.7
Sydney	Sy	−42	79	5.3
Berkeley	Be	44	62	4.1
Climax	Cl	48	56	3.7
Lincoln	Li	51	47	3.1
Mt. Wellington	Mt. We	−52	58	3.9
Chicago	Chi	53	43	2.9
Ottawa	O	57	36	2.4
Deep River	DR	58	38	2.5
Sulphur Mt.	Su Mt.	58	28	1.9
College	Co	65	16	1.1
Churchill	Chu	69	19	1.3
Mawson	Ma	−73	7	0.5
Uppsala	Up	59	54	3.6
Munich	Mu	49	70	4.7
Zugspitze	Zu	48	74	4.9
Pic du Midi	P M	46	78	5.2
Herstmonceux	He	54	60	4.0
Leeds	Le	57	55	3.7
Ellsworth	El	−67	24	1.6
Rio de Janeiro	Rio	−13	78	5.2
Mina Aguilar	M Ag	−12	82	5.5
Mt. Washington	Mt. Wa	56	39	2.6
Resolute	Re	83	−1	−0.1

for the purposes considered here. In Table III the directions are expressed as a longitude shift to the east of the observers' meridian, that is, the station passes under the effective direction at a time later than the time of observation of the maximum by the amount shown in Table III. The corrected times or the times the stations are in the meridian of the effective direction are shown in Table IV. These are shown in local time and within the order of over-all

TABLE IV

Intensity weighted mean time of event "D" early on July 18, 1959, in the nucleonic component, corrected for direction of maximum response, and expressed in local time

Station	$T_{L.T.}$ actual	$T_{L.T.}$ corrected
Ottawa	23.3	1.7
Deep River	23.9	2.4
Chicago	23.6	2.5
Churchill	23.6	0.9
Lincoln	22.5	1.6
Climax	23.2	2.9
Sulphur Mt.	23.1	1.0
Berkeley	21.9	2.0
College	22.6	23.7
Sydney	19.4	0.7
Mt. Wellington	20.6	0.5
Mt. Norikura	18.5	23.2
Average		1.3

accuracy; the local time is almost the same at all stations. The average is 1.3 hours. The four stations from which most reliable times can be derived namely Ottawa, Deep River, Churchill, and Sulphur Mountain, give an average corrected local time of 1.5 hours with extremes of $+0.9$ and -0.6 hours. This corresponds to a direction in the sky making an angle of about 165° with the sun–earth line. The opening in the modulating mechanism which in the case of peak "D" lasted about 10 hours occurred on the side of the earth almost opposite the sun.

5. ASYMMETRY IN THE RECOVERY FROM THIS DEEP FORBUSH EVENT

Although this hole in the modulating mechanism only appeared open for about 10 hours when it was first apparent, there is evidence that recovery in this direction remained more favorable (allowing varying intensities of passage of recovery particles) for at least two rotations of the earth. Further, another direction of favored recovery appeared in a direction almost opposite the above or nearly in the sun–earth line. The time–intensity curves in Figs. 1 and 2, in many cases reveal more peaks later on in the day on July 18 and on July 19 during the early part of the recovery from the Forbush decrease. These peaks are listed in Table V, when they are clearly distinguishable, together with the approximate time of their occurrence expressed in universal time: the uncertainty in this time, read directly off the intensity–time graphs is taken as ± 2 hours. These events are then plotted in Fig. 5 after correction for direction of maximum response. This graph shows geographic longitude at which the event occurred as a function of corrected universal time when it occurred. In other words, a point represents a direction in space under which the station concerned would be at the indicated universal time when the event occurred for that observer. The sloping lines show constant local time or constant direction with respect to the sun–earth line. It is remarkable how the events line up on slopes of constant local time situated 12 hours apart. This means,

TABLE V

List of the events on July 18 and 19, 1959. The time of occurrence (uncorrected) is expressed in U.T. A dash means no event is visible on the record. A question mark means data are incomplete in that region. The columns represent constant local time and, therefore, constant direction in the sky. Increasing longitude to the west reading down

Station	13 L.T.	01 L.T.	13 L.T.	22 L.T.	13 L.T.
Ottawa		0415	14	24	16
Deep River		0505	—	24	—
Chicago		0530	16	24	—
Churchill		0555	18	2	18
Lincoln		0500	16	2	—
Climax		0615	—	1	?
Sulphur Mt.		0645	17	4	—
Berkeley		0600	15	3	—
College		0830	21	9	21
Sydney		0915	?	6	?
Mt. Wellington		1045	23	9	—
Mt. Norikura		0915	24	—	
Mawson	15	22	10	20	
Uppsala	—	—	8	20	
Munich	—	—	7	19	
Zugspitze	—	—	8	19	
Pic du Midi	13	—	—	17	
Herstmonceux	—	—	7	20	
Leeds	—	—	9	22	
Ellsworth	14	22	13	23	
Rio de Janeiro	12	—	—	—	
Mina Aguilar	13	—	—	—	
Mt. Washington	—	24	14	1	

according to our hypotheses, that there existed two holes in the modulating mechanism diametrically opposed or 180° apart, one at 0100 L.T. and the other at 1300 L.T., making respectively 165° and 15° with the sun–earth line. These lasted for almost two complete revolutions of the earth and disappeared only on July 20 at which time the recovery from this last Forbush decrease seemed reasonably complete. However, since all the peaks do not occur at all stations as they pass under the direction of the opening the holes were not continuously open to the maximum extent. The first peak with an average position in time of 01.3 hours appeared to be fully present for only about 10 hours represented by the width (in longitude) of the oval in Fig. 3. The length of this period is open to a question of interpretation but it is very clear that this peak was either missing or quite small or possibly displaced in time as shown by the gap in points on or near the 01-hour line in Fig. 5 in the longitude region from 60° east to 70° west. The second and third peaks on the lines representing 13 and 22 hours local time seemed more uniformly distributed around the earth but were, of course, wider and in some cases sufficiently diffuse to make interpretation not entirely definite.

6. COMPARISON WITH OTHER ASYMMETRIES IN THE FORBUSH DECREASE MECHANISM

It has been reported by Fenton, McCracken, Rose, and Wilson (1959) that during a Forbush-type decrease, the intensity is first depressed in directions running from 30° to 120° to the west of the sun–earth line. The median direction

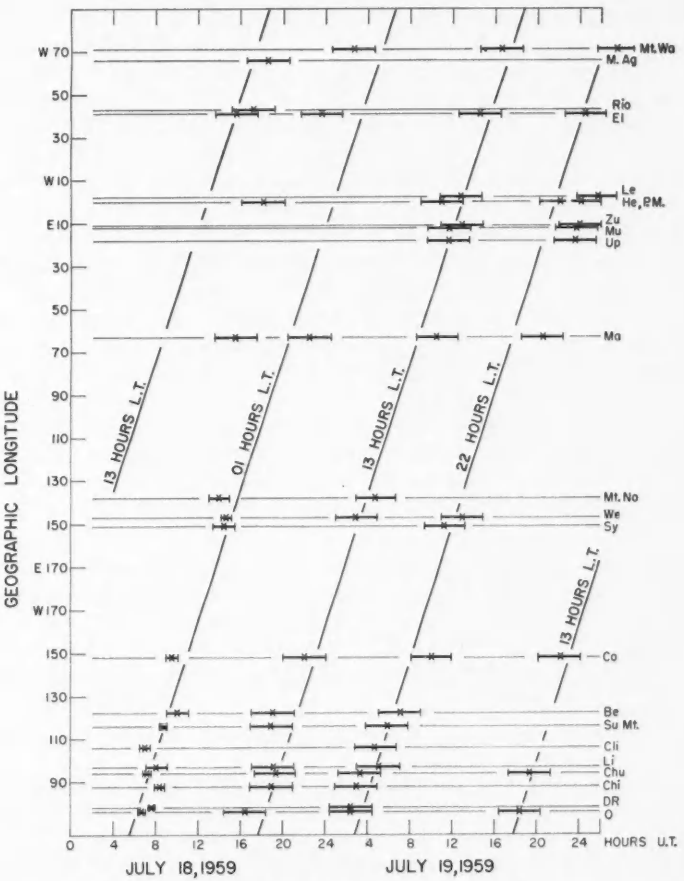

FIG. 5. Time–occurrence diagram of the events recorded on July 18 and 19, 1959, at a number of stations. Ordinate: geographic longitude increasing to the west upwards; abscissa: universal time. Sloping lines represent constant local time, and hence constant direction in space. The abbreviations used for station names are shown in Tables II and III.

to be first depressed, therefore, makes an angle of 75° with the sun–earth line and hence is perpendicular to the direction in which the intensity is first to recover, as determined above. The same authors give the median direction in which the intensity is last depressed as the one making an angle of 45° to the east of the sun–earth line; this by the way is also almost the direction of the maximum of the average daily variation at Hobart during 1957. All these directions are illustrated in Fig. 6. It might be noted that the directions of first and last depression in the Forbush mechanism were determined in the paper just quoted, from the analysis of 22 events and therefore seem to be a general enough feature.

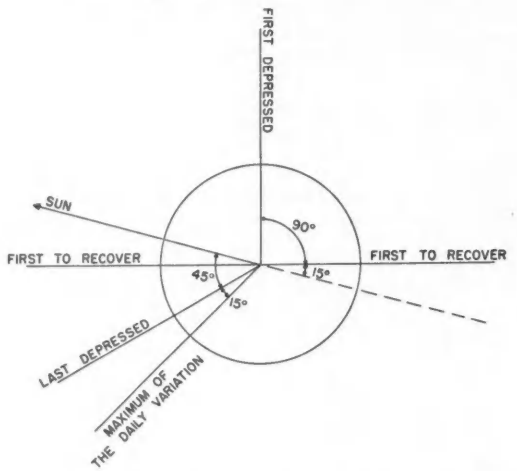

FIG. 6. Characteristic directions with respect to the sun–earth line in the Forbush-type decrease mechanism.

It seems very natural in a general sort of way, there being no definite model for the Forbush-type decrease mechanism, that the intensity should recover first in directions perpendicular to that in which it was first depressed. We therefore conclude from the foregoing analysis:

(*a*) The early event on July 18, 1959, was not simultaneous at all the stations observing it on earth.

(*b*) The energy spectrum of the incoming particles strongly suggests that they consist of ordinary cosmic rays.

(*c*) This being the case, particles making 15° and 165° with the sun–earth line are first to leak through the depressing mechanism.

7. DISCUSSION

The night side (01 h L.T.) "hole" opened up first just over Ottawa. This onset seems to be very sharp since nearby Mt. Washington and M.I.T. (mesons) had just passed and did not record it at least not with any appreciable strength. Mt. Washington picks it up the next time around.

The most outstanding and really the only significant gap is the one for the European stations around 24 U.T. July 18. It would seem that the night side hole was closed when they moved into position. Unfortunately, we have no data for the stations in Asia between the Australian and the European stations to follow the development of this intensity variation with time. But the openings certainly exist over the European stations in the next two positions.

Some further features of these intensity increases which have not been emphasized yet merit discussion. The beam is assumed to be composed of ordinary cosmic-ray particles, but it is not detected at low latitude stations.

Our method of deciding whether or not the event occurred is necessarily coarse; and because of intensity fluctuations only relatively large cases can be distinguished. Consider Sydney almost the lowest positive station, where the geomagnetic latitude is $-42°$ and the vertical cutoff energy for protons is 3.6 Bev. The next positive station available is Mt. Norikura where $\lambda = 25°$ and $E_v = 8.9$ Bev. At Sydney the maximum intensity in the peak is 4.5%. At Mt. Norikura it would be $4.5\% \times (3.6/8.9)^{1.1}$ or about 1.5%; this is barely detectable as an event. Therefore, the absence of events at lower latitude stations is consistent with an ordinary cosmic-ray beam leaking through holes and resulting in the events analyzed here.

Two polar cap stations have been considered, namely, Thule and Resolute. One might expect the intensity peaks there to be as big as they are near the positive stations of highest latitude. However, the holes are probably limited in latitude, up to this point in the analysis only longitudinal asymmetries have been considered.

According to our calculation of effective directions for neutron monitors, the asymptotic latitude of maximum response at Resolute is 64° N. geographical, and at Thule lies between 74° and 84° N. geographical. Hence, the absence of signal at the polar cap stations is consistent with the simple assumption that the holes extended to no more than 60° in the active meridian plane. If one takes 6 hours as the typical duration of the event (width of the beam), this means a divergence of 90° in the equatorial plane. If one were to assume the same size or divergence in a meridian plane, then one would conclude that the beam does not extend to more than 45° N. and 45° S. in asymptotic latitude. Therefore, the stations Thule and Resolute may have had no connecting orbits with the holes.

ACKNOWLEDGMENTS

The authors would like to express their appreciation to those operating the many stations of the I.G.C. network who generously have made their data available by private communication. S. M. Lapointe is grateful to the National Research Council of Canada for its hospitality in the summer of 1960 while this work was performed. Appreciation is expressed in footnotes of the assistance of H. Carmichael and J. Steljes in exchange of plotted curves. We would like to extend this expression of appreciation for discussions and comments.

REFERENCES

BRUNBERG, E. A. and DATTNER, A. 1953. Tellus, **5**, 269.
CARMICHAEL, H. and STELJES, J. F. 1959. Phys. Rev. Letters, **3**, 392.
DORMAN, L. I. 1957. Cosmic ray variations (State Publishing House for Technical and Theoretical Literature, Moscow. Translation by United States Technical Documents Liaison Office).
FENTON, A. G., FENTON, K. B., and ROSE, D. C. 1958. Can. J. Phys. **36**, 824.
FENTON, A. G., MCCRACKEN, K. G., ROSE, D. C., and WILSON, B. G. 1959. Can. J. Phys. **37**, 970.
STELJES, J. F. and CARMICHAEL, H. 1960. Bull. Am. Phys. Soc. **5**, 360.
WILSON, B. G., ROSE, D. C., and POMERANTZ, M. A. 1960. Can. J. Phys. **38**, 328.

THE EMISSION SPECTRUM OF THE CCl RADICAL[1]

R. D. GORDON[2] AND G. W. KING

ABSTRACT

A rotational analysis of the 2780 Å emission band obtained in a microwave discharge through CCl_4 vapor and photographed on a 20-ft grating spectrograph shows that a $^2\Delta_i(b) \rightarrow {}^2\Pi_r(a)$ transition of the CCl radical is responsible, not $^2\Sigma \rightarrow {}^2\Pi(a)$ as reported by previous workers. Molecular constants are given for the combining states, as well as a vibrational analysis that identifies the 2780 Å band as the (0–0) band.

INTRODUCTION

A high-frequency electrical discharge through carbon tetrachloride vapor at low pressure produces a series of emission bands in the 2710–2940 Å region. Under low resolution four bands, lying at approximately 2714, 2780, 2850, and 2920 Å, are prominent, those at 2780 and 2850 Å being double-headed and especially intense in emission (Fig. 1). Various vibrational analyses have

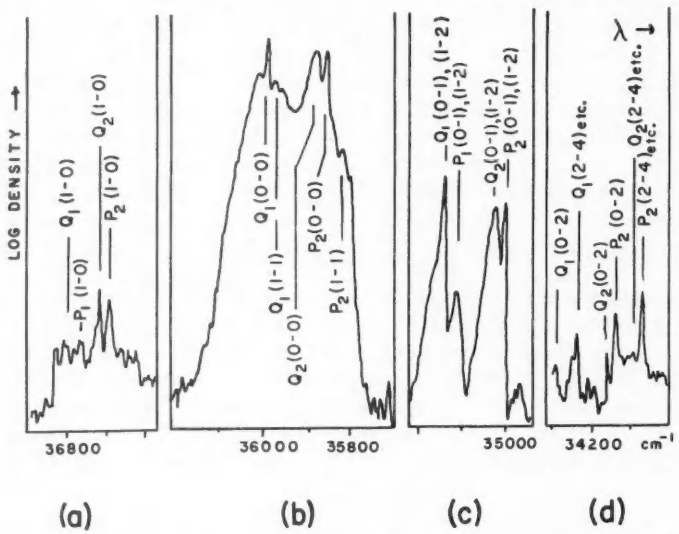

FIG. 1. Microdensitometer profiles of CCl bands at (*a*) 2714, (*b*) 2780, (*c*) 2850, (*d*) 2920 Å under low resolution.

[1]Manuscript received October 13, 1960.
Contribution from the Department of Chemistry, McMaster University, Hamilton, Ontario.
[2]Holder of Imperial Oil Graduate Research Fellowship, 1959–1960.

been attempted (Asundi and Karim 1937; Horie 1939), the most extensive being that of Venkateswarlu (1950) on the basis of a $^2\Sigma \rightarrow {}^2\Pi$ electronic transition of the CCl radical. Kuzyakov and Tatevsky (1959*a*) agreed that this transition was responsible for the bands, but criticized inconsistencies in Venkateswarlu's analysis, which gave a high value of 22 ev for the lower state dissociation energy. They proposed a new vibrational scheme, and also (1959*b*) gave rotational analyses of two branches in each of the stronger bands of the system that supported a $^2\Sigma \rightarrow {}^2\Pi(a)$ electronic assignment. However, no vibrational analysis has been free of inconsistencies so far, mainly owing to uncertainty in identifying the observed band heads.

We have rephotographed the spectrum under much higher resolution than was used in previous work, and a detailed study of the band at 2780 Å shows that the transition is, in fact, $^2\Delta(b) \rightarrow {}^2\Pi(a)$. This analysis enabled positive identification of heads and prominent features in the other bands to be made, resulting in a satisfactory vibrational scheme which shows the 2780 Å band is the (0–0) transition. Both the rotational and vibrational analyses are consistent with CCl being the diatomic species responsible for the spectrum.

EXPERIMENTAL

Spectra were excited using a Raytheon "Microtherm" model CMD 4, delivering 100 watts of microwave radiation at 2450 Mc/s. The antenna was mounted 1 cm from the outside of a 12-mm hard-glass discharge tube which was viewed end on by the spectrograph through a silica window. Helium gas at 0.1 mm pressure was flowed through the tube as a carrier gas, together with carbon tetrachloride at sufficient vapor pressure to change the red helium discharge to a bluish-white color; the carbon tetrachloride was of reagent grade quality, resublimed three times under vacuum. The visible discharge was some 5 cm long. Low-resolution spectrograms were taken in the second order of a 1.5 m Bausch and Lomb spectrograph model 11. High-resolution spectra were obtained on a 20-ft Ebert grating spectrograph (King 1958), used in the second order with a resolving power in excess of 200,000. Using Kodak 103*a*0 plates, exposure times were about 4 hours, but increased with the age of the discharge tube, whose walls became coated with brown polymer. Plates were measured in both directions on a travelling microscope, each line being measured three times during each run. Iron arc spectra were used for calibration, with wavelengths taken from the M.I.T. tables (Harrison 1939), together with the vacuum corrections of Edlén (1953). Vacuum wavenumbers and assignments for all the rotational lines of the 2780 Å band are given in Table I.

When the spectrum of pure helium was excited under identical conditions, plates of 11-hours' exposure showed a very faint semicontinuous background, with no strong atomic lines in the region of the CCl spectrum. The spectra were free of contamination from this source, but the weak bands at 2714 and 2920 Å, which were only photographed under low resolution, were, apart from heads, just slightly more intense than a continuous background ascribable to the chlorine molecule.

TABLE I

Vacuum wavenumbers and rotational assignments for the 2780 Å band of CCl

	$^2\Delta \rightarrow {}^2\Pi_{1/2}$			$^2\Delta \rightarrow {}^2\Pi_{3/2}$				
J	R_{21}	R_1	P_1	R_2	R_{12}	Q_2	P_2	P_{12}
1.5		35998.93		35876.64	35865.60	35872.96		
2.5		36000.10		878.66	866.57	873.34	35869.63	
3.5		001.29		880.60	867.69	873.80	868.75	
4.5		002.43	35988.98	882.45	868.75	874.38	867.41	
5.5		003.56	987.46	884.36	869.63	874.90	866.57	
6.5		004.71	985.92	886.38	870.63	875.36	865.71	35851.97
7.5		005.59	984.31	888.43	872.04	875.95	864.88	850.25
8.5		007.01	982.67	890.49		876.64	864.17	848.49
9.5		008.12	981.04	892.79		877.36	863.54	846.81
10.5		009.30	979.45	894.97		878.13	862.73	844.94
11.5		010.50	977.79	897.20		878.94		843.52
12.5		011.68	976.285	899.41		879.75		841.44
13.5		012.80	974.75	901.70		880.60		839.76
14.5		014.31	973.09	904.02		881.52		837.97
15.5		015.48	971.83	906.35		882.45		836.22
16.5	36044.36	016.69	970.09	908.83		883.37		834.50
17.5	046.65	017.99	968.63	911.10		884.36		832.81
18.5	049.52	019.47	967.17	913.49		885.56		831.09
19.5	052.24	021.10	965.72	915.92		886.68		829.40
20.5	054.92	022.23	964.34	918.38		887.40		827.73
21.5	057.67	023.65	962.98	920.84		888.43		826.09
22.5	060.48	025.10	961.62	923.30		889.54		824.45
23.5	063.29	026.63	960.33	925.82		890.59		822.83
24.5	066.09	028.10	959.06	928.35		891.75		821.23
25.5	069.01	029.72	957.63	930.89		892.76		819.61
26.5	071.92	031.27	956.59	933.57		894.07		818.05
27.5	074.87	032.68		936.05		895.23		816.52
28.5	077.82	034.28		938.59		896.39		814.58
29.5	080.47	035.91		941.24		897.64		813.73
30.5	083.83	037.54		943.88		898.86		811.98
31.5	086.92	039.16		946.56		900.29		810.51
32.5	089.98	040.86		949.19		901.41		809.04
33.5	093.10	042.62		951.89		902.71		807.64
34.5	096.26			954.40		904.02		806.20
35.5	099.49					905.52		804.82
36.5	102.63					906.66		803.40
37.5								802.08
38.5								800.75
39.5								799.44
40.5								798.08
41.5								796.82
42.5								795.54

ROTATIONAL ANALYSIS OF THE 2780 Å BAND

A microdensitometer trace of this band under high resolution is shown in Fig. 2. It consists of two subbands separated by approximately 130 cm^{-1}, with two heads, labelled Q_1 and P_2 degraded to shorter wavelengths. Four intense branches can be picked out in each subband, labelled P_1, Q_1, R_1, R_{21}; P_{12}, P_2, Q_2, R_2. The large separation between the subbands, and also the presence within each of a fourth chief branch for which necessarily $\Delta K \neq \Delta J$ implied that the transition was between a Hund's case (a) and a case (b) doublet state. Lines of low J numbering were found to deviate from a parabolic formula,* which implied that the latter state was not purely case (b),

*"Low J deviations" are those caused by the terms in α in equation (3) below.

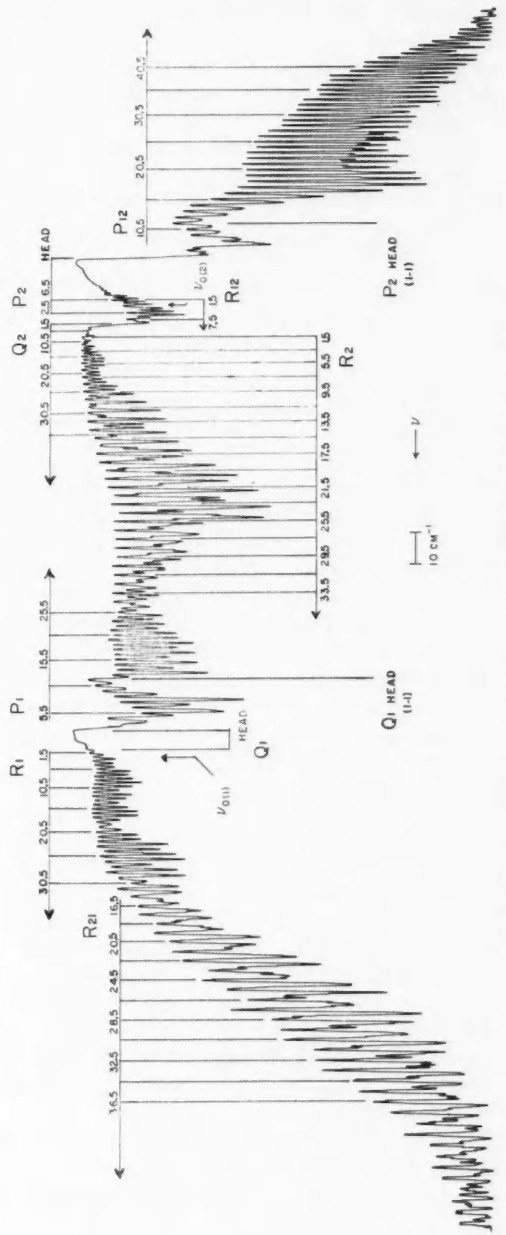

FIG. 2. Microdensitometer profile of CCl band at 2780 Å under high resolution.

with zero doublet separation, and could not be a $^2\Sigma$ state. The effect of these deviations can be most clearly seen in Fig. 2 in the R_1 and Q_2 branches; the Q_2 branch spacings at low J values are much smaller than those in the R_1 branch, whereas the spacings in these branches should be the same for transition from a pure case (b) state.

Analysis showed that two intense branches were of Q type; hence $\Delta\Lambda = \pm 1$ for the transition. The electron configuration of CCl demands a $^2\Pi_r$ ground state; electronically similar molecules such as SiF (Eyster 1937), CF (Andrews and Barrow 1951), and NO (Schmid 1930) all have $^2\Pi_r(a)$ lower states for transitions observed under similar conditions. Thus the transition will be considered as $^2\Delta(b) \rightarrow {}^2\Pi_r(a)$, the details of the analysis confirming this assignment. All attempts to analyze the band on the basis of a $^2\Sigma \rightarrow {}^2\Pi(a)$ transition failed.

1. Term Values and Expected Spectrum

Standard analytical formulae are given in the literature (Herzberg 1950 and references quoted therein) and only certain aspects of these need further discussion here. The expected total of 24 branches in the band is reduced to 12 if Λ-type doubling is not separately resolved. All of the main ($\Delta K = \Delta J$) branches P_1, Q_1, R_1; P_2, Q_2, R_2 were observed as well as the intense ($\Delta K \neq \Delta J$) branches R_{21} and P_{12}. The remaining weaker branches P_{21}, Q_{21}; Q_{12}, R_{12} closely paralleled other branches and were not separately resolved, except for a number of lines in the R_{12} branch that were revealed owing to the low J deviations of the Q_2 branch, as can be seen in Fig. 2. Very few of the P_2 lines, and none of the Q_1 lines (both head-forming) could be resolved. Thus the analysis relied mainly on three branches in each subband (P_1, R_1, R_{21}; P_{12}, Q_2, R_2).

Rotational term values for doublet states intermediate between Hund's cases (a) and (b), relative to a vibronic origin, are given by

$$F_i(J) = B_v[(J+\tfrac{1}{2})^2 \mp \{(J+\tfrac{1}{2})^2 + C^2\}^{\frac{1}{2}}] \tag{1}$$

upper and lower signs referring to $i = 1$, $(J = K+\frac{1}{2})$ and $i = 2$, $(J = K-\frac{1}{2})$ respectively, $C^2 = Y(Y-4)\Lambda^2/4$, with $Y = A/B_v$, A being the spin-orbit coupling constant. Additional terms due to Λ-type doubling and centrifugal stretching need not be added to equation (1); from the relation $D_v \sim 4B_v^3/\omega^2$, with approximate values $B_v = 0.6\ \text{cm}^{-1}$ and $\omega = 860\ \text{cm}^{-1}$, $D_vJ^3 \sim 0.05\ \text{cm}^{-1}$ even at $J = 30$ (cf. resolution of $\sim 0.15\ \text{cm}^{-1}$). Also, least squares analysis of combination differences with B_v as a linear and D_v as a higher power coefficient gave values for D_v of the order of magnitude of the deviation in B_v. Magnetic coupling terms γ were also ignored for the same reason: in any case, they are expected to be negligibly small even in the Δ state over the range of K values used in the analysis.

For the $^2\Pi_r(a)$ lower state, with large Y, A, and C, expansion of the square root term in (1) as $C\{1+(J+\frac{1}{2})^2/C^2\}^{\frac{1}{2}}$ gives

$$F_i''(J) = B_v''/4 \mp B_v''(C''+1/8C'') + (B_{\text{eff}}'')_i J(J+1) \tag{2}$$

where the effective rotational constant $(B_{\text{eff}}'')_i = B_v''[1 \mp 1/2C'']$. Quadratic

and higher terms in the expansion were ignored since they contribute <0.01 cm^{-1} for $J < 32$. Terms independent of J in (2) are not considered in the rotational analysis, being included in the vibronic energy.

For the $^2\Delta(b)$ upper state, with small Y, A, and C, expansion of the square root term in (1) as $(J+\frac{1}{2})\{1+C^2/(J+\frac{1}{2})^2\}^{\frac{1}{2}}$ gives

$$(3) \qquad F_1'(J) = B_v'\left[(J-\tfrac{1}{2})(J+\tfrac{1}{2})-\left(\frac{\alpha}{J+\frac{1}{2}}+\ldots\right)\right]$$

$$F_2'(J) = B_v'\left[(J+\tfrac{1}{2})(J+3/2)+\left(\frac{\alpha}{J+\frac{1}{2}}+\ldots\right)\right]$$

where $\alpha = (C')^2/2$. Although the original expression (1) is used below in determining C' accurately, (3) was useful in detecting errors in the combination differences (4) described in the next section.

2. Lower State Constants

The analysis began by considering the following two combination differences, each of which involved only lower state levels and thus cancelled exactly any low J deviations in the upper state.

$$(4) \qquad R_2(J-1)-Q_2(J) = 2(B''_{\text{eff}})_2 J$$

$$R_1(J-1)-P_1(J+1) = 4(B''_{\text{eff}})_1(J+\tfrac{1}{2})$$

The assignment was helped by the fact that for incorrect relative numberings of branches, terms in α in (3) caused large residual errors in fitting (4) to linear functions of J by the method of least squares. The unique numbering found for each pair of branches gave the values of $(B''_{\text{eff}})_1$, $(B''_{\text{eff}})_2$, and $B_0'' = \{(B''_{\text{eff}})_1+(B''_{\text{eff}})_2\}/2$ shown in Table II. The approximate value obtained

TABLE II

Rotational constants for the 2780 Å band. Errors are quoted as standard deviations

Upper $^2\Delta(b)$ state:	$B_0 = 0.70533\pm0.00062$ cm^{-1}
	$r_0 = 1.63546\pm0.00073$ Å
Doublet splitting:	$Y' = -5.87$ } or* { $+9.87$
	$A' = -4.14$ cm^{-1} } { $+6.96$ cm^{-1}
Lower $^2\Pi_r(a)$ state:	$(B''_{\text{eff}})_1 = 0.68892\pm0.00101$ cm^{-1}
	$(B''_{\text{eff}})_2 = 0.69506\pm0.00096$ cm^{-1}
	$B_0'' = 0.69199\pm0.00069$ cm^{-1}
	$r_0'' = 1.65115\pm0.00081$ cm^{-1}
Doublet splitting:	$Y'' = 195.03\pm0.19$
	$A'' = 134.96\pm0.13$ cm^{-1}
Subband origins:	$\nu_{0(1)} = 36{,}000.92\pm0.25$ cm^{-1}
	$\nu_{0(2)} = 35{,}867.35\pm0.12$ cm^{-1}

*Positive values are for a regular, and negative values for an inverted $^2\Delta$ state.

for Y'' from the difference between $(B''_{\text{eff}})_1$ and $(B''_{\text{eff}})_2$ was 224 ± 51 cm^{-1}, consistent with the more precise value of 195.03 cm^{-1} obtained below.

The doublet splitting $\Delta''(J)$ is given by the following two relations:

$$(5) \qquad \Delta''(J) = F_2''(J)-F_1''(J) = P_1(J)-P_{12}(J) = R_{21}(J)-R_2(J).$$

The numbering in the P_1 and R_2 branches is already known; it was established for the P_{12} and R_{21} branches as that for which equations (5) gave identical $\Delta''(J)$ values at each J. From equation (2),

$$\Delta''(J) = 2B_v''(C''+1/8C'')+\{(B_{eff}'')_2-(B_{eff}'')_1\}(J^2+J). \tag{6}$$

A least-squares treatment gave

$$\Delta''(J) = (133.57\pm0.013)+J(0.0158\pm0.0142)+J^2(0.00635\pm0.00035). \tag{7}$$

The quadratic coefficient agrees with the value $(B_{eff}'')_2-(B_{eff}'')_1 = 0.00614 \pm0.00139\ \text{cm}^{-1}$ obtained from equation (4). The constant term was used to obtain the values of Y'' and A'' in Table II.

3. Upper State Constants

The following combination difference gave B_0' independently of deviations from case (*b*) in the upper state.

$$[R_1(J)-P_1(J)]+[\{R_2(J)-Q_2(J)\}+\{R_2(J-1)-Q_2(J-1)\}] = 4B_v'(2J+1). \tag{8}$$

The doublet splitting Δ' was obtained experimentally using the relation

$$\Delta'(N) = [F_2'(N)-F_1'(N)] = \Delta''(J)-[R_1(J)-Q_2(J)] \tag{9}$$

where N is the upper state value of K; values of $\Delta''(J)$ were taken from the least-squares equation (7). Attempts to fit the result to formulae derived from the approximate relation (3) failed, but good results were obtained by using the general equation (1), which gives, with N as the variable replacing J;

$$\Delta'(N) = B_v'[(N^2+C^2)^{\frac{1}{2}}+\{(N+1)^2+C^2\}^{\frac{1}{2}}-(2N+1)]. \tag{10}$$

A computer program gave $C^2 = 57.98$ as showing a minimum residual deviation of $0.138\ \text{cm}^{-1}$ between the calculated and observed values of Δ' over the range $N = 2$–34. Values for Y' and A' derived from this are given in Table II.

4. Determination of Subband Origins

The origin $\nu_{0(2)}$ of the subband at lower frequency was determined by a least-squares fit to the combination relationship;

$$R_2(J-1)+P_{12}(J+1) = 2\nu_{0(2)}+B_v'/2-2(B_{eff}'')_2 +2J(J+1)\{B_v'-(B_{eff}'')_2\}. \tag{11}$$

Since lines close to the other origin $\nu_{0(1)}$ were not resolved, an equation similar to (11) would introduce errors of extrapolation. Greater precision could be obtained by taking the constant term in (7) as $\nu_{0(1)}-\nu_{0(2)}$; compare equations (2) and (6). Values obtained are shown in Table II.

5. Doubling of Lines

Although Λ-type doubling was not resolved, detailed examination of lines indicated that those in the subband at higher frequency were slightly broader, as would be expected for a $^2\Pi_r$ lower state; doubling in the $^2\Delta$ state would be negligibly small. Also, lines in the P_{12} and R_{21} branches, which stand out

clearly on opposite edges of the band, showed slight indications of splitting into two components. The effect was too small to be resolved properly, and cannot be seen in Fig. 2. It did not seem due to Λ-type doubling, since its magnitude was independent of J. Satellite bands do not parallel these branches, but the isotopic CCl^{37} species could cause additional lines to appear weakly. A Zeeman effect caused by magnetic fields in the discharge tube could cause doubling of rotational lines, as could quadrupole interactions of the chlorine nucleus in one electronic state, but the experimental evidence is too slight to decide on this.

VIBRATIONAL ANALYSIS OF THE BAND SYSTEM

The rotational analysis shows that the two intense heads of the 2780 Å band are in the Q_1 and P_2 branches, with a separation of 138.1 cm^{-1}. Two weaker intensity maxima with a separation of 138.5 cm^{-1} are ascribed to an underlying sequence band labelled (1–1) in Fig. 2. A rotational analysis of the more complex band at 2850 Å was not performed; nevertheless, similar heads can be identified in its high resolution spectrum, and these are shown in Fig. 3. Heads can also be identified, though somewhat more tentatively, in the two other weak bands of Fig. 1. The frequencies and separations of identified Q_1 and P_2 heads are listed in Table III. The head separation in a

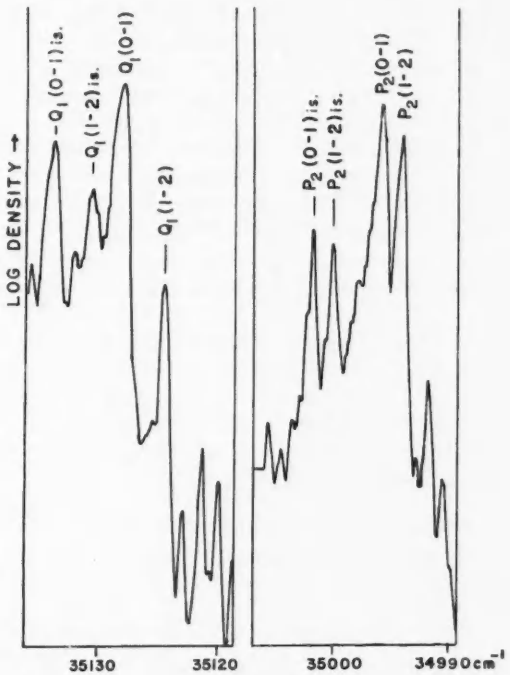

FIG. 3. Microdensitometer profiles of Q_1 and P_2 peaks in the CCl band at 2850 Å, under high resolution. Peaks marked "is." are due to CCl^{37}.

TABLE III

Frequencies (cm^{-1}) and assignments of band heads and bands (i = isotopic band)

Sequence	Head frequency Q_1	Head frequency P_2	Doublet separation $= Q_1 - P_2$	Band frequency $(Q_1+P_2)/2$
$\Delta v = +1$ (2714 Å)	36836	36700	136	36768 (1–0)
$\Delta v = 0$ (2780 Å)	35992.2	35854.1	138.1	35923.1 (0–0)
	976.3	837.8	138.5	907.1 (1–1)
	35134.2	35001.8	132.4	35068.0 (0–1)i
$\Delta v = -1$ (2850 Å)	130.9	000.1	130.8	65.4 (1–2)i
	128.2	34995.7	132.5	61.9 (0–1)
	124.6	993.9	130.7	59.2 (1–2)
$\Delta v = -2$ (2920 Å)	34284	34147	137	34215 (0–2)
	34246	34098	148	34172 (2–4), etc.

band will be very similar to the separations of the subband origins, and for this vibrational analysis, it is sufficiently accurate to call the mean of the head frequencies the band frequency, as shown in the last column.

Since the internuclear distances in the upper and lower electronic states differ by only 1%, we assumed first of all, along with previous workers, that the most intense band, that at 2780 Å, contained the (0–0) transition and its sequences, and the 2850 Å band contained the (0–1) transition and $\Delta v = v' - v'' = -1$ sequences. This gives $\omega'' \sim 860\ cm^{-1}$. ω' must be of similar magnitude if the 2714 Å band contains the (1–0) sequence.

Confirmation comes from the isotope effect. Bands due to the isotopic CCl^{37} species should appear with appreciable intensity and with nearly the same $Q_1 - P_2$ head separation as the corresponding normal band. The isotopic (0–0) band is at almost the same frequency as the normal (0–0) band, and buried beneath it, but isotopic (0–1) and (1–2) bands are expected to be shifted by $+6\ cm^{-1}$ from the corresponding normal bands for $\omega'' \sim 860\ cm^{-1}$. This is indeed the shift found in two weaker sets of P_2 and Q_1 band heads, as shown in Fig. 3 and Table III.

If the assignments made here for either the $\Delta v = 0$ or $\Delta v = -1$ sequence bands are interchanged so as to make the stronger band at higher frequency originate at the $v' = 1$ rather than the $v' = 0$ level, very improbable anharmonicities are found for the lower state vibration. The band at 2714 Å can now be identified as the first member of the $\Delta v = +1$ sequence, for the vibrational combination relationship predicts

$$(1\text{–}0) = (1\text{–}1) + (0\text{–}0) - (0\text{–}1) = 36768.4\ cm^{-1},$$

which agrees with the observed frequency of $36768\ cm^{-1}$ for the band.

The predicted frequency of the (0–2) transition is

$$(0\text{–}2) = (1\text{–}2) + (0\text{–}1) - (1\text{–}1) = 34214.0\ cm^{-1}.$$

The 2920 Å band is weak and complex, and its features cannot be identified with certainty; nevertheless, a band of suitable frequency does occur at $34215\ cm^{-1}$.

Values so far obtained for the $v'' = 0, 1$ levels give the ground state constants in Table IV. The first vibrational quantum in the upper state is also found to be 845 cm^{-1}.

TABLE IV

Vibrational constants

	$^2\Delta$	$^2\Pi$
ω_e	860	875.1 cm^{-1}
$\omega_e x_e$	~7.5	7.0 cm^{-1}
D_e	~24,700	27,300 cm^{-1}*

*Calculated from $D_e = \omega_e^2/4\omega_e x_e$.

The remaining peaks in the 2714 Å band at 34246 and 34098 cm^{-1} have roughly the correct separation for a Q_1 and P_2 head. They do not belong to the (1–3) band, since they are more intense than the heads of the (0–2) band, and also this assignment would give 887 cm^{-1} for the third vibrational quantum in the lower state, implying negative anharmonicity. However, if $\omega_e'x_e'$ is given the plausible value of ~7½ cm^{-1}, it can be shown that heads in successive bands in the $\Delta v = -2$ sequence will themselves converge at the observed head frequencies, and that this type of convergence will not occur for successive bands in other observed sequences. This accounts for the relatively high intensity of the two peaks, and is consistent with the rest of the vibrational scheme.

DISCUSSION

In their rotational analysis, Kuzyakov and Tatevsky (1959*b*) ignored low J deviations of lines from parabolic formulae. This led to a wrong numbering of lines in the R_2 and Q_2 branches upon which their analysis is based. Also, these deviations invalidate the band head-origin formulae used in their vibrational analysis (1959*a*).

There remains the possibility that the transition is $^2\Pi(b) \rightarrow {}^2\Pi(a)$, with Λ-type doubling of the branches remaining too small for observation. Additional rotational lines expected near band origins for such a transition were not identifiable, although the resolution was not sufficient for this to be conclusive. The chief argument in favor of a $^2\Delta$ upper state is that the Q branches in the bands have high intensity. In Fig. 2, the Q_2 branch, which is distinct from its satellite R_{12} branch at low J, shows strongly between the wider-spaced lines of the R_2 branch. The high intensity of the head in the Q_1 branch cannot be ascribed to the accompanying satellite P_{21} branch, since it can be calculated that the latter would form a head 1 cm^{-1} to lower frequencies, and such a head does not appear with appreciable intensity.

The upper state is identified as $^2\Delta_i$ rather than $^2\Delta_r$. The lines $Q_2(1.5)$ and $P_2(2.5)$, both originating from the $J' = 1.5$ upper state level, can be assigned in Fig. 2 in the correct positions for an inverted upper state. The alternative values of A' and Y' for a regular state given in Table II would cause both these lines to appear 11.1 cm^{-1} to lower frequencies, where they are not observed.

The lower state of the transition is almost certain to be the ground state of the radical, arising from the . . . $\pi^4\sigma^2\pi$ electronic configuration. The ground state bond length of 1.65 Å lies between the approximate values of 1.72 Å and 1.63 Å for C—Cl bonds adjacent to double and triple bonds respectively (Bowen 1958). Similarly, Andrews and Barrow (1951) found that the ground state internuclear distance for the CF radical was 1.27 Å, slightly less than for double-bonded CF groups (~1.32 Å).

The ground state dissociation energy ($D_0 = \omega_0^2/4\omega_0x_0$) of 3.34 ev is less than the CF value of 4.96 ev as would be expected. The excited state $D_0 \sim 3$ ev gives approximately 4 ev as the difference in energies between the dissociation products in the two states, but this value results from rather drastic extrapolations. Assuming, as Andrews and Barrow have for CF, that the lower state gives normal $C(^3P)$ and halogen (^2P) atoms, then the upper $^2\Delta$ state found here could correlate with either; firstly, the same atomic states $C(^3P)+Cl(^2P)$ as in the ground state; secondly, the states $C(^1D_2)+Cl(^2P)$; or thirdly, highly excited states of both the C and Cl atoms, with the possibilities here too numerous to specify. It is improbable that the extrapolated dissociation energies are sufficiently in error to make their difference equal to zero, but the difference of 1.2 ev required by the second alternative makes this a more likely possibility.

Finally, although the shorter bond length in the excited state is associated with a lower vibrational frequency than in the ground state, the differences in frequency and bond length are only 1–2%. Badger's rule relating bond length and frequency cannot be expected to apply when such small differences are involved. Interestingly, Eyster (1937) specifically mentions the poor results obtained when applying Badger's rule to doublet states of the SiF molecule.

REFERENCES

ANDREWS, E. B. and BARROW, R. F. 1951. Proc. Phys. Soc. A, **64**, 481.
ASUNDI, R. K. and KARIM, S. M. 1937. Proc. Indian Acad. Sci. A, **6**, 328.
BOWEN, H. J. M. *et al.* 1958. Tables of interatomic distances and configuration in molecules and ions (Special Publication No. 11, The Chemical Society, London).
EDLÉN, B. 1953. J. Opt. Soc. Am. **43**, 339.
EYSTER, E. H. 1937. Phys. Rev. **51**, 1078.
HARRISON, G. R. 1939. M.I.T. wavelength tables (John Wiley & Sons, Inc., New York).
HERZBERG, G. 1950. Spectra of diatomic molecules (D. Van Nostrand Co., Inc., Princeton, N.J.).
HORIE, T. 1939. Proc. Phys. Math. Soc. Japan, **21**, 143.
KING, G. W. 1958. J. Sci. Instr. **35**, 11.
KUZYAKOV, YU. YA. and TATEVSKY, V. M. 1959*a*. Nauch. Doklady Vysshei Shkoly, Khim. i Khim. Tekhnol. **2**, 233.
——— 1959*b*. Optika i Spektroskopiya, **7**, 300.
SCHMID, R. 1930. Z. physik. **64**, 84, 279.
VENKATESWARLU, P. 1950. Phys. Rev. **77**, 79.

ON THE THERMAL EXPANSION OF METALS AT LOW TEMPERATURES[1]

G. K. HORTON

ABSTRACT

A theory is developed which correlates the thermal expansion of crystals to the anharmonicity introduced into Born's lattice dynamics by allowing the force constants of the crystal to vary with volume. This is achieved by identifying the force constants with the elastic constants of the crystal by the method of long waves. It is then assumed that it is primarily the volume dependence of the elastic constants that give rise to their temperature variation. A central force nearest and next-nearest neighbor force model analogous to Leighton's is applied to copper. The values of the lattice thermal expansion coefficient and of Grüneisen's parameter are given as a function of the temperature and found to agree quite well with the latest experimental results. It is pointed out that the description of the interionic potential in metals by a two-body central force is certainly a serious oversimplification and that the theory is likely to be more realistic for, say, the ideal inert solid gases, as soon as the experimental data becomes available.

I. INTRODUCTION

The lattice dynamics of Born (Born and Huang 1954) has met with considerable success in those effects that depend primarily on the harmonic contribution to the free energy. Among these I need only refer to the theory of specific heats where Born's theory is able to account for the considerable body of experimental information with reasonable success (Blackman 1955).

Of the various phenomena that depend on the anharmonic terms in the free energy, I wish to discuss the thermal expansion of crystals. This seems appropriate in view of the recent experimental work in this field. In an *ideally harmonic crystal*, e.g. one in which all pairs of atoms attract or repel each other with forces proportional to the distance between them, there would be no thermal expansion. No complete theory of lattice vibrations that takes proper account of anharmonic effects has yet been carried through satisfactorily for a three-dimensional dielectric crystal, much less for a three-dimensional metal. I would like to emphasize that this paper makes no contribution to this problem.

As has been discussed by Salter (1955*b*), Born's lattice dynamics (Begbie and Born 1947) is only quasi-harmonic and, in a certain sense, has anharmonic effects built into it. In this paper I present an investigation of the extent to which a suitably formulated quasi-harmonic theory can account for thermal expansion of crystals. In so doing, I would like to stress the exploratory nature of the discussion. Some version of Born's theory, in which the interionic forces are represented by one general potential function, with due reference to the influence of the conduction electrons (Bhatia 1955; de Launay 1953) on this

[1]Manuscript received February 15, 1960.
Contribution from Rutgers, The State University, New Brunswick, N.J., U.S.A. The work was completed while the author was at the Department of Mathematical Physics, The University, Birmingham 15, England.

potential, may, in principle, be able to account for the low temperature heat capacity of crystals. This may not be true of the thermal expansion and so we probably cannot expect quantitative agreement with experiment.

The theory of the equation of state of crystals is largely due to Mie (1903) and Grüneisen (1912). This theory, in its usual form (Grüneisen 1926), is based on the well-known Debye approximation, leading to Grüneisen's rule that the thermal expansion coefficient and the specific heat of a crystal are proportional. Recently Barron (1955*a*) has studied the effect of replacing the continuum model of Debye by the dynamical version of the nearest neighbor central force theory of Born and von Kármán (1912). Barron found that in his theory, Grüneisen's parameter γ was no longer a constant at intermediate temperatures, though it did approach (different) constant values at high (γ_∞) and low (γ_0) temperatures. The high temperature value γ_∞ depended on the logarithmic volume derivative of the one force constant that enters into the lattice dynamical model used by him. It is left as an arbitrary parameter (which may still vary with temperature through its volume dependence) that has to be found for a given crystal by identifying the experimental and theoretical γ_∞. The temperature dependence of γ in the intermediate region was then a function that depended only slightly on the properties of particular crystals. Using a Mie–Lennard–Jones potential, he also estimated the influence of more distant neighbors: this influence turned out to be quite marked.

In this paper I would like to report on an attempt to use the nearest and next-nearest neighbor central force theory (Leighton 1948) in its dynamical form together with the *experimentally* measured elastic constants. It is in this way that we introduce the major anharmonic effects, including that of the zero point energy, into the theory. The theory presented in this paper ***contains no adjustable parameters*** and yields results that can be compared directly with the experimental results for the crystal whose elastic constants are being used. It is applied to a face-centered cubic metal Cu, because, when the numerical work was started, it was only for this crystal that reliable values for the expansion coefficient, the heat capacity, and the elastic constants were available. I would like to emphasize that this does *not* mean that I believe that the interionic forces in a metal can be described by a central, two-body short range force (cf. Peierls 1955). An application to the heavier inert gas solids would clearly be more realistic when the experimental results are available with sufficient accuracy. The choice of the nearest and next-nearest neighbor central force theory was indicated by two considerations. The first is the reasonable success that this theory enjoys in accounting for the specific heat of Cu and, to a lesser degree, of other noble metals (Horton and Schiff 1959). The second arises from the fact that this theory is the simplest in common use that still permits direct comparison with experiment. The assumption made in the theory that each "shell" of neighbors is separately in equilibrium is made for simplicity in this exploratory study. In future work, especially when the zero point energy plays an important role, it should not be made (Barron 1955*b*).

II. THEORY

The Mie–Grüneisen equation of state is given by

$$PV = \mathscr{D}\Phi + kT \sum_{j=1}^{3N} \gamma_j P(x_j), \tag{1}$$

where Φ is the potential energy of the crystal with the particles at rest in their equilibrium positions, $x_j = \hbar\omega_j/kT$, $P(x) = x/(e^x-1)$,

$$\gamma_j = -\mathscr{D} \ln \omega_j, \tag{2}$$

$\mathscr{D} \equiv V(\partial/\partial V)$, and all other symbols have their usual meaning. ω_j and Φ are functions of the volume only. From the usual thermodynamic relations we find from (1) that

$$\frac{3\alpha}{\chi} = \left(\frac{\partial P}{\partial T}\right)_v = \frac{\gamma C_v}{V}. \tag{3}$$

Here $\alpha = (1/a)[(\partial a/\partial T)_P]$ is the linear thermal expansion coefficient, and $\chi = -(1/V)[(\partial V/\partial P)_T]$ is the isothermal compressibility, a is the nearest neighbor distance and

$$\gamma = \sum_{j=1}^{3N} \gamma_j E(x_j)/C_v, \tag{4}$$

with $E(x) = x^2e^x/(e^x-1)^2$.

The dynamical matrix for our central force theory may be found in Salter (1955*a*). The summations occurring in (4) were replaced by integrals in the usual manner. These integrals were then evaluated by using the modified Houston spherical five-term integration method developed by Horton and Schiff (1959). The error introduced by the use of this method does not amount to more than about one per cent over the whole temperature range considered. To use the integration formula we must solve the secular equation in reciprocal lattice space and insert the resultant dispersion law into the integrals obtained from (4). I will carry through the procedure in the A, or (100), direction as an example of the general method. One finds that

$$(\omega_j^2)^A{}_{\text{long}} = \frac{4}{\rho a^2}[2(2\beta_1+\delta_1)+(\beta_2+\delta_2)p](2-p), \tag{5}$$

$$(\omega_j^2)^A{}_{\text{trans}} = \frac{4}{\rho a^2}[(4\beta_1+\delta_1)+\beta_2 p](2-p), \qquad \text{(twice)}; \tag{6}$$

$p = (1+\cos ka/\sqrt{2})$, ρ is the density, and a is the nearest neighbor distance.

$$\beta_1 = \frac{\rho a^2}{2M}\left[\frac{1}{r}\frac{dW}{dr}\right]_{r=a}, \tag{7}$$

$$\delta_1 = \frac{\rho a^3}{2M}\left[\frac{d}{dr}\left(\frac{1}{r}\frac{dW}{dr}\right)\right]_{r=a}; \tag{8}$$

corresponding expressions for β_2 and δ_2 can be found by replacing a by $\sqrt{2}a$. In the static theory we put the β's (proportional to the first derivative of the interionic potential) equal to zero and, using the usual Fuchs–Fine method, find

$$\begin{aligned} \delta_1 &= c_{44}, \\ \delta_2 &= (c_{11}-c_{12}-c_{44})/2. \end{aligned} \tag{9}$$

Because of the form of (2), we cannot use this procedure here. Clearly, to find the γ_j, all volume differentiations must be carried out before the β's are equated to zero. From (2) we note that

$$\gamma_j = -\frac{1}{6\omega_j^2}\mathscr{D}_a\omega_j^2, \tag{10}$$

and that

$$\mathscr{D}_a\left(\frac{1}{a^2\rho}\right) = \frac{1}{a^2\rho},$$

with

$$\mathscr{D}_a \equiv a\frac{d}{da}.$$

From (7) and (8), and noting the volume dependence of the density, it is easy to show that

$$\mathscr{D}_a\beta_i = (\delta_i-\beta_i). \qquad (i = 1, 2) \tag{11}$$

Next we must consider $\mathscr{D}_a\delta_i$ $(i = 1, 2)$. This expression can be evaluated directly if one assumes a definite function for W. Our problem is to evaluate it subject to (9). We do this with the *assumption* that

$$\begin{aligned} \mathscr{D}_a\delta_i &= a\left(\frac{d\delta_i}{dT}\right)\left(\frac{dT}{da}\right), \\ &= \frac{1}{\alpha}\frac{d\delta_i}{dT}, \end{aligned} \qquad (i = 1, 2) \tag{12}$$

the pressure being constant.

This assumption may be regarded as equivalent to the statement that it is assumed that if the elastic constants were measured at *constant volume* as the temperature varies, they would essentially be temperature independent. We assume that this is a reasonable approximation well below the characteristic temperature. Finally, following Barron (1955*a*), we will ignore the volume dependence of p in (5) and (6). After the appropriate differentiations corresponding to (10) have been carried out, the β_j's can then be equated to zero; they are likely to be very small. In this way we obtain the γ_j corresponding to (5) and (6). They are given by

$$(\gamma_j)^A{}_{\text{long}} = -\frac{1}{6}\left[\frac{2(3\delta_1+\delta_2 p)}{2\delta_1+\delta_2 p}+\frac{1}{\alpha}\frac{2\dot{\delta}_1+\dot{\delta}_2 p}{2\delta_1+\delta_2 p}\right], \tag{13}$$

$$(\gamma_j)^A{}_{\text{trans}} = -\frac{1}{6}\left[\frac{5\delta_1+\delta_2 p}{\delta_1}+\frac{1}{\alpha}\frac{\dot{\delta}_1}{\delta_1}\right], \qquad \text{(twice)}. \tag{14}$$

The dot over the δ's indicates a derivative with respect to the temperature. The results for the other four directions (110), (111), (210), and (211), may be derived in a similar fashion. The values of the elastic constants and their temperature derivatives are taken directly from the experimental results. For the temperature range 0° K to half the Debye characteristic temperature it is convenient to fit the published tables by a quadratic polynomial in T by the usual methods. At very low temperatures this procedure breaks down. The breakdown was traced to the fact that for $T < \Theta/10$ it becomes important to represent the elastic constants by the correct theoretical expression (Born and Huang 1954). In a second calculation I, therefore, wrote

$$c_{ij} = a - bT^4 + cT^6 \qquad (ij = 11, 12, 44). \tag{15}$$

The results of the two calculations can then be used in the respective temperature ranges in which they are valid.

At high temperatures finally we can use the moments method in the form first given by Barron (1955*a*) and Horton and Schiff (1959). We write

$$E(x) = \sum_{n=0}^{3} A_{2n} x^{2n}, \tag{16}$$

with

$$A_0 = 1, \quad A_2 = -0.08320, \quad A_4 = 0.003977, \quad A_6 = -0.000106. \tag{17}$$

Equation (17) has been obtained from (16) by a fitting procedure accurate to about 0.1% in the range $0 \leqslant x \leqslant 3$. All the higher A's are zero. On inserting (16) into (4) we find

$$\gamma = \sum_{n=0}^{3} A_{2n} \gamma_{2n} c_{2n} \Big/ \sum_{n=0}^{3} A_{2n} c_{2n}, \tag{18}$$

where

$$c_{2n} = \mu_{2n} (\hbar/kT)^{2n}, \tag{19}$$

where

$$\mu_{2n} = \frac{1}{3N} \sum_{j=1}^{3N} \omega_j^{2n}, \tag{20}$$

and

$$\gamma_{2n} = -\frac{1}{2n} \mathscr{D} \ln \mu_{2n}, \qquad (n > 0). \tag{21}$$

The case $n = 0$, which gives γ_∞, requires special treatment. Clearly

$$\gamma_\infty = \frac{1}{3N} \sum_{j=1}^{3N} \gamma_j. \tag{22}$$

Equation (22) may be evaluated directly by converting it into an integral. Indeed the integral is just the numerator of (4) with the Einstein function

replaced by unity. Equations (13) and (14) are samples of the integrand that can again be evaluated by the modified Houston method.

For higher terms in (18) we note that after carrying out the indicated differentiations and with

$$\Theta_\infty = \frac{\hbar}{k}\sqrt{\frac{5}{3}\mu_2}, \tag{23}$$

$$\gamma_2 = -\frac{1}{6}\left[4+\frac{1}{\alpha}(4\dot{\delta}_1+\dot{\delta}_2/2)/(4\delta_1+\delta_2/2)\right], \tag{24}$$

$$c_2 = \frac{3}{5}(\Theta_\infty/T)^2. \tag{25}$$

Higher terms in the expansion are similar and will not be reproduced here explicitly.

Both in the high temperature limit and at lower temperatures we see that the results of our analysis of (3) and (4) can therefore be put in the form

$$\alpha = x(q+r/\alpha), \tag{26}$$

where

$$x = \chi/3V. \tag{27}$$

The q and r are quantities that come from the numerator of (4) corresponding respectively to the portion of γ_j in (13), (14), and (24) that is independent of α and that multiplies $1/\alpha$. Equation (26) is quadratic in α with solution

$$\alpha = x\{q/2+\sqrt{[(q/2)^2+r/x]}\}. \tag{28}$$

It can be shown that we must choose the positive sign of the square root in (28) as it corresponds to a higher entropy state, i.e., one with a lower free energy (Varley 1956). We obtain Grüneisen's parameter as a function of temperature from (3), (26), and (28). The result is

$$\gamma = \alpha/xC_v. \tag{29}$$

All the numerical integration was done on the University of Toronto Ferranti I digital computer and on an LGP 30 Royal McBee computer. It is a pleasure to thank Canadian National Telegraphs for making a direct teletype line available to the University of Toronto Computation Center and to thank the National Research Council for free time on Ferut. The integrations were performed at intervals of 10° K by using the wave number integration procedure, combined with Houston's spherical five-term formula and Simpson's rule with 24 intervals at 10° K and 12 intervals at higher temperatures. The detailed procedure is discussed in Horton and Schiff (1959).

III. DISCUSSION OF THE RESULTS FOR COPPER

The elastic constants for Cu were taken from Gaffney and Overton (1955). I used $a = 2.551\times10^{-8}$ cm and $\rho = 8.995$ g/cm^3. The experimental results are those of Rubin, Altman, and Johnston (1954), Simmons and Balluffi

(1957), and White (1960). As the results of the capacitor dilatometer method as used by Bijl and Pullan (1955) seem to contain certain systematic errors at low temperatures, I confine the discussion to the results of the former authors. The thermal expansion coefficient as a function of temperature is given in Fig. 1 while the temperature dependence of Grüneisen's parameter is shown in Fig. 2.

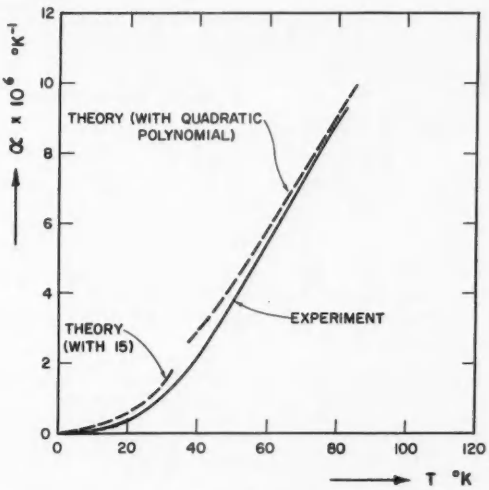

FIG. 1. The linear thermal expansion coefficient of Cu as a function of the temperature. The theory (with quadratic polynomial) refers to the description of the temperature dependence of the elastic constants in terms of a quadratic polynomial in T. Equation (15) incorporates the correct T^4 low temperature dependence of the c_{ij}. This curve is only valid below to 30° K. The experimental curve was obtained from the measurements of Rubin, Altman, and Johnston (1954), Simmons and Balluffi (1957), and White (1960).

It is clear that the theoretical results at higher temperatures lie about 8% above the experimental results. At lower temperatures the values of γ become rather uncertain theoretically as I am trying to calculate the ratio of two quantities that separately tend to zero as T^3. The increase in γ below 40° K is clearly due to this cause and hence probably spurious. In this region the experimental results also become increasingly less accurate. It is nevertheless clear that the dashed curves obtained by using (15) to represent the temperature dependence of the elastic constants leads, as might be expected at very low temperatures, to more reasonable results. At 30° K neither of the two theoretical curves are reliable and an interpolation between the two must be made. In view of the crude theoretical model I feel the agreement between theory and experiment is surprisingly good.

In conclusion I would like to enumerate briefly what seem to me to be the most serious defects of the theory presented above. With regard to the theory in general, it is firstly phenomenological in the sense that I have simply related two phenomena that depend essentially on the anharmonicity of the lattice vibrations, namely the temperature variation of the elastic

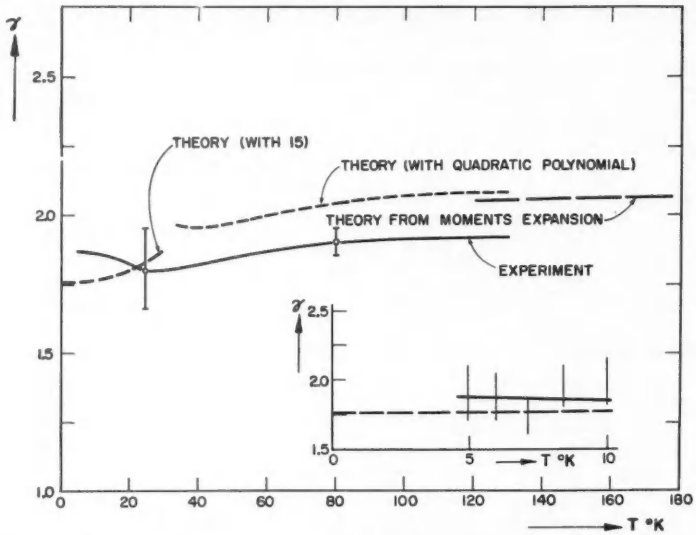

FIG. 2. The temperature dependence of Grüneisen's parameter γ. The theory (with quadratic polynomial) refers to the description of the temperature dependence of the elastic constants in terms of a quadratic polynomial in T. Equation (15) incorporates the correct T^4 low temperature dependence of the c_{ij}. This curve is only valid up to 30° K. The experimental curve was obtained from the measurements of Rubin, Altman, and Johnson (1954), Simmons and Balluffi (1957), and White (1960).

constants and the thermal expansion. A proper theory (Ludwig 1958) would contain an explanation of both phenomena. Secondly the temperature variation of the elastic constants may not be due to the expansion of the solid only. It is likely that any additional corrections are small, however, because the elastic constants of a number of crystals, *at constant volume*, appear to be reasonably constant with temperature. Thirdly the use of the modified Houston method may have introduced errors of one or two per cent especially at low temperatures. Fourthly the assumption of nearest and next-nearest neighbor central forces is a considerable oversimplification. There is no difficulty, in principle, in removing these last assumptions. As far as the application to copper is concerned, this was done purely for the purpose of illustrating the kind of behavior of α and γ that is predicted. Throughout we have ignored the explicit contribution of the conduction electrons to the thermal expansion which is certainly a good approximation for Cu but may be questionable in, say, Al (Varley 1956).

IV. ACKNOWLEDGMENTS

It is a pleasure to thank my colleagues for stimulating discussions, in particular I would like to thank Dr. T. H. K. Barron. I am grateful to Professor R. E. Peierls for his comments on the manuscript. It is a pleasure to thank the National Research Council of Canada for financial assistance.

REFERENCES

BARRON, T. H. K. 1955*a*. Phil. Mag. **46**, 720.
——— 1955*b*. See SALTER, L. 1955. Proc. Roy. Soc. A, **233**, 418.
——— 1957. Ann. Phys. **1**, 77.
BEGBIE, G. H. and BORN, M. 1947. Proc. Roy. Soc. A, **188**, 179.
BHATIA, A. B. 1955. Phys. Rev. **97**, 363.
BIJL, D. and PULLAN, H. 1955. Physica, **21**, 285.
BLACKMAN, M. 1955. Encyclopedia of Physics VII/1, 325.
BORN, M. and HUANG, K. 1954. The dynamical theory of crystal lattices (Oxford University Press, New York).
BORN, M. and VON KÁRMÁN, T. 1912. Physik Z. **13**, 297.
DE LAUNAY, J. 1953. J. Chem. Phys. **29**, 19.
GAFFNEY, J. and OVERTON, W. C. 1955. Phys. Rev. **98**, 969.
GRÜNEISEN, E. 1912. Ann. Physik, **39**, 257.
——— 1926. Handbuch der Physik, **10**, 1.
HORTON, G. K. and SCHIFF, H. 1959. Proc. Roy. Soc. **250**, 248.
LEIGHTON, R. B. 1948. Revs. Modern Phys. **20**, 165.
LUDWIG, W. 1958. J. Phys. Chem. Solids, **4**, 283.
MIE, G. 1903. Ann. Physik, **11**, 657.
PEIERLS, R. E. 1955. The quantum theory of solids (Oxford University Press, New York).
RUBIN, T., ALTMAN, H. W., and JOHNSTON, H. L. 1954. J. Am. Chem. Soc. **76**, 5289.
SALTER, L. 1955*a*. Proc. Roy. Soc. A, **233**, 418.
——— 1955*b*. Unpublished Oxford dissertation.
SIMMONS, R. O. and BALLUFFI, R. W. 1957. Phys. Rev. **108**, 278.
VARLEY, J. H. O. 1956. Proc. Roy. Soc. A, **238**, 413.
WHITE, G. K. 1960. Programme of the VIIth International Conference on Low Temperature Physics, p. 256.

REFRACTION AND DIFFRACTION OF PULSES[1]

W. E. WILLIAMS

ABSTRACT

It is shown that the solution for the reflection and refraction of a plane pulse at a plane interface may be obtained, by Fourier synthesis, from the corresponding solution for a time-harmonic plane wave even when the angle of incidence is such that total reflection occurs. The application of the Fourier superposition method to problems involving both refraction and diffraction is also discussed.

1. INTRODUCTION

It is a standard method in the theory of scattering of waves by obstacles to obtain the solution for incident plane pulses of arbitrary shape by Fourier superposition of the solution for an incident time-harmonic plane wave (for example, Wait 1957). It has, however, been pointed out (Friedlander 1948) that, if the angle of incidence is such that total reflection occurs, this approach breaks down even in the simplest problem of reflection and refraction at an infinite plane interface. The object of the present work is to indicate the method by which the Fourier synthesis approach may be employed to solve this type of problem for all values of the angle of incidence. If a time variation $\exp -i\omega t$ is assumed then it is shown that the reflection and transmission coefficients for the case of total reflection depend on the sign of ω. The results for arbitrary plane pulses can then be deduced from known results in the theory of Fourier integrals. The results are in agreement with these obtained by Friedlander (1948), who obtained the solution in an entirely different manner. The apparent breakdown of the ordinary Fourier superposition method is due entirely to the dependence of the reflection and transmission coefficients on sign ω. This prevents a direct and simple relation being obtained between the incident, reflected, and transmitted waves. The dependence on sign ω is due to the fact that each separate Fourier component, for total reflection, has to be evanescent away from the interface and thus the appropriate form of each component will depend on the sign of ω.

The problem of diffraction of a plane pulse by a half plane at the interface between two media is also discussed. A problem of this type has been considered by Papadopoulos (1959) when the incident wave is a step function. Papadopoulos employs arguments of dynamic similarity in order to effect a solution; this type of argument does not seem to be capable of generalization to plane pulses of arbitrary shape.

The problem for the case of an incident time-harmonic plane wave is of the type which may be solved by the Wiener–Hopf method. It is shown that the results for reflection at a plane interface and the method of Fourier synthesis enable the solution for a plane pulse to be deduced directly from the time-harmonic solution for all values of the angle of incidence.

[1]Manuscript received August 30, 1960.

Contribution from the Department of Applied Mathematics, The University, Liverpool 3, England.

2. REFRACTION OF A PLANE PULSE

The mathematical problem considered is the solution of

$$\frac{\partial^2\phi}{\partial x^2}+\frac{\partial^2\phi}{\partial y^2}-\frac{1}{a_1^2}\frac{\partial^2\phi}{\partial t^2}=0, \qquad y>0, \tag{1}$$

$$\frac{\partial^2\phi}{\partial x^2}+\frac{\partial^2\phi}{\partial y^2}-\frac{1}{a_2^2}\frac{\partial^2\phi}{\partial t^2}=0, \qquad y<0, \tag{2}$$

subject to the conditions

$$b_1\phi_{y=0+}=b_2\phi_{y=0-},$$

$$c_1\left(\frac{\partial\phi}{\partial y}\right)_{y=0+}=c_2\left(\frac{\partial\phi}{\partial y}\right)_{y=0-},$$

where a_1, a_2, b_1, b_2, c_1, c_2 are all real constants. It is assumed that there is incident in the region $y>0$ the plane wave

$$\phi_0=f\left(t-\frac{x\sin\theta+y\cos\theta}{a_1}\right)$$

where t denotes the time. In the present work we are interested in the case when the angle of incidence, θ, exceeds the critical angle, i.e. $a_1<a_2\sin\theta$. The total solution is given by

$$\phi=\begin{cases}\phi_0+\phi_1, & y>0,\\ \phi_2, & y<0,\end{cases}$$

where ϕ_1 and ϕ_2 are solutions of equations 1 and 2 respectively and represent, in some sense, waves going out from the plane $y=0$.

The special case $f(\zeta)=\exp -i\omega\zeta$ will be considered first, the solution for arbitrary f will then be obtained by Fourier superposition. The appropriate forms for ϕ_1 and ϕ_2 are

$$\phi_1=A\exp -i\omega\left\{t-\frac{x\sin\theta-y\cos\theta}{a_1}\right\},$$

$$\phi_2=B\exp -i\omega\left\{t-\frac{x}{a_1}\sin\theta+\lambda y\right\},$$

where

$$\lambda^2=\frac{1}{a_2^2}-\frac{\sin^2\theta}{a_1^2}$$

and A and B are constants. λ is purely imaginary and thus in order to obtain outgoing waves we must have $\lambda=(i\beta/a_1)\operatorname{sgn}\omega$ where $\beta=\sqrt{(\sin^2\theta-(a_1^2/a_2^2))}$ and $\operatorname{sgn}\omega$ denotes the sign of ω.

The formal solution of the boundary value problem is elementary and we obtain

$$\frac{A}{C} = b_2^2c_1^2\cos^2\theta - b_1^2c_2^2\beta^2 + 2ib_1b_2c_1c_2\beta\cos\theta \operatorname{sgn}\omega,$$

$$\frac{B}{C} = 2b_1c_1\cos\theta(b_2c_1\cos\theta + ib_1c_2\beta \operatorname{sgn}\omega),$$

where

$$C = (b_2^2c_1^2\cos^2\theta + b_1^2c_2^2\beta^2)^{-1}.$$

We are now in a position to solve the problem for an arbitrary plane wave, it will be assumed that $f(\zeta)$ possesses a Fourier transform $F(\omega)$ in the ordinary sense, i.e.

$$f(\zeta) = \frac{1}{\sqrt{(2\pi)}}\int_{-\infty}^{\infty} F(\omega)e^{-i\omega\zeta}d\omega.$$

The reflected wave is thus

$$(3)\quad (b_2^2c_1^2\cos^2\theta - b_1^2c_2^2\beta^2)Cf(\zeta) + 2ib_1b_2c_1c_2\beta\cos\theta C\frac{1}{\sqrt{2\pi}}\int_{-\infty}^{\infty} F(\omega)\operatorname{sgn}\omega e^{-i\omega\zeta}d\omega,$$

where $\zeta = t - [(x\sin\theta - y\cos\theta)/a_1]$. From equations 5.1.8 and 5.1.11 of Titchmarsh (1937) it is seen that the above integral is equal to

$$\frac{i}{\pi}P\int_{-\infty}^{\infty}\frac{f(v)}{v-\zeta}dv,$$

where P denotes the principal value. The transmitted wave is

$$(4)\quad b_1c_1\cos\theta C\sqrt{\frac{2}{\pi}}\int_{-\infty}^{\infty} F(\omega)[b_2c_1\cos\theta + ib_1c_2\beta \operatorname{sgn}\omega]$$
$$\exp -i\omega\left(t - \frac{x}{a_1}\sin\theta + \frac{i\beta y}{a_1}\operatorname{sgn}\omega\right)d\omega.$$

From equations 5.13, 5.15, 5.3.5, 5.3.6 of Titchmarsh (1937) we have that

$$(5)\quad \int_{-\infty}^{\infty} F(\omega)\exp -\omega[i\zeta + \mu \operatorname{sgn}\omega]d\omega = \frac{\mu}{2\pi}\int_{-\infty}^{\infty}\frac{f(v)dv}{(v-\zeta)^2+\mu^2},$$

$$(6)\quad \int_{-\infty}^{\infty} F(\omega)\exp -\omega[i\zeta + \mu \operatorname{sgn}\omega]\operatorname{sgn}\omega d\omega = \frac{i}{2\pi}\int_{-\infty}^{\infty}\frac{(v-\zeta)f(v)dv}{(v-\zeta)^2+\mu^2}.$$

Equations 3, 4, 5, and 6 represent the formal solution of the problem. By a suitable choice of the constants b_1, b_2, c_1, c_2 the solution for the reflection of acoustic, electromagnetic, or elastic plane waves may now be obtained. The case $b_1 = b_2$ has been treated by Friedlander and, for this case, the present solution agrees with that of Friedlander, who used a completely different approach. The above analysis is strictly formal and is clearly rigorous when f and its derivatives possess Fourier transforms in the ordinary sense. A similar type of restriction was also imposed by Friedlander. Use of generalized function theory (Lighthill 1958) enables the analysis to be applied to other functions, for example, the Heaviside unit function.

3. DIFFRACTION PROBLEMS

We now consider briefly the application of the results of Section 2 to problems involving both diffraction and refraction. The general boundary value

problem considered is the determination of a solution ϕ of equations 1 and 2, satisfying the boundary conditions of Section 2 on $y = 0$, $x \leqslant 0$ and with ϕ or $\partial\phi/\partial y$ vanishing on $y = 0$, $x \geqslant 0$. Boundary value problems of this type occur in the diffraction of acoustic waves by either a perfectly soft or perfectly rigid semi-infinite screen placed at the interface between two different media. A similar type of boundary value problem occurs in electromagnetic diffraction (Clemmow 1953).

The solution ϕ for an incident plane wave $\exp -i\omega\{t - [(x \sin\theta + y\cos\theta)/a_1]\}$ is easily obtained by Wiener–Hopf methods. ϕ may be written as a sum of the plane wave terms of geometrical optics and a diffracted term. We consider first the diffracted term and examine the form of this in $y \geqslant 0$, the region $y \leqslant 0$ may be treated similarly. From the results of Clemmow (1953) it can be seen that the diffracted field has the form

$$\int_0^\infty e^{(i\omega r/a_1)\cosh v} F(v,\psi)dv,$$

where $x = r\cos\psi$, $y = r\sin\psi$, and F is independent of ω. Fourier superposition thus shows immediately that the diffracted field due to the incident plane pulse ϕ_0 is

$$\int_0^\infty f\left(t - \frac{r}{a_1}\cosh v\right)F(v,\psi)dv.$$

The geometrical optics term due to reflection at $y = 0$, $x \leqslant 0$, is an ordinary plane wave of amplitude ± 1 depending on the boundary conditions imposed. The corresponding term for the plane pulse problem is thus the reflected pulse term of geometrical optics. It thus only remains to consider the geometrical optics terms due to reflection at $y = 0$, $x \geqslant 0$. These have precisely the form of ϕ_1 and ϕ_2 and may be treated in the same manner. Thus, in the time-dependent diffraction problem, we obtain the reflected and refracted pulses of geometrical optics for $a_1 > a_2 \sin\theta$ and the solution for $a_1 < a_2 \sin\theta$ is given by equations 3–6.

The above analysis is quite general and the particular form of $F(v,\psi)$ will depend on the boundary conditions, and obtaining it will involve a complicated Wiener–Hopf factorization. The object of the present work, however, is not to consider a particular case in detail but merely to indicate how the Fourier synthesis technique may be applied, even under conditions of total reflection, to obtain the solution of time-dependent problems from the time-harmonic solutions. It is of interest to note that, when $f(\zeta)$ is the unit step function $H(\zeta)$, the diffracted part of $\partial\phi/\partial t$ has the particularly simple form $H(a,t - r)$ $F(\cosh^{-1}(a_1 t/r),\psi)$; this is precisely the form of solution obtained from arguments of dynamic similarity and conical flow methods.

REFERENCES

CLEMMOW, P. C. 1953. Phil. Trans. Roy. Soc. (London), A, **246**, 1.
FRIEDLANDER, F. G. 1948. Quart. J. Mech. and Appl. Math. **1**, 376.
LIGHTHILL, M. J. 1958. Generalized functions (Cambridge University Press).
PAPADOPOULOS, V. M. 1959. Proc. Roy. Soc. (London), A, **252**, 520.
TITCHMARSH, E. C. 1937. Theory of Fourier integrals (Oxford University Press).
WAIT, J. R. 1957. Can. J. Phys. **35**, 693.

EXCITED STATES OF O^{18} STUDIED BY THE REACTION $H^3(O^{16}_{4+},p\gamma)O^{18}$ [1]

A. E. LITHERLAND,[2] R. BATCHELOR,[3] A. J. FERGUSON, AND H. E. GOVE

ABSTRACT

Gamma rays from the excited states of O^{18} at 3.63 and 3.92 Mev have been observed using the reaction $H^3(O^{16}_{4+},p\gamma)O^{18}$ at an incident O^{16} energy of 14 Mev. Both states were observed to emit gamma rays to the 1.98-Mev 2+ first excited state of O^{18}. No evidence for crossover transitions was found and in each case the crossover transition was estimated to be $\lesssim 15\%$ of the cascade transition. Angular correlations of the gamma rays were obtained and these strongly support an assignment of spin 0 to the 3.63-Mev state and a spin of 2 for the 3.92-Mev state. These assignments have been confirmed by a recent experiment on the $O^{16}(H^3,p)O^{18}$ reaction which gives the assignments 0+ and 2+ for these two states. Thus the states at 3.55, 3.63, and 3.92 Mev form a triplet with assignments 4+, 0+, and 2+ which strongly resembles the vibrational spectra found in heavier nuclei. However, the measured angular correlations of the gamma rays from the 3.92-Mev state show only a small admixture of electric quadrupole in the 1.94-Mev gamma ray with relative amplitude $+0.1\pm.1$. A lower limit of $\sim 10^{-12}$ seconds on the lifetime of the 3.63-Mev state was obtained from the absence of a doppler shift of the 1.65-Mev cascade gamma ray.

INTRODUCTION

The excited states of O^{18} are of particular interest because of the possibility of describing them as the result of the interaction of two neutrons outside the closed shell nucleus O^{16}. Intermediate coupling calculations by Redlich (1954) and by Elliott and Flowers (1955) have been successful in explaining some features of the O^{18} energy level spectrum. Both calculations predict similar sets of low-lying states for the two neutrons in the *s,d* shell: a 0+ ground state and low-lying excited states of 0+, 2+(two), and 4+. Higher excited states of spin 0+, 1+(two), 2+(three), 3+(two), and 4+(one) are also predicted.

The wave functions derived by Redlich for O^{18} have been successfully used in a comparison with theory of the ratios of the reduced stripping widths determined from the $O^{17}(d,p)O^{18}$ reaction by Bilaniuk and Hough (1957). Bilaniuk and Hough concluded that the 1.98- and 3.55-Mev states probably had spins 2 and 4. The parities of these states were found to be even because of the prominent $l = 2$ stripping patterns observed. Subsequently, in a study of the $C^{14}(\alpha,\gamma)O^{18}$ reaction by Gove and Litherland (1959), the 1.98- and 3.55-Mev states were shown to have spins of 2 and 4 as conjectured by Bilaniuk and Hough. The spin of the 1.98-Mev state has also been established by the work of Phillips (1958) on the $C^{14}(\alpha,\gamma)O^{18}$ reaction. Recently Silbert and Jarmie (1959) discovered another level in O^{18} at 3.65 Mev between the known

[1]Manuscript received November 4, 1960.
Contribution from the Physics Division, Atomic Energy of Canada Limited, Chalk River, Ontario.
Issued as A.E.C.L. No. 1157.
[2]At present at Clarendon Laboratories, Oxford, England.
[3]Seconded from the Atomic Weapons Research Establishment, Aldermaston, United Kingdom.

levels at 3.55 Mev and 3.93 Mev (Ajzenberg-Selove and Lauritsen 1959). This new level was strongly excited by the $O^{16}(t,p)O^{18}$ reaction. The available information on the low-lying levels in O^{18} is summarized in Table I, which

TABLE I

The energies of the low-lying states of O^{18} are tabulated together with the known spins and parities. The energy measurements are (*a*) from the tabulation of Ajzenberg-Selove and Lauritsen (1959) and Silbert and Jarmie (1959) and (*b*) Jaffe *et al.* (1960). The spins and parity assignments are from several sources as discussed in the text

	Energy (Mev±kev)	
Spin and parity	(*a*)	(*b*)
0+	0	0
2+	1.982±4	1.979±5
4+	3.55±20	3.552±5
0+	3.65±20	3.634±5
2+	3.93±40	3.915±5
	4.45±50	4.448±5

includes the most recent values of the energies which were measured by Jaffe *et al.* (1960). The energy values quoted by Jaffe *et al.* (1960) are used in this paper.

Since this experiment was completed some preliminary results (Jaffe *et al.* 1960) have become available on the angular distributions of the proton groups from the $O^{16}(t,p)O^{18}$ reaction. Using 5.5-Mev tritons the angular distributions of the protons to the 3.63- and 3.92-Mev states in O^{18} suggested the assignments of 0+ and 2+ for these states. These angular distributions were interpreted on a recent double stripping theory by Newns (1960).

This paper describes the measurement of gamma-ray angular correlations from the 3.63- and 3.92-Mev states and their interpretation in terms of the properties of the states. In Appendix I it is shown that the discovery of a 0+ state 80 kev above the 3.55-Mev state studied by Gove and Litherland (1959) does not alter the spin assignments that they made. In Appendix II an estimate is given of the lifetime of the 3.63-Mev state based on the absence of a doppler shift of the 1.65-Mev reaction gamma ray. It is also pointed out that the type of reaction $H^3(O^{16}_{4+},p)O^{18}$, used in this work is potentially of great value in such lifetime measurements.

EXPERIMENTAL APPARATUS

To produce O^{18} in its various excited states a beam of O^{16} ions was used to bombard a thick tritium target absorbed in a zirconium layer deposited on a thick copper backing. O^{16} ions with three, four, and five electrons removed are readily produced by the Chalk River tandem accelerator. Beams of these ions have previously been used to calibrate the momentum scale of the 90° deflecting magnet of the accelerator by means of the reaction $H^2(O^{16}_{4+},n)F^{17}$ (Gove *et al.* 1958). Currents of approximately 0.4 microampere of O^{16}_{4+} ions were used for

most of the experiments described in this paper. The energy of the O^{16}_{4+} ions used was 14 Mev which is approximately the highest energy that can be used before gamma-ray cascades in F^{18}, from the competing $H^3(O^{16}_{4+},n)F^{18*}$ reaction, interfere with the measurement of the gamma rays from the 3.63- and 3.92-Mev states in O^{18}. The Q-value of the $H^3(O^{16}_{4+},n)F^{18}$ reaction is 1.28 Mev and at 14-Mev bombarding energy the energy in the center of mass system is 2.21 Mev. Consequently only states in F^{18} up to the 3.35-Mev state can be excited.

To produce the 14-Mev O^{16}_{4+} ions, the tandem accelerator accelerates negative oxygen ions to the central positive terminal of the machine. Several electrons are then removed in a gas stripping canal and the resulting positive ions are further accelerated. Charge states other than O^{16}_{4+} have been observed and, for example, currents of approximately 0.15 microampere of 36-Mev O^{16}_{5+} have been used in Coulomb excitation experiments. Small beams of O^{16}_{6+} have also been obtained. C^{12}_{4+} ions are available from the tandem machine when CO_2 is used in the ion source.

After a deflection through 90° by the beam analyzing magnet the O^{16}_{4+} ions then travelled for about 40 feet into a well-shielded room. Two alternating gradient magnetic lenses similar to the type described by Bromley and Bruner (1954) were used to focus the beam over this distance. The well-shielded room contained an angular correlation table which supported two NaI(Tl) gamma-ray detecting crystals: one 5 in. diameter by 4 in. long crystal mounted so that it could rotate about the target in a horizontal plane, and one 5 in. diameter by 6 in. long crystal mounted on another support which permitted it to be moved to any point on a hemisphere centered on the target and lying on and above the horizontal plane of the other counter. At all such points the axis of the gamma-ray counter intersected the target center. The target chamber was constructed so that it had nearly equal gamma-ray absorption properties for all accessible polar angles θ and ϕ of the gamma-ray counters. The distance from the target to the front faces of the crystals was 6.2 inches.

The electronic system used to study the pulses from the Dumont 6365 multipliers which were optically coupled to the NaI(Tl) crystals was a conventional "fast–slow" system (Bell, Graham, and Petch 1952) with a resolving time, 2τ, of 50 nanoseconds. This system permitted a coincident gamma-ray pulse spectrum to be displayed on one 100-channel transistorized pulse-height analyzer and a direct pulse spectrum to be displayed on another 100-channel pulse-height analyzer for monitoring purposes.

For a measurement on the gamma rays in coincidence with the neutrons from the reaction $H^3(O^{16}_{4+},n\gamma)F^{18}$ an NE 212* organic liquid scintillator, 3 in. diameter by 3 in. long was used in conjunction with the 5 in. diameter by 4 in. long NaI(Tl) crystal. To ensure that coincidences between gamma rays were not observed a pulse-shape discrimination circuit of the type described by Owen (1959) was used to eliminate gamma-ray pulses from the neutron counter. The circuit was adjusted so that only neutrons over 800 kev were counted by the detector. This permitted the gamma rays from F^{18} to be

*Obtained from Nuclear Enterprises, Winnipeg, Manitoba, Canada.

identified. For these measurements the neutron detector was placed at 0° to the incident O^{16}_{4+} beam where, because of the large center of mass velocity, it could intercept a larger fraction of the reaction neutrons.

EXPERIMENTAL RESULTS

A portion of the gamma-ray pulse spectrum from the bombardment of H^3 by a beam of 14-Mev O^{16}_{4+} is shown in Fig. 1. The high energy gamma rays

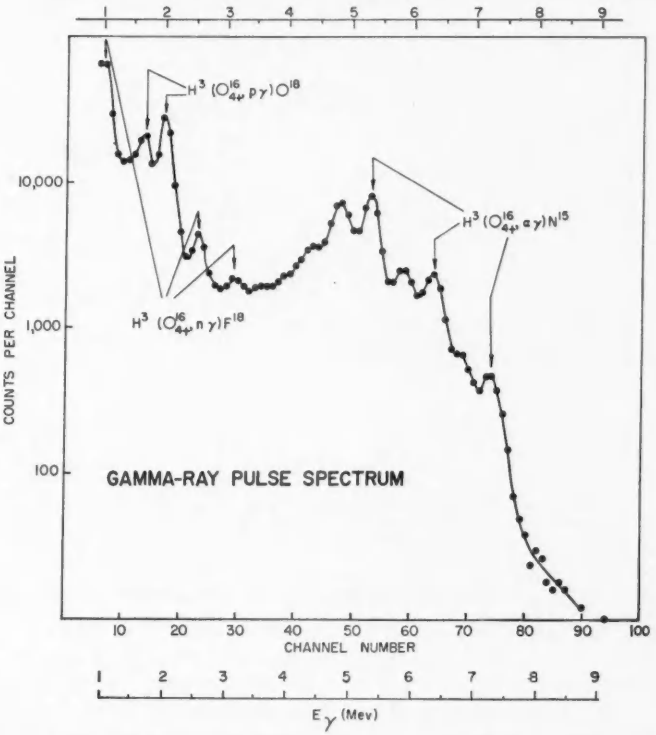

FIG. 1. Part of the gamma-ray pulse spectrum from the bombardment of H^3 by 14.0-Mev O^{16}_{4+} ions.

from the $H^3(O^{16}_{4+},\alpha\gamma)N^{15}$ reaction are easily identified because this reaction has the highest Q-value (7.70 Mev) of the possible reactions emitting heavy particles. Lower energy gamma rays from the $H^3(O^{16}_{4+},p\gamma)O^{18}$ (Q-value 3.73 Mev) and $H^3(O^{16}_{4+},n\gamma)F^{18}$ (Q-value 1.28 Mev) are also observed. The gamma rays from F^{18} were identified by measuring them in coincidence with neutrons. The gamma-ray pulse spectrum in coincidence with these neutrons is shown in Fig. 2. The well-known (Kuehner *et al.* 1958) 0.660, 0.94, 1.08–1.04 complex, 1.70, 2.10, and 2.53 Mev gamma rays can be observed in this spectrum.

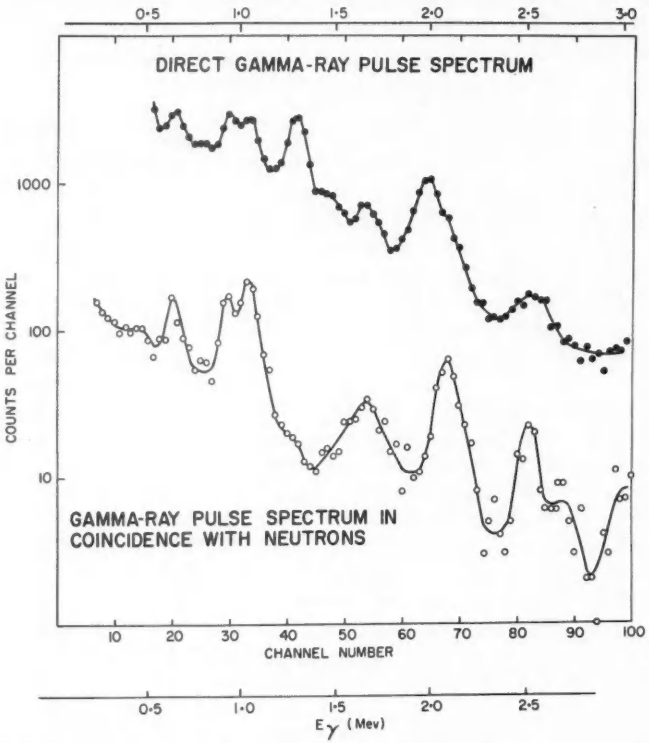

FIG. 2. A portion of the gamma-ray pulse spectrum from the bombardment of H^3 by 16-Mev O^{16}_{3+} ions together with the spectrum in coincidence with fast neutrons from the reaction $H^3(O^{16}_{4+},n)F^{18}$. The 1.29-Mev gamma ray is from the decay of A^{41} produced by the Chalk River NRX reactor. This gamma ray is present during certain meteorological conditions.

Evidence for higher energy gamma rays can also be seen. As a result of this measurement, which was carried out with 16-Mev O^{16}_{3+} ions, the incident oxygen ion energy was reduced to 14 Mev to remove the possibility of coincidences between gamma rays from the 3.725- and 3.790-Mev states in F^{18} interfering with the measurements on the gamma rays from O^{18}. In addition the O^{16}_{4+} beam was used for all subsequent measurements.

To study the gamma rays from O^{18} it was necessary to use the two large NaI crystals in coincidence. Gamma-ray coincidences from F^{18} can be rejected because they lie in the lower channels of the 100-channel analyzer and in addition there are no known cascades in N^{15} which could interfere with the measurements. Coincidence gamma-ray pulse spectra are shown in Fig. 3 together with the relevant portion of the O^{18} energy level diagram. In Fig. 3(*a*), the spectrum of gamma-ray pulses in coincidence with a gate set to include the total absorption peaks of the 1.98- and 1.94-Mev gamma rays is shown.

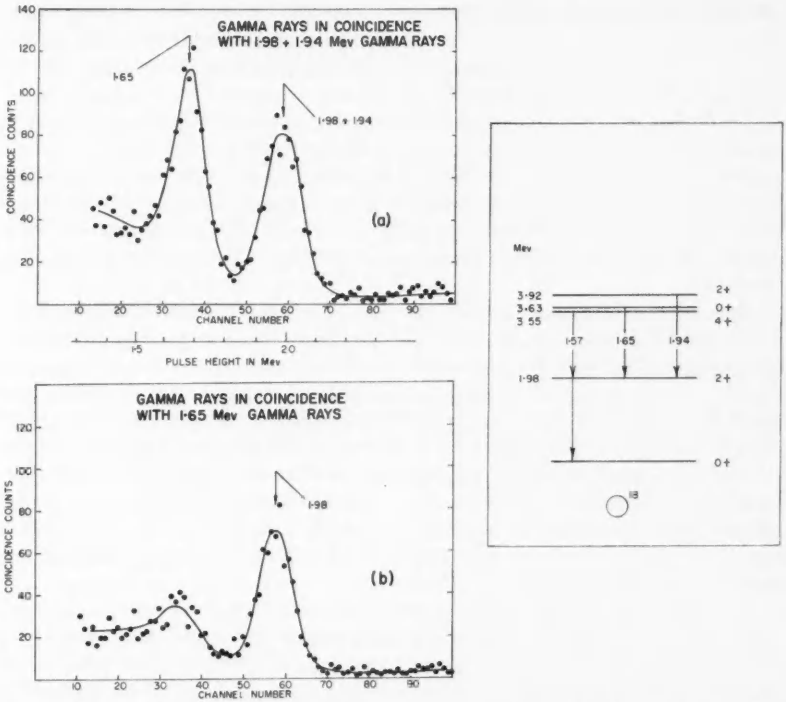

FIG. 3. Typical gamma-ray pulse spectra taken in coincidence. (*a*) The gamma-ray pulse spectrum in coincidence with a voltage gate set to include the 1.98- and 1.94-Mev gamma rays. (*b*) The gamma-ray pulse spectrum in coincidence with a gate set to include the 1.65-Mev gamma rays. The origin of these gamma rays is shown in the energy level diagram which includes the spin assignments made in this paper together with the parity assignments of Jaffe *et al.* 1960.

Both crystals were at 90° to the beam and on opposite sides of the target for this measurement.

In addition to the spectra shown in Fig. 3, spectra were taken with a voltage gate set above the 2-Mev peak. The resulting spectra showed that the 1.65- and 1.98-Mev gamma rays were not in coincidence with gamma rays greater than 2 Mev. Consequently the 1.65- and 1.98-Mev gamma rays cannot come from N^{15}. The pulses greater than 2 Mev in Fig. 3 require some comment as a calculation showed that they could not be random coincidences. It will be noticed from Fig. 2 that the voltage gate includes, in addition to the 1.98-Mev gamma ray, the 2.10-Mev gamma ray from F^{18}. As the 2.10-Mev gamma ray is in coincidence with neutrons there can be genuine neutron – gamma-ray coincidences between the two crystals. However, fast neutrons produce a continuum of pulses rather than a peak in the pulse spectrum and this is observed. The large velocity of the center of mass in the reaction causes the neutrons to be strongly peaked forward in the laboratory. Consequently when

the NaI(Tl) crystal detecting the gamma rays at various angles to the incident beam is placed at 0° the pulses due to fast neutrons in coincidence with gamma rays, should increase in number. This effect was observed and it is shown for example in Figs. 5(*a*) and (*b*).

To obtain the intensity of the gamma rays at each angle it was necessary to subtract the background due to fast neutrons. This was done by assuming that the spectrum of pulses induced by neutrons was the same above and below the gamma-ray peaks shown in Fig. 3. The subtraction of the tail of the 1.98-Mev gamma-ray spectrum line from the 1.65-Mev gamma ray was carried out using the known spectrum line shape of the 1.85-Mev gamma ray from Y^{88}.

Gamma rays of approximately 1.98 and 1.65 Mev appear in the coincidence spectrum. These gamma rays can be interpreted as resulting from cascades from the 3.92- and 3.63-Mev states in O^{18}. This interpretation is supported by the spectrum shown in Fig. 3(*b*). This shows the pulse spectrum from one crystal in coincidence with a gate set to include the total absorption peak of the 1.65-Mev gamma observed in the other crystal. The spectrum confirms the conclusions drawn from Fig. 3(*a*). As will be discussed below, there is a small contribution from the gamma rays from the 3.55-Mev state in O^{18} which results in coincidences between the 1.98-Mev gamma ray and 1.57-Mev gamma rays being observed at angles where the intensity of the 1.65-Mev gamma ray is low.

It is important to consider the energy measurements made with the gamma-ray detectors because it is necessary to be sure that the 3.55-Mev state is not fed strongly at the bombarding energy used. The results of the measurements made by Silbert and Jarmie (1959) on the energy of the protons from the reaction $O^{16}(H^3,p)O^{18}$ are given in Table I together with other measurements quoted by Jaffe *et al.* (1960). Jaffe *et al.* (1960) give a value of 82 ± 7 kev for the energy separation of the 3.55- and 3.63-Mev states. Considerable difficulty was encountered in the measurement of the energies of the gamma rays in this experiment due to photomultiplier gain shifts which were a function of counting rate. Consequently, a counting rate meter was used to ensure comparable counting rates when the reaction was being studied and when the calibration sources were used. Sources of Y^{88} and Pr^{144} were used to provide 1.850 ± 0.008 and 2.185 ± 0.015 Mev calibration gamma rays.

These measurements can be analyzed in two ways: either by evaluating the energy separation of the peaks shown in Fig. 3(*a*), or by evaluating the actual energies. The first procedure is the more accurate and reliable since the energy separation is less sensitive to gain shifts resulting from changing counting rates. The measured energy separation of the two peaks was found to be 307 ± 25 kev. The two calibration sources were used simultaneously to obtain the kev per channel. The energies shown in Table I can be used to calculate the energy separation of the cascade gamma rays from the 3.92-Mev state and those from the 3.55- and 3.63-Mev states. These calculated energy separations are 384 ± 10 kev and 302 ± 10 kev respectively which imply that the 3.63-Mev state is excited more strongly than the 3.55-Mev state as the measured value was

307 ± 25 kev. As will be discussed later there is evidence that the 3.55-Mev state is excited weakly in the reaction.

An analysis of the width of the 1.98-Mev complex shown in Fig. 3(*a*) indicates that the energy separation of the two gamma rays is 20 ± 13 kev. This latter energy separation is in approximate agreement with the value of 43 ± 10 kev deduced from the energies shown in Table I. It should be pointed out that such an analysis is possible in this case because both gamma rays are equal in intensity. This is due to the inclusion of both gamma rays in the voltage window set on one of the counters at 90° to the beam and to the observation of the pulse spectrum shown in Fig. 3(*a*) at 90° to the beam in the other counter.

The energies of the prominent peaks in the spectrum of Fig. 3(*a*) were also determined relative to the 1.850 ± 0.008 Mev and 2.185 ± 0.015 Mev calibration gamma rays. These energies were found to be 1.677 ± 0.025 Mev and 1.983 ± 0.025 Mev. Because the upper peak is composed of two gamma rays which are close together in energy and which cascade from the 3.915 ± 0.005 Mev state the expected peak position is 1.957 ± 0.007 Mev which compares favorably with the measured value. The expected energy of the cascade gamma ray from the 3.634-Mev state to the 1.979-Mev state is 1.655 ± 0.007 Mev which again compares favorably with the measured value. The errors on the measured energies do not include the possibility of an error due to the small difference in average counting rate between the reaction gamma rays and the calibration gamma rays. The fact that the measured energies are both about 25 kev higher than the expected values may be a result of this effect.

The measurements discussed above were considered to be sufficient evidence that the 3.63- and 3.92-Mev states are preferentially excited at the incident energy and target conditions used.

The crossover transitions from the 3.63- and 3.92-Mev states in O^{18} were not observed in spectra such as that shown in Fig. 1. It could be estimated from such spectra that the crossover transitions were less than approximately 15% of the cascade transitions. These crossover transitions could be searched for more easily by observing the gamma rays in coincidence with the appropriate proton group.

The angular correlations of the two complexes of gamma rays were measured in the geometrical arrangements shown in Figs. 4 and 6. The protons leading to the excited states of O^{18} were not observed. As was discussed above, the 1.98-Mev complex consists predominantly of a 1.65-Mev gamma ray and a weak 1.57-Mev gamma ray. For the measurement of the angular correlations a voltage gate was set on the combined total absorption peaks of the 1.98- and 1.94-Mev gamma rays from one counter fixed at 90° and the coincident gamma-ray pulse spectrum observed at various angles (θ,ϕ) of the other counter. The correlations shown in Figs. 4 and 6 are corrected for the varying absorption of the target backing and target chamber walls which is a function of the angles (θ,ϕ). They were also corrected for a small effect due to the beam spot on the target not being at the center of rotation of the counter assembly. These corrections were estimated by observing the angular correlations of the

2.185-Mev gamma rays from a Pr^{144} source placed in the target holder. Small corrections were also made for the aberration effect due to the motion of the source of gamma rays from the reactions. These corrections were in nearly all cases smaller than the statistical errors. The corrected angular correlations were fitted to a function of the form $a_0+a_2P_2(\cos\theta)+a_4P_4(\cos\theta)$ or, in the case of Fig. 6(*b*), of the form $b_0+b_2\cos 2\phi+b_4\cos 4\phi$. The coefficients a_0, a_2, a_4, b_0, b_2, and b_4 have in turn been fitted, as discussed in the next section, to the spin assignments $0\rightarrow 2\rightarrow 0$ for the 1.65 Mev–1.98 Mev correlation and $2\rightarrow 2\rightarrow 0$ for the 1.95 Mev–1.98 Mev correlation. The latter fit was made using a Datatron computer program written by one of the authors (A.J.F.). In measuring the correlations of Figs. 4 and 6, no attempt was made to establish the relative normalizations of the different distributions. The theoretical distributions, which are shown as solid lines, are normalized so as to be continuous at the junctions between them, and the same normalization factors have been applied to the experimental points. The results of the analysis are shown in Table II and Table III.

TABLE II

The experimental coefficients for the angular correlation of the 1.65- and 1.98-Mev gamma rays are compared with theory. For correlation (*a*) the coefficients refer to a correlation which is a function of an angle $90°-\theta_1$

		Experiment	Theory
(*a*)	a_2/a_0	.28±.13	.309
	a_4/a_0	.59±.12	.643
(*b*)	a_2/a_0	.40±.04	.309
	a_4/a_0	.61±.05	.643
(*c*)	a_2/a_0	.21±.06	0
	a_4/a_0	.03±.07	0

TABLE III

The experimental coefficients for the angular correlation of the 1.98- and 1.94-Mev gamma rays are compared with theory for the quadrupole–dipole amplitude mixture ratio $x = 0.1$. The experimental correlations are shown in Fig. 6 together with the theoretical curve

		Experiment	Theory
(*a*)	a_2/a_0	−0.17±.03	−0.158
	a_4/a_0	0.10±.03	0.105
(*b*)	b_2/b_0	0.40±.03	.424
	b_4/b_0	0.06±.03	.002
(*c*)	a_2/a_0	0.58±.06	.529
	a_4/a_0	0.12±.08	.002

ANALYSIS OF THE EXPERIMENTAL DATA

(*a*) *The Correlations of the Gamma Rays from the 3.63-Mev State*

The strong angular correlations shown in Figs. 4(*a*) and (*b*) immediately

suggest the assignment of spin 0 to the 3.63-Mev state in O^{18}. The solid curves shown in Fig. 4 are theoretical curves, for the spin sequence, $0 \rightarrow 2 \rightarrow 0$,

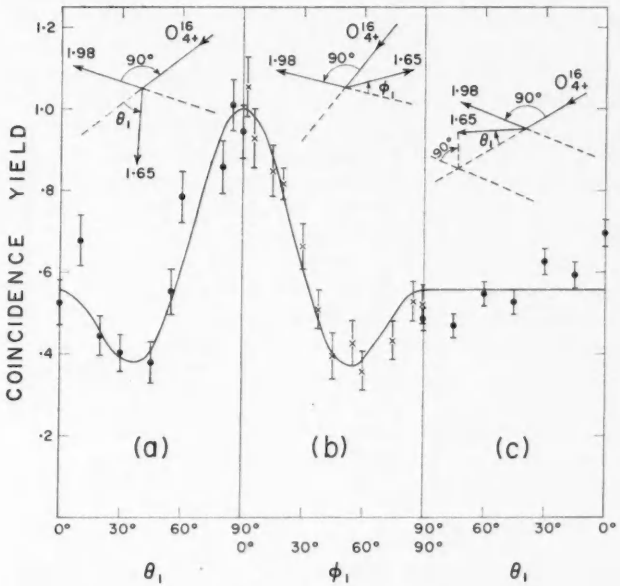

FIG. 4. Gamma-ray angular correlations taken with three geometrical arrangements of the counters shown in the figure. The energies of the gamma rays observed in each counter are also shown. The solid lines on the angular correlations (*a*) and (*c*) are for the spin sequence $0 \rightarrow 2 \rightarrow 0$.

attenuated for the finite sizes of counters employed. Since the initial state of the cascade is assumed to have spin zero, the gamma-ray correlation is that of a decaying radioactive nucleus, and is given by the equation

$$W = 1+(Q_2)^2\, 0.357 P_2(\cos\phi_1)+(Q_4)^2\, 1.143 P_4(\cos\phi_1). \tag{1}$$

The axis of quantization is defined here by the fixed counter and the target, and is different from that assumed below in the analysis of the correlations from the 3.92-Mev state. ϕ_1 of equation (1) is defined as shown in Fig. 4(*b*). The same equation describes the correlation of Fig. 4(*a*) with ϕ_1 replaced by $90°-\theta_1$. The attenuation coefficients Q_2 and Q_4 were taken from the tables of Gove and Rutledge (1958) and Rutledge (1959). The values used in Figs. 4(*a*) and (*c*) were $Q_2 = 0.93$ and $Q_4 = 0.75$. The agreement is very good in Figs. 4(*a*) and 4(*b*). However, there is disagreement in Fig. 4(*c*) because there the predicted correlation is isotropic. The reason for this discrepancy was apparent from the gamma-ray spectra taken for the correlation shown in Fig. 4(*c*). Two gamma-ray pulse spectra for this correlation are shown in Figs. 5(*a*) and 5(*b*). At $\theta_1 = 0°$ in Fig. 5(*b*) the 1.65-Mev gamma-ray total absorption peak is broader than that recorded at $\theta_1 = 75°$ which is shown in Fig. 5(*a*). The

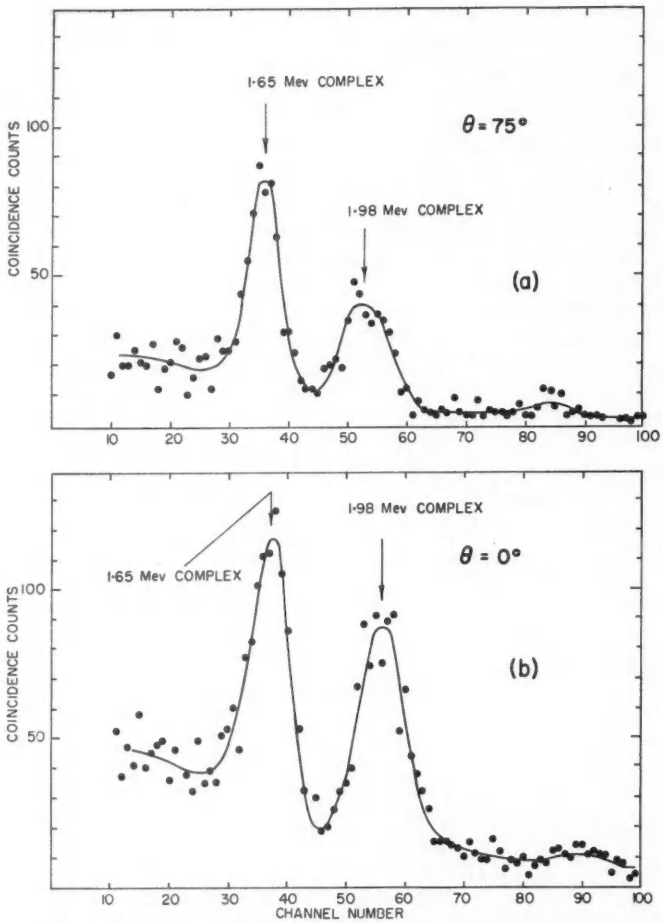

FIG. 5. Typical pulse spectra taken during the angular correlation measurements. The voltage gate was set to include the 1.94- and 1.98-Mev gamma rays. For the spectra one counter was situated at $\theta = 90°$, $\phi = 180°$, and the other was moved in the $\phi = 90°$ plane. This angular correlation is shown in Fig. 6. These spectra show the broadening of the 1.98-Mev complex due to the 1.98- and 1.94-Mev gamma rays from the 3.92-Mev state. In spectrum (*b*) the 1.65-Mev complex is perceptably broadened over that in (*a*) indicating the presence of a weak 1.57-Mev gamma ray from the 3.55-Mev state in O^{18}.

broadening from 6.5 channels in 5(*a*) to 8.5 channels in 5(*b*) can be explained by the appearance of the 1.57-Mev gamma ray from the de-excitation of the 3.55-Mev state in O^{18} with an angular correlation such that it is much stronger at 0° than at 75°. A rough estimate of 25% for the intensity of the

1.57-Mev gamma ray relative to the 1.65-Mev gamma ray at $\theta_1 = 0°$ was obtained from measured spectra. Admixtures of this magnitude of a $4 \rightarrow 2 \rightarrow 0$ correlation having the lower magnetic substates of the 4+ state the most strongly populated are compatible with the anisotropy appearing in Fig. 4(*c*). The effect of such admixtures on the correlations of Figs. 4(*a*) and 4(*b*) will not be great enough to change the conclusions. The good agreement between theory and experiment shown in Fig. 4(*a*) and Fig. 4(*b*) together with agreement shown in Table II can be taken as strong evidence for the spin 0 assignment for the 3.63-Mev state in O^{18}. In Table II the finite value of the correlation coefficient listed in Section (*c*) is attributed to the presence of the weak 1.57-Mev gamma ray as discussed above.

A search for fits to the data assuming the spin sequences $1 \rightarrow 2 \rightarrow 0$, $2 \rightarrow 2 \rightarrow 0$, $3 \rightarrow 2 \rightarrow 0$, and $4 \rightarrow 2 \rightarrow 0$* was made with the aid of the computer program described briefly below. The theoretical Legendre polynomial coefficients given by the best of these were grossly discordant with the measured values and it is concluded that the measured correlations exclude these assignments.

(b) The Angular Correlations of the Gamma Rays from the 3.92-Mev State

The angular correlations of the 1.98+1.94 Mev gamma rays are shown in Figs. 6(*a*), (*b*), and (*c*). The solid curve shown is the theory for the spin sequence $2 \rightarrow 2 \rightarrow 0$ with the first radiation pure dipole. The theoretical angular correlations were calculated in this case using the procedure outlined by Batchelor *et al.* (1960) and discussed in some detail by Litherland and Ferguson (1960). As shown by Litherland and Ferguson (1960) the angular correlation of the gamma rays from an axially symmetrical state J_1, is

$$(2) \qquad W_{tt'}(\theta_1,\theta_2,\phi) = \sum_{KMN} \sum_{s} (-1)^{L_2+L_2'} Q_K Q_M T(s) x^p D^N_{KM}(tt') X^N_{KM}(\theta_1,\theta_2,\phi).$$

In equation (2) the state of spin J_1 decays to a state of spin J_2 by emitting 2^{L_1}-pole radiation. The state of spin J_2 decays to a state of spin I by emitting 2^{L_2}-pole radiation. The first gamma ray is observed at a polar angle θ_1 and the second at θ_2. The azimuthal angle between the two gamma rays is ϕ. The polar axis, i.e. the axis of quantization, lies in the beam direction. The coefficients $D^N_{KM}(tt')$ have been tabulated by Ferguson and Rutledge (1957). The functions $X^N_{KM}(\theta_1,\theta_2,\phi)$ are defined by Ferguson and Rutledge (1957). The attenuation coefficients Q_K, Q_M have been tabulated by Gove and Rutledge (1958) and by Rutledge (1959). The quantities $T(s)$ are used to specify the alignment of the state J_1 and are related to the populations of the magnetic substates of the state J_1 by the equation

*It can be shown that the three measured "geometries" provide only six independent constants. Fits made assuming the spin sequences $3 \rightarrow 2 \rightarrow 0$ and $4 \rightarrow 2 \rightarrow 0$ involve seven parameters. For the $3 \rightarrow 2 \rightarrow 0$ case these consist of one $E2/M1$ ratio, three population parameters, $P(m)$ (see below), and three normalization factors. For the $4 \rightarrow 2 \rightarrow 0$ case no $E2/M1$ ratic is present, but there is an additional population parameter. Thus unique fits cannot be expected for these cases. However, two normalizations may be determined at least approximately, for example, by joining the curves at the common points. To attempt the $3 \rightarrow 2 \rightarrow 0$ and $4 \rightarrow 2 \rightarrow 0$ fits mentioned, the normalizations of Figs. 4 and 6 were used.

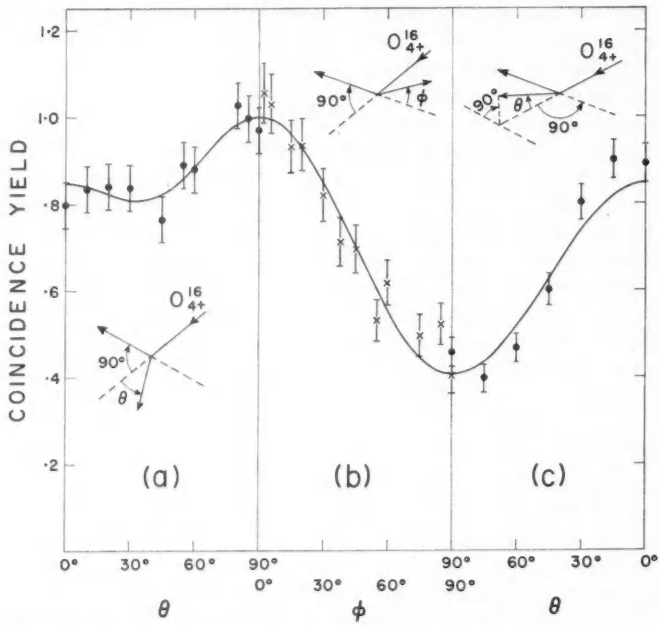

FIG. 6. Gamma-ray angular correlations taken with the three geometrical arrangements of counters are shown in the figure. The two gamma rays of the 1.98-Mev complex could not be resolved so that the correlations of their sum was measured. The solid lines on the angular correlations are for the given sequence $2 \rightarrow 2 \rightarrow 0$.

$$P(m) = \sum_s T(s)(sJ_1m - m|l0)^2. \tag{3}$$

x is the $E2/M1$ amplitude ratio of the first gamma ray and p is an exponent having the value 0, 1, and 2 for the dipole–dipole, dipole–quadrupole, and quadrupole–quadrupole terms respectively.* In equation (3) the quantum numbers satisfy the relation $\mathbf{s}+\mathbf{l} = \mathbf{J}_1$ where the angular momentum quantum number l is chosen so that the $D^N_{KM}(tt')$ coefficients can be obtained from the tables of Ferguson and Rutledge (1957). For the calculations discussed in this paper it was found convenient to choose $l = J_1$.

In the correlations shown in Fig. 6 one of the counters was fixed at 90° to the beam direction. For the arrangement of counters shown in Figs. 6(*a*) and (*c*) equation (2) simplifies to

$$W_{tt'}(\theta) = \sum_r \sum_s T(s)x^p A_r(LL')P_r(\cos\theta) \tag{4}$$

where

$$A_r(LL') = \sum_{KMN} \alpha^N_{rKM} Q_K Q_M D^N_{KM}(tt').$$

*Since the second gamma-ray transition involves the spin sequence $2 \rightarrow 0$, this transition is a pure $E2$ and no mixing parameter is required for it.

The coefficients α^N_{rKM} have also been tabulated by Ferguson and Rutledge (1957). For the case shown in Fig. 6(*b*) equation (2) simplifies to

$$W_{tt'}(\phi) = \sum_N \sum_s T(s) x^p B_N(LL') \cos N\phi \tag{5}$$

where

$$B_N(LL') = \sum_{KM} \alpha^N_{KM} Q_K Q_M D^N_{KM}(tt').$$

The coefficients $A_r(LL')$ and $B_N(LL')$ are tabulated in Table IV of this paper

TABLE IV

The coefficients $A_r(11)$ and $B_r(11)$ of the angular correlations are tabulated for the sequence of spins $2 \rightarrow 2 \rightarrow 0$. The coefficients contain the attenuation factors Q_K discussed in the text

s	0	1	2
(*a*) $A_0(11)$	2.5325	1.8161	2.3825
$A_2(11)$	−0.4135	0.2905	−0.7319
$A_4(11)$	1.2594	−0.6407	0.2746
(*b*) $B_0(11)$	0.8912	0.6740	1.2157
$B_2(11)$	0.7146	0.0413	0.2101
(*c*) $A_0(11)$	1.3231	1.3578	1.9715
$A_2(11)$	1.9893	0.1521	−0.0607
$A_4(11)$	0.0661	−0.0440	0.0189

for the case $L = L' = 1$ and for $J_1 = 2$, $J_2 = 2$, $I = 0$, and $l = 2$. The coefficients apply only to the case where the two gamma rays L_1 and L_2 are not distinguished by the gamma-ray detectors because of their being so close in energy.

Preliminary calculations revealed that the measured Legendre polynomial coefficients of Table III are compatible with the spin sequence $2 \rightarrow 2 \rightarrow 0$ and with a small admixture of quadrupole radiation in the 1.94-Mev transition. This work has been refined by a least squares fit carried out with the Chalk River Datatron, the resulting coefficients being listed in the "theoretical" column of Table III.* The adjustable parameters of this fit were the ratios $T(1)/T(0)$, $T(2)/T(0)$, the quadrupole–dipole amplitude ratio, and, since the relative normalizations of the three different cases were not measured, a normalization constant for each of them. These constitute six parameters to be determined by the nine measured Legendre polynomial coefficients: In Fig. 6 the three theoretical correlations have been renormalized so as to be continuous at the junctions between them and the same normalization constants have been applied to the experimental points.

The results of the fit are as follows: the $E2/M1$ amplitude ratio of the

*It will be noted that two least squares fittings have been made in succession here, the first to obtain the "measured" Legendre polynomial coefficients, the second to obtain the "theoretical" ones. While there are some minor objections to this double process, it is more convenient to program on the computer and more economical of computer time than a program which would fit directly the measured data in terms of theoretical parameters.

1.94-Mev transition is $0.1\pm.1$, the relative populations of the magnetic substate of the initial 2+ state, $P(0):P(1):P(2) = 1:0.67\pm0.17:0.08\pm0.07$. The presence of alignment here implies that the orbital momentum of the incoming particles is greater than zero, and that the compound state has a spin greater than 1/2. The best fits available assuming the spin sequences $1 \rightarrow 2 \rightarrow 0$, $3 \rightarrow 2 \rightarrow 0$, and $4 \rightarrow 2 \rightarrow 0$, were also obtained. For these the theoretical Legendre polynomial coefficients differed from the measured ones by considerably more than the experimental error, so that these possible assignments are eliminated. The sequence $0 \rightarrow 2 \rightarrow 0$ is eliminated because the correlation of Fig. 6(*c*) is not isotropic.

CONCLUSIONS

The experiment described above has obtained further information on the properties of the excited states of the O^{18} nucleus at 3.63 Mev and 3.92 Mev. In addition the measurements reported by Gove and Litherland (1959) on the properties of the 3.55-Mev state are unaffected by the presence of the then unknown 3.63-Mev state. This point is discussed in detail in the Appendix I to this paper.

Measurements of the angular correlations of the cascade gamma rays from the 3.63-Mev and 3.92-Mev states in O^{18} have permitted the assignment of spins 0 and 2 respectively to those states. Also the quadrupole amplitude divided by the dipole amplitude, x, of the 1.94-Mev gamma ray de-exciting the 3.92-Mev state was estimated to be 0.1 ± 0.1. The information obtained on O^{18} as a result of this experiment together with information previously obtained is summarized in Fig. 7. The positive parities of the 3.63- and 3.92-Mev states have been inserted because of the recent evidence from $O^{16}(t,p)O^{18}$ double stripping distributions obtained by Jaffe *et al.* (1960).

The ratios of the energies, and the values of the spins and parities of the first four states in O^{18} are remarkably similar to those found for the vibrational-like states found in medium weight nuclei such as Cd^{144} (Motz 1957). However, the well-studied vibrational states in medium weight nuclei exhibit enhanced electric quadrupole transitions which have not yet been found in O^{18}, with the possible exception of the 4+ to 2+ pure $E2$ transition between the 7.13-Mev and the 1.98-Mev levels which shows some enhancement (Gove and Litherland 1959). The Weisskopf estimate (Wilkinson 1956) of the ratio of the electric quadrupole width to the magnetic dipole width is $\sim10^{-3}$ for the 1.94-Mev gamma ray de-exciting the 3.92-Mev state in O^{18}. However, if O^{18} is considered to be two neutrons attached to the closed shell nucleus O^{16}, electric quadrupole radiation can arise only from the recoil of O^{16} during the gamma-ray transition. The Weisskopf estimate is then multiplied by Z^2/A^4 (Wilkinson 1956) which lowers the ratio to $\sim6\times10^{-7}$. The experimental amplitude ratio of $+0.1\pm0.1$ from the angular correlations shown in Fig. 6 corresponds to an intensity ratio of $\lesssim.04$ which implies an enhancement of $\lesssim10^5$. It is interesting to recall that the 872-kev $E2$ transition from the first excited state of O^{17} is strongly enhanced over the Weisskopf estimate multiplied by Z^2/A^4.

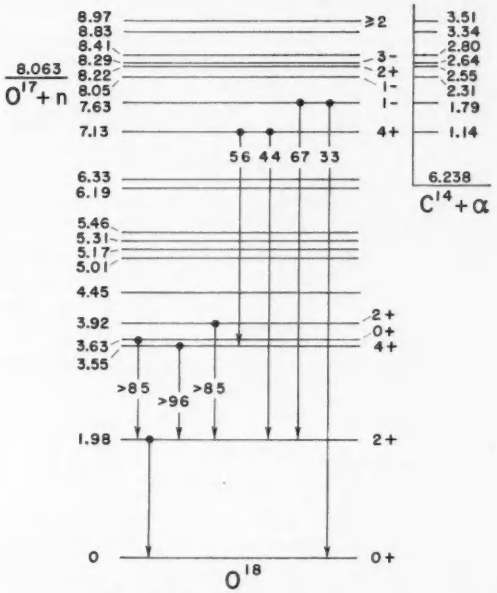

FIG. 7. The known energy levels of O^{18} with the assignments and gamma rays studied in this experiment included.

In conclusion a more accurate experimental determination of the dipole–quadrupole mixing ratio of the 1.94-Mev gamma ray would be of considerable interest together with a determination of the lifetimes of the 1.98-Mev, 3.63-Mev, and 3.92-Mev states in O^{18}. A careful search for the de-excitation of the 3.92-Mev states by means of a ground state transition would also be of value.

ACKNOWLEDGMENTS

We wish to thank Mr. P. G. Ashbaugh and his staff for their successful operation of the accelerator and Mr. C. E. L. Gingell for his assistance with the electronic equipment. We are indebted to Drs. Jaffe and Silbert for communication to us of their results before publication and Dr. C. Broude for valuable comments on the manuscript.

REFERENCES

AJZENBERG-SELOVE, F. and LAURITSEN, T. 1959. Nuclear Phys. **11**, 1.
BATCHELOR, R., FERGUSON, A. J., GOVE, H. E., and LITHERLAND, A. E. 1960. Nuclear Phys. **16**, 38.
BELL, R. E., GRAHAM, R., and PETCH, H. E. 1952. Can. J. Phys. **30**, 35.
BILANIUK, O. M. and HOUGH, P. V. C. 1957. Phys. Rev. **108**, 305.
BROMLEY, D. A. and BRUNER, J. 1954. U.S.A.E.C. Document NYO-3823.
COX, J. A. M. and TOLHOEK, H. A. 1953. J. Appl. Phys. **19**, 1178.
DEVONS, S. and GOLDFARB, L. J. B. 1957. Encyclopedia of physics, **42** (Julius Springer, Berlin), p. 362.

DEVONS, S., MANNING, G., and BUNBURY, D. ST.P. 1955. Proc. Phys. Soc. (London), A, **68**, 18.
ELLIOTT, J. P. and FLOWERS, B. H. 1955. Proc. Roy. Soc. (London), A, **229**, 536.
FERGUSON, A. J. and RUTLEDGE, A. R. 1957. Chalk River Report CRP-615, Chalk River, Ontario, Canada.
GOVE *et al.* 1958. Phys. Rev. Letters, **1**, 251.
GOVE, H. E. and LITHERLAND, A. E. 1959. Phys. Rev. **113**, 1078.
GOVE, H. E. and RUTLEDGE, A. R. 1958. Chalk River Report CRP-755, Chalk River, Ontario, Canada.
JAFFE, A. A., BARROS, F. DE S., FORSYTH, P. D., MUTO, J., TAYLOR, I. J., and RAMAVATARAM, S. 1960. Private communication.
JARMIE, N. 1956. Phys. Rev. **104**, 1683.
KUEHNER, J. A., ALMQVIST, E., and BROMLEY, D. A. 1958. Phys. Rev. Letters, **1**, 260.
LITHERLAND, A. E. and FERGUSON, A. J. 1960. To be published.
MANNING, G. 1955. Thesis. Imperial College of Science and Technology, London.
MOTZ, H. T. 1956. Phys. Rev. **104**, 1353.
NEWNS, H. C. 1960. Proc. Phys. Soc. (London), **76**, 489.
OWEN, R. B. 1959. Nucleonics, **17** (9), 92.
PHILLIPS, W. R. 1958. Phys. Rev. **110**, 1408.
REDLICH, M. G. 1954. Phys. Rev. **95**, 448.
RUTLEDGE, A. R. 1959. Chalk River Report CRT-851, Chalk River, Ontario, Canada.
SILBERT, M. G. and JARMIE, N. 1959. Private communication.
WILKINSON, D. H. 1956. Phil. Mag. Ser. 8, **1**, 127.

APPENDIX I

SPIN ASSIGNMENTS FROM $C^{14}(\alpha,\gamma)O^{18}$

In the $C^{14}(\alpha,\gamma)O^{18}$ reaction at the 1.14-Mev resonance it was assumed by Gove and Litherland (1959) that there were only two primary transitions, that to the level at 1.98 Mev and that to the 3.55-Mev level. With the present information that there is a spin-0 level at 3.63 Mev the possibility exists that both it and the 3.55-Mev level are fed by a primary transition from the resonance in question and that these two primaries of energy 3.48 and 3.58 Mev respectively would be unresolved in the direct spectrum. Coincidence measurements at this 1.14-Mev resonance proved that the level or levels near 3.6 Mev fed by primaries do not de-excite directly to ground thus avoiding the possibility that more than two gamma rays are unresolved at energies near 3.6 Mev in the direct spectrum.

It was shown by Gove and Litherland (1959) in an appendix that the angular distribution of the primary transition from the 1.14-Mev resonance to the 1.98-Mev first excited state requires that the resonance has $J = 2+$ or $4+$. If $J = 4+$ there is no problem since there will be no primary transition to the spin-0 state at 3.63 Mev. However, if the resonance has $J = 2+$ the situation is more complicated. It is easy to show that the resonance cannot be $2+$ by considering what this would imply about the direct angular correlation of the 1.98-Mev gamma ray. As before (Gove and Litherland 1959, Appendix) the correlation of this gamma ray can be corrected for the part due to direct feeding of the 1.98-Mev state by a primary transition from the 1.14-Mev resonance. When the latter has $J = 2+$ the corrected correlation is $W(\theta) = 1+(0.90\pm0.15)P_2-(0.50\pm0.21)P_4$. One can assume that the 3.55-Mev state has any spin value between 0 and 4. Higher spin for the state would result in a vanishingly low probability for a transition from a $J = 2+$ resonance. Spin 0 can be eliminated since a correlation of the type $2+$ ($E2$) $0+$ ($E2$) $2+$ ($E2$) $0+$ with the first two gamma rays unobserved is

spherically symmetric. For spin 1 there would be no P_4 term in the correlation whereas a large one is required experimentally. For spin 2, one can show that the maximum value of the coefficient of P_2 is $+0.178$ for any combination of dipole, quadrupole mixtures in the first two radiations. This is already too small and any feeding of the spin-0 state at 3.63 Mev adds in a spherically symmetric distribution which makes it even smaller. Similarly for spin 3 the maximum P_2 coefficient is $+0.49$ which is again too small. There remains only the possibility that the 3.55-Mev level has spin 4 with spin 2 for the 1.14-Mev resonance. In this case the theoretical correlation $2+$ $(E2)$ $4+$ $(E2)$ $2+$ $(E2)$ $0+$ with the first two gamma rays unobserved is $W(\theta) = 1+0.40P_2 -0.14P_4$. If the 3.63-Mev state is fed as well one must add a spherically symmetric distribution to this which reduces both coefficients and puts them even more outside the required values. If the 3.63-Mev state is not fed, the arguments employed by Gove and Litherland (1959) do not permit the combination spin 2 for the 1.14-Mev resonance and spin 4 for the 3.55-Mev level. Hence the spin assignments made by Gove and Litherland (1959) are unchanged by the discovery of a spin-0 level at 3.63 Mev.

APPENDIX II

Although the triton energy in the center of mass system is only about 2.2 Mev, when 14-Mev O^{16}_{4+} ions bombard H^3, the center of mass has a velocity of about 1.1×10^9 cm per second in the laboratory. This implies large ($\sim3\%$) doppler shifts of the gamma rays from the residual O^{18} nuclei because they will be travelling at approximately the velocity of the center of mass. The large velocity of the recoiling nuclei from reactions with light elements induced by O^{16} ions makes it possible in principle to use a technique described by Devons, Manning, and Bunbury (1955) to measure the lifetimes of the resulting excited nuclear states. They showed that it is possible to estimate the lifetime of an excited state produced in a nuclear reaction by observing the attenuation of the doppler shift when the recoiling nucleus is slowed down in a solid. The method is most successful when the slowing down time in the solid is of the order of the lifetime to be measured. For example, using the data given by Manning (1955) an O^{16} ion travelling initially at 10^9 cm/sec in copper comes to rest in approximately 10^{-12} sec. In the experiment described in this paper this method was not exploited because suitable targets were unavailable. It was possible, however, to obtain a lower limit for the lifetime of the 3.63-Mev state in O^{18} from the measured spectra.

The gamma-ray spectra which were used to determine the angular distributions shown in 4(b) and 4(c) were scrutinized for energy shifts. No significant, $<1\%$, shift for either gamma ray was observed for the sequence of spectra taken to obtain Fig. 4(b). This is to be expected as both gamma-ray counters are at 90° to the incident oxygen beam. The spectra upon which Fig. 4(c) is based were, however, taken with one of the gamma-ray counters at a variable angle θ to the beam. Again no significant, $<1\%$, shift between $\theta = 0°$ and $\theta = 90°$ was observed for the 1.65-Mev gamma ray but a shift of $\sim1.8\pm1.0\%$ was observed for the 1.98-Mev complex of gamma rays.

As the target was a thick one it is not possible to estimate the average doppler shift before the recoiling O^{18} ions start to slow down in the backing. However, because the Coulomb barrier to the H^3+O^{16} reaction causes th. yield of the reaction to fall rapidly as the energy of the oxygen ions is decreased the average doppler shift is expected to be near the maximum value of about 3%. Consequently the $<1\%$ doppler shift observed for the 1.67-Mev gamma ray implies that most of the recoiling nuclei have slowed down before the gamma rays from the 3.63-Mev state in O^{18} are emitted. The slowing down time for an O^{18} ion of initial velocity 10^9 cm/sec in copper is approximately 10^{-12} sec which is therefore an approximate lower limit to the lifetime of the 3.63-Mev state in O^{18}.

The $\sim 1.8 \pm 1.0\%$ shift of the 1.98-Mev complex of gamma rays is consistent with the 1.94-Mev $M1$ gamma ray showing the full doppler shift of $\sim 3\%$ and the 1.98-Mev $E2$ gamma ray showing no doppler shift.

It should be emphasized that these estimates are included merely as a by-product of the data taken for the angular correlations. Much better estimates of the lifetimes could be obtained if it was possible to obtain thin tritium targets (*a*) in zirconium thin to the incident oxygen ions, (*b*) in thin zirconium backed with calcium, and (*c*) in thin zirconium backed with copper.

AN ITERATIVE METHOD FOR NEUTRON TRANSPORT PROBLEMS WITH SPHERICAL SYMMETRY[1]

W. R. CONKIE[2]

ABSTRACT

An iterative method developed previously for transport problems with plane symmetry has been extended to problems with spherical symmetry. Particular application has been made to the problem of the neutron distribution for a black sphere embedded in a purely scattering medium with sources at infinity. The results compare favorably with those of other workers for this problem.

1. INTRODUCTION

For many of the problems of interest to reactor physicists the stationary neutron distribution in a reactor can be mathematically described as being a solution of the transport equation (Davison 1957)

$$(1.1) \qquad v\boldsymbol{\Omega} \cdot \nabla N(\mathbf{r},v\boldsymbol{\Omega}) + \frac{vN(\mathbf{r},v\boldsymbol{\Omega})}{l_{tot}(v)} = \int K(\mathbf{v},\mathbf{v}')N(\mathbf{r},v'\boldsymbol{\Omega}')dv'd\Omega' + S(r,v\boldsymbol{\Omega}).$$

In this equation $N(\mathbf{r},v\boldsymbol{\Omega})$ is the probable number of neutrons in the volume element dV around the point $\mathbf{r}$, with velocity $\mathbf{v} = v\boldsymbol{\Omega}$, where v is the magnitude of the velocity. $l_{tot}(v)$ is the total mean free path, and $K(\mathbf{v},\mathbf{v}')$ is the differential scattering probability for scattering from $\mathbf{v}'$ to $\mathbf{v}$. S represents any sources which are present and we have assumed cross sections independent of $\mathbf{r}$.

It is usually very difficult to obtain accurate solutions to this equation and it is necessary to turn to approximate methods of solution which in many cases have only a limited range of application. For example, for slowing down problems the Greuling–Goertzel method (Greuling *et al.* 1953) has been useful, and for thermalization problems a method combining the spherical harmonics method with polynomial approximations in the velocity variable has been applied to a simple problem with plane symmetry (Conkie 1960*a*). However, these methods and others suffer from their restriction so far to a P_1 approximation (Davison 1957, Chapter X *et seq.*). That is, the neutron distribution consists only of a spherically symmetric term plus a term linear in the directional cosines of the angular variable Ω. Improvements in this approximation can in principle be made. For example, for the thermalization problem mentioned above (Conkie 1960*a*) the extension to higher P_N approximations is straightforward but will involve a large amount of computational labor. Also, for many problems the usual form of the spherical harmonics method is slowly convergent and this may not be the best way to improve the accuracy of these various approximate methods.

Since it is relatively easy to find low order spherical harmonics approximations for various problems we might consider iterative methods of improving

[1]Manuscript received October 28, 1960.
Contribution from the Theoretical Physics Branch, Atomic Energy of Canada Limited.
Issued as A.E.C.L. No. 1160.
[2]Present address: Department of Physics, Queen's University, Kingston, Ontario.

these solutions, since the operators forming the transport equation (1.1) are easy to apply to the solutions usually obtained.

To this end of developing more accurate solutions of the transport equation from low order spherical harmonics approximations, the author has been developing an iterative method for solving the transport equation, and has already applied this method to the Milne problem of one velocity-group transport theory or radiative transfer (Conkie 1959).

The present work still remains within the limits of one velocity-group theory, but extends the iterative method to problems with spherical symmetry. We will consider in particular the problem of the neutron distribution around a black sphere embedded in a purely scattering medium with neutron sources far from the sphere. This problem has been treated before by various methods (Davison and Kushneriuk 1946; Davison 1951) including the spherical harmonics method. This method does not give accurate results for a sphere of small radius even in high order approximations. We will focus attention on the calculation of the linear extrapolation length, λ, which is defined as

$$\lambda = \frac{\rho_{as}(r)}{(d/dr)\rho_{as}(r)}\bigg|_{r=a} \tag{1.2}$$

where $\rho_{as}(r)$ is the asymptotic neutron flux and a is the radius of the sphere. The parameter λ is useful in obtaining the correct ratio of flux to its derivative in the diffusion theory approximation. It should be noted that although we will calculate only λ in detail, the complete neutron distribution should be obtained from our results with an accuracy equal to that with which we obtain the values of the extrapolation length.

In Section 2 we recapitulate the main features of the iterative method applied to problems with plane symmetry. This will serve to illustrate the concepts necessary for carrying out the procedure, and the approach will be somewhat different from the previous exposition (Conkie 1959).

In Section 3 we extend the method to a problem with spherical symmetry, the black sphere problem, with emphasis on the linear extrapolation length.

Section 4 contains the comparison of the results of Section 3 with those of other workers and the conclusions derived from these comparisons.

In Section 5 we discuss the extension of the method to general multilayer problems with spherical symmetry.

Section 6 contains conclusions as to the general applicability of the method.

2. PROBLEMS WITH PLANE SYMMETRY

For problems with plane symmetry the one group source-free transport equation with isotropic scattering is (Davison 1957)

$$\mu\frac{\partial\psi(x,\mu)}{\partial x}+\psi(x,\mu) = \frac{c}{2}\int_{-1}^{1}\psi(x,\mu')d\mu'. \tag{2.1}$$

$\psi(x,\mu)$ is the angle-dependent flux, usually called the angular distribution, μ is the cosine of the angle between the x direction and the direction of velocity, c is the mean number of secondaries per collision, and distances are measured in units of the mean free path.

The flux, $\rho(x)$, is given by

$$\rho(x) = \int_{-1}^{1} \psi(x,\mu)d\mu.$$

It is possible to solve equation (2.1) by the spherical harmonics method, which for this problem consists of expanding the angular distribution in the form

$$\psi(x,\mu) = \sum_{n=0}^{N} \psi_n(x)\frac{(2n+1)}{2}P_n(\mu)$$

where the $P_n(\mu)$ are the Legendre polynomials and the expansion is truncated at the Nth polynomial.

By this means the integrodifferential equation (2.1) is replaced by a system of $(N+1)$ coupled differential equations, which are readily solved for the moments $\psi_n(x)$ in the form

$$\psi_n(x) = \sum_j g_n(\nu_j)e^{\nu_j x}$$

where the $g_n(\nu_j)$ and the exponents ν_j depend on the order of approximation attempted (Davison 1957, Chapter X).

It should be noted that there are two main sources of error in applying the usual form of the spherical harmonics method. First, there is the error of truncating the infinite system of differential equations to $(N+1)$ equations. Secondly, instead of satisfying the exact boundary conditions of the problem being considered, with the complete neutron distribution being continuous across an interface, we use the approximation that only certain angular moments of the distribution be continuous.

We can expect, in deriving solutions in this approximation, that the flux is determined more accurately than the higher angular moments, since it is an integral over the approximate angular distribution and presumably the error in the angular distribution is oscillatory because of our orthogonal functions expansion.

This suggests putting the P_N approximation to the flux, $\rho_N(x)$, in place of the integral in equation (2.1) and simply solving the resulting differential equation.

$$\mu\frac{\partial\psi(x,\mu)}{\partial x} + \psi(x,\mu) = \frac{c}{2}\rho_N(x). \tag{2.2}$$

This will give us an improved result for $\psi(x,\mu)$, which can be made to satisfy the exact boundary conditions of the problem. This improvement of the distribution at the boundary is illustrated for the particular case of the Milne problem by Kourganoff (1952, p. 99). This type of iteration has been considered by various other authors previously and it was found in most cases that although $\psi(x,\mu)$ was improved considerably, the flux, $\rho(x)$, was not improved very much in one iteration. That is, it was mostly the higher moments of the distribution which were improved. The main effect of this method seems to be that of improving the angular distribution, especially at the surface of the

region being investigated. In other words this scheme will largely compensate the second source of error mentioned above, but the errors due to truncation of the infinite system of equations still remains. This last statement is confirmed by the fact that the exponents ν_j, which depend strongly on the order of approximation, remain unchanged by this iteration.

Let us now consider a method of solving equation (2.1), which involves no truncation. To this end we will consider the Fourier transformed form of equation (2.1)

$$(1-i\mu k)\phi(k,\mu) = \frac{c}{2}\int_{-1}^{1}\phi(k,\mu')d\mu' + S(\mu) \tag{2.3}$$

where

$$\phi(k,\mu) = \int_{-\infty}^{\infty} e^{ikx}\psi(x,\mu)dx$$

and

$$S(\mu) = \mu\psi(0,\mu) - \mu\psi(a,\mu),$$

where for definiteness we have considered the neutron distribution in an infinite slab, bounded by the planes $x = 0$ and $x = a$. We have defined $\psi(x,\mu)$ to vanish outside the slab, and consequently the surface terms which make up $S(\mu)$ appear as source terms in equation (2.3). This technique for replacing a finite medium problem by an infinite medium problem is discussed more fully by Case, deHoffman, and Placzek (1953, Section 17).*

Equation (2.3) can now be solved for $\phi_0(k)$, the Fourier transform of the flux $\rho(x)$, by dividing through by $(1-i\mu k)$ and integrating over μ. We obtain then

$$\phi_0(k) = \left\{1 - \frac{c}{k}\tan^{-1}k\right\}^{-1}\int_{-1}^{1}\frac{S(\mu)}{1-i\mu k}\,d\mu \tag{2.4}$$

and

$$\rho(x) = \frac{1}{2\pi}\int_{-\infty}^{\infty}\phi_0(k)e^{-ikx}dk.$$

If $S(\mu)$ is known, the integration in equation (2.4) can be done and the inverse Fourier transform of $\phi_0(k)$ taken using the methods of contour integration. The type of contour used is shown in Fig. 1 (CHP, Appendix C). If the contour is taken in the upper half plane, and $c < 1$, $[1-(\tan^{-1}k)/k]^{-1}$ has a pole at $k = i\kappa_0$ and a branch point at $k = i$. Thus we get a contribution from the pole at $k = i\kappa_0$ and from integrating along both sides of the branch cut extending from $k = i$ to $k = i\infty$. The result for $\rho(x)$ is obtained in the form

$$\rho(\xi) = \rho_{as}(\xi) + \rho_{non\text{-}as}(\xi),$$

where $\rho_{as}(\xi)$, the so-called asymptotic part of the solution is given by

*Hereafter this reference will be called CHP.

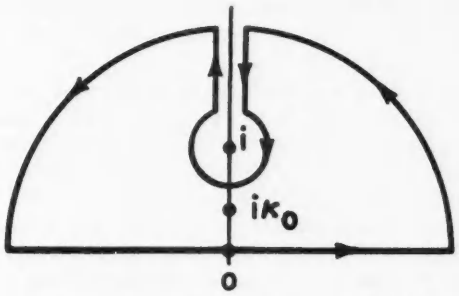

FIG. 1. The form of contour required for evaluating $\rho(x)$ from $\phi_0(k)$ given by equation (2.4).

$$\rho_{as}(\xi) = -c\frac{\partial \kappa_0}{\partial c}\int_{-1}^{1}\frac{S(\mu)d\mu}{(1\mp\kappa_0\mu)}e^{\mp\kappa_0\xi}. \tag{2.5}$$

$\rho_{\text{non-as}}(\xi)$ is the non-asymptotic solution, sometimes known as the transient part of the solution, since it represents terms which die off rapidly as we move away from a source or boundary, and is given by

$$\rho_{\text{non-as}}(\xi) = \int_0^{\pm 1} d\mu g(c,\mu)e^{-\xi/\mu}\left\{\frac{S(\mu)}{\mu} - \int_{-1}^{1}\frac{S(\mu')-S(\mu)}{(\mu'-\mu)}d\mu'\right\}. \tag{2.6}$$

In these equations the upper and lower signs hold for $\xi > 0$ and $\xi < 0$ respectively and $\xi = x$ or $(x-a)$ depending on the term of our particular $S(\mu)$ which is being used in the above integrals. $g(c,\mu)$ is defined in CPH, Section 14, and is also given in Appendix II.

We see then that as long as $S(\mu)$ is known we can find our solution. Unfortunately $S(\mu)$ is not known, but depends on the solution of equation (2.1), which we are trying to find. However, since we know that solving equation (2.2) with accurate boundary conditions leads to much improved surface distributions, we can try using the improved $S(\mu)$ calculated from equation (2.2), in equations (2.5) and (2.6).

The iterative method which we propose consists then of three steps.

(1) We determine a low order spherical harmonics approximation to the neutron flux.

(2) We use this flux as a source term in equation (2.2), whence we improve the angular distribution, satisfying the boundary conditions of our problem accurately at the various surfaces.

(3) We use these improved surface distributions as source terms in the Fourier transformed transport equation from which we can obtain an improved neutron flux. In practice this amounts to using the isotropic and anisotropic plane and point source distributions of CHP, together with the theorem given in Section 17 of that work.

With respect to the two sources of error in the usual spherical harmonics method discussed previously, we see that step 2 attempts to improve the accuracy with which the boundary conditions are satisfied and thus to give

better surface terms. In step 3 the improved surface terms are then used in a complete solution of the transport equation which involves no truncation errors.

It should be noted that by introducing step 3 we get the correct form of solution as given by equations (2.5) and (2.6) with the exact exponent, or reciprocal diffusion length, in the asymptotic solution and the continuous spectrum of exponents, $1/\mu$, in the non-asymptotic solution.

In principle steps 2 and 3 could be repeated to carry out more iterations, but for most problems this would become laborious and we shall see that good accuracy can usually be obtained from just one stage of this process.

As an example of this iterative process we will consider the calculation of the neutron distribution in the Milne problem. The results for the quantity called the extrapolated end point, z_0, are easily calculated in various P_N approximations of the standard spherical harmonics method. A description of the Milne problem and definition of the extrapolated end point together with various P_N results for this quantity are given by Weinberg and Wigner (1958). The results for z_0 for several P_N approximations for a pure scatterer ($c = 1$) are given in Table I.

TABLE I

Values of z_0 for various P_N approximations. $c = 1.0$

N	1	3	5	7	15
z_0	.5774	.6940	.7039	.7069	.7096

The exact value to four figures is $z_0 = .7104$.

The details of the iterative method applied to the P_1 solution have been given elsewhere (Conkie 1959) and the result is $z_0 = .7113$. It is also found that other parameters of the distribution obtained from the iterative method are given with equal accuracy, which should be sufficient for most practical purposes.

We see then, that by iterating the P_1 solution, which is easily obtained, we can obtain results which are as accurate as the P_{15} results for this problem. It should be appreciated that there is a great amount of computing involved in calculating the P_{15} solution for this relatively simple energy-independent problem.

3. CALCULATION OF THE FLUX FOR THE BLACK SPHERE PROBLEM*

Instead of developing the iterative method for general problems with spherical symmetry, we will consider the specific problem of a black sphere embedded in a purely scattering medium with neutron sources far removed from the sphere. We will concentrate on the calculation of the linear extrapolation length, λ, defined by equation (1.2), although, as will be seen, the complete neutron distribution can be obtained from our results.

The P_1 result for the flux for this problem is readily calculated (Mark 1957),

*A preliminary account of this work was presented at the June 1960 meeting of the American Nuclear Society (Conkie 1960*b*).

and using Mark's boundary conditions that the angular distribution at the surface of the sphere should vanish at the positive root of $P_2(\mu) = 0$, we get

$$\rho_N(r) = \left(\frac{q_0}{a^2} + \frac{1}{a}\right) - \frac{1}{r}, \qquad N = 1 \tag{3.1}$$

where a is the radius of the sphere expressed in units of the mean free path of the scattering medium and $q_0 = 1/\sqrt{3} = .5774$. Then

$$\lambda = [q_0/a^2]/[1/a^2] = q_0 = .5774, \qquad \text{for all } a.$$

Carrying on to step 2 of our iterative procedure, we will use $\rho_N(r)$ given by equation (3.1) as a source term in

$$\boldsymbol{\Omega} \cdot \nabla\psi(\mathbf{r},\boldsymbol{\Omega}) + \psi(\mathbf{r}, \boldsymbol{\Omega}) = \frac{c}{4\pi}\int \psi(\mathbf{r}, \boldsymbol{\Omega}')d\Omega', \tag{3.2}$$

which leads to the equation

$$\boldsymbol{\Omega} \cdot \nabla\psi(\mathbf{r},\boldsymbol{\Omega}) + \psi(\mathbf{r},\boldsymbol{\Omega}) = \frac{c}{4\pi}\rho_N(r), \tag{3.3}$$

for our problem with spherical symmetry.

The solution of this equation, which we will call the improved angular distribution is given by

$$\psi_{\text{imp}}(\mathbf{r},\boldsymbol{\Omega}) = \psi_{\text{imp}}(r,\mu) = \frac{c}{4\pi}\int_0^\infty e^{-R}\rho_N(\mathbf{r}-R\boldsymbol{\Omega})dR, \tag{3.4}$$

where $\mu = \boldsymbol{\Omega} \cdot \mathbf{r}/r$.

In our case, with $c = 1$

$$\psi_{\text{imp}}(r,\mu) = \frac{1}{4\pi}\left\{\frac{q_0}{a^2} + \frac{1}{a} - \int_0^\infty \frac{e^{-R}dR}{\sqrt{(R^2+r^2-2rR\mu)}}\right\} \tag{3.5}$$

with the surface condition

$$\psi_{\text{imp}}(r,\mu)\,|_{r=a} = 0, \qquad \mu > 0. \tag{3.6}$$

Since we will need only the results from equation (3.5) at the surface of the sphere, where condition (3.6) holds, an expansion of $\psi(a,\mu)$ in shifted Legendre polynomials, adjusted to the range $-1 \leqslant \mu \leqslant 0$ (Lanczos 1956) is suitable for further calculations.

In practice only the third term on the right-hand side of equation (3.5) needs to be expanded to give

$$\int_0^\infty \frac{e^{-R}dR}{\sqrt{(R^2+a^2-2aR\mu)}} = \sum_0^N (2n+1)C_n(a)P_n^*(\mu), \qquad -1 \leqslant \mu \leqslant 0, \tag{3.7}$$

where the coefficients $C_n(a)$ are obtained from

$$C_n(a) = \int_{-1}^0 P_n^*(\mu)d\mu \int_0^\infty \frac{e^{-R}dR}{\sqrt{(R^2+a^2-2aR\mu)}}. \tag{3.8}$$

These integrals were evaluated using high order Gauss–Legendre quadrature for the μ integration and high order Gauss–Laguerre quadrature for the R integration. The computations were done on the Chalk River Datatron and results were obtained for various values of a. The rapid convergence of the expansion (3.7) which occurred for all cases considered is illustrated by the results shown in Table II for $a = 1.0$.

TABLE II

Coefficients $C_n(a)$ for $a = 1.0$

n	0	1	2
$C_n(1)$	6.64432×10^{-1}	2.58298×10^{-2}	2.16066×10^{-4}
n	3	4	5
$C_n(1)$	2.31098×10^{-4}	2.76412×10^{-5}	3.55770×10^{-6}

Let us now consider the Fourier transformed form of equation (3.3), with

$$\phi(\mathbf{k},\boldsymbol{\Omega}) = \int e^{i\mathbf{k}\cdot\mathbf{r}}\psi(\mathbf{r}\cdot\boldsymbol{\Omega})dV_r \tag{3.9}$$

where the integral is over r space. By multiplying equation (3.3) by $e^{i\mathbf{k}\cdot\mathbf{r}}$ and integrating over r, we obtain

$$(1-i\boldsymbol{\Omega}\cdot\mathbf{k})\phi(\mathbf{k},\boldsymbol{\Omega}) = \frac{c}{4\pi}\int \phi(\mathbf{k},\boldsymbol{\Omega}')d\Omega' - \int \boldsymbol{\Omega}\cdot d\mathbf{S}e^{i\mathbf{k}\cdot\mathbf{r}}\psi(\mathbf{r},\boldsymbol{\Omega})\Big|_{r=a} \tag{3.10}$$

where the last term, obtained by Gauss' theorem, is a surface integral over the sphere surface. $\boldsymbol{\Omega}\cdot d\mathbf{S} = a^2(\boldsymbol{\Omega}\cdot\mathbf{r}/r)d\Omega_r$.

Since $\psi(\mathbf{r},\boldsymbol{\Omega})$ is a function only of r and $(\boldsymbol{\Omega}\cdot\mathbf{r}/r)$, $\phi(\mathbf{k},\boldsymbol{\Omega})$ is a function only of k and $(\boldsymbol{\Omega}\cdot\mathbf{k}/k)$, where k is the magnitude of the vector $\mathbf{k}$.

Calling the last integral on the right-hand side of equation (3.10), $X(\mathbf{k},\boldsymbol{\Omega}) = X(k,\mu_0)$, where $\mu_0 = \boldsymbol{\Omega}\cdot\mathbf{k}/k$, we obtain, by dividing through by $(1-i\,\boldsymbol{\Omega}\cdot\mathbf{k})$ in equation (3.10) and integrating over Ω,

$$\phi_0(k)\left\{1-\frac{c}{k}\tan^{-1}k\right\} = \int_{-1}^{1}\frac{X(k,\mu_0)d\mu_0}{(1-i\mu_0 k)}. \tag{3.11}$$

This equation for the Fourier transform of the flux, $\rho(r)$, is similar to equation (2.4), which represents the Fourier transform of the flux in the case of plane symmetry. However, there is one important difference, which is that, for the plane case, $S(\mu)$ in equation (2.4) is obtained directly from the plane surface distributions, whereas $X(k,\kappa_0)$ is obtained from an integral of the surface distribution, taken over the surface of the sphere.

If we represent the integral on the right-hand side of equation (3.11) by $Y(k)$ we obtain for the flux $\rho(r)$

$$\rho(r) = \frac{1}{(2\pi)^3}\int\frac{Y(k)e^{-i\mathbf{k}\cdot\mathbf{r}}dV_k}{1-(c/k)\tan^{-1}k} \tag{3.12}$$

where dV_k is the three-dimensional volume element in k space.

Since $Y(k)$ does not depend on angle and is an even function of k, we obtain

$$\rho(r) = \frac{1}{4\pi^2 ir}\int_{-\infty}^{\infty} \frac{kY(k)\sin(kr)dk}{1-(c/k)\tan^{-1}k}. \tag{3.13}$$

This integral is similar in form to that obtained from equation (2.4) and again the type of contour used in Fig. 1, with poles at $k = \pm i\kappa_0$ and branch cuts from $k = i$ to $i\infty$ and $k = -i$ to $-i\infty$, will be used in evaluation of equation (3.13). The contour will be taken either in the upper half plane or lower half plane as is necessary to ensure convergence of the integrals. The case $c < 1$ will be considered here and the case $c = 1$, when $\kappa_0 = 0$, will be considered to be the results of taking the limit as c approaches unity. The case of $c > 1$ is also considered in CHP.

By the procedure which has led up to equation (3.13) we have replaced our two-medium problem by an infinite medium problem with a surface shell source at $r = a$. However, the solution to our problem still appears naturally in two parts; that is the solution for $r < a$ and that for $r > a$.

If we had the exact angular distribution on the surface of our sphere, we would have from equation (3.13) only a solution regular at the origin of the infinite medium source-free equation for $r < a$ (CHP, Section 17). This solution would be of the form

$$\phi_{as}(r) = A[\sinh(\kappa_0 r)/\kappa_0 r].$$

That is, the transient* part of our solution should vanish for $r < a$, and in order to satisfy the condition that the asymptotic solution should vanish for $r < a$, we must subtract off an amount of the solution of the infinite medium source-free equation to cancel $\phi_{as}(r)$. A will be determined by

$$A = \phi_{as}(r)\,|_{r=0}. \tag{3.14}$$

For our approximate calculations we will not have the exact surface distributions and consequently the solution evaluated for $r < a$, from equation (3.17) will have a small proportion of transient term mixed in. This will only be important for a sphere of small radius. However, this will mean that our solution for $r < a$ will not vanish completely inside the sphere. We can, however, subtract enough of the source-free solution to make our solution vanish at one point, the point $r = 0$ being the obvious choice. In other words we subtract off an amount of the source-free infinite medium solution, regular at the origin, given by $A[\sinh(\kappa_0 r)/\kappa_0 r]$ where A will be determined from

$$A = \rho(r)\,|_{r=0} \tag{3.15}$$

where $\rho(r)$ is given by equation (3.13).

In practice we need not go through the contour integration just described, but we can make use of the results already given for a point source by CHP.

*Strictly speaking in the case of a finite region (such as the interior of a sphere) the separation of $\rho(r)$ into $\rho_{as}(r)$ and $\rho_{non\text{-}as}(r)$ is not unambiguous. However, since $(\nabla^2+\kappa_0^2)\rho_{as}(r) = 0$, the statement in the text should be understood in the sense that if we knew the source distribution exactly, then for $r < a$ we would have $(\nabla^2+\kappa_0^2)\rho(r) = 0$.

This is done as follows. We rewrite equation (3.12) as

$$\rho(r) = \frac{1}{(2\pi)^3}\int\left\{1+\frac{(c/k)\tan^{-1}k}{1-(c/k)\tan^{-1}k}\right\}e^{-i\mathbf{k}\cdot\mathbf{r}}Y(k)dV_k. \tag{3.16}$$

Now the first term simply represents the direct unscattered contribution to the neutron flux from our surface source distribution. Also,

$$\frac{(c/k)\tan^{-1}k}{1-(c/k)\tan^{-1}k}$$

is proportional to the Fourier transform of the isotropic point source solution (CHP, Section 14). This means that we can invoke the convolution theorem for Fourier transforms and write the flux in the following form

$$\rho(r) = Z(r)+c\int\rho_0(|\mathbf{r}'-\mathbf{r}|)\,Z(r')\,dV_{r'}, \tag{3.17}$$

where $Z(r)$ is the direct unscattered contribution from the surface source and $\rho_0(r)$ is the point source solution,

$$\rho_0(r) = \frac{1}{4\pi r}\left\{-\frac{\partial\kappa_0^2}{\partial c}e^{-\kappa_0 r}+\int_0^1 g(c,\mu)e^{-r/\mu}\frac{d\mu}{\mu^2}\right. . \tag{3.18}$$

$Z(r)$ is readily calculated for a specific surface distribution $\psi(\mathbf{r}',\boldsymbol{\Omega})|_{r'=a}$, as follows, using Fig. 2,

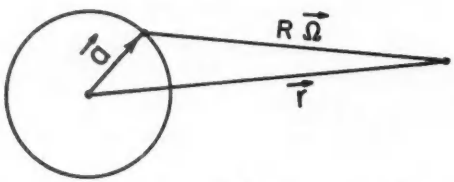

FIG. 2. The determination of the unscattered neutron density at $\mathbf{r}$ from a surface source on $r = a$.

$$f(\mathbf{r},\boldsymbol{\Omega}) = e^{-R}\psi(\mathbf{r}',\boldsymbol{\Omega})\,|_{r'=a} \tag{3.19}$$

where $f(\mathbf{r},\boldsymbol{\Omega})$ is the angular distribution at $\mathbf{r}$ due to the surface distribution at $r = a$. Then

$$Z(r) = \frac{1}{2\pi}\int f(\mathbf{r},\boldsymbol{\Omega})d\Omega = \int f(\mathbf{r},\boldsymbol{\Omega})d\mu_r \tag{3.20}$$

where $\mu_r = \boldsymbol{\Omega}.\mathbf{r}/r$. Thus

$$Z(r) = \int_{-1<\mu_a<0}\psi(a,\mu_a)e^{-R}d\mu_r \tag{3.21}$$

where $\mu_a = \boldsymbol{\Omega}\,.\,\mathbf{a}/a$ and $\psi(a,\mu_a)$ is the surface distribution.
Since

$$a^2 = r^2+R^2-2Rr\mu_r$$

and

$$r^2 = a^2+R^2+2Ra\mu_a$$

we can rewrite equation (3.21), taking R as the variable of integration, as

$$Z(r) = \frac{1}{2r}\int_{\substack{\sqrt{(r^2-a^2)},\ \text{if } r>a \\ a-r,\ \text{if } r<a}}^{r+a} e^{-R}\psi\left(a,\frac{r^2-a^2-R^2}{2Ra}\right)\left[1-\frac{r^2-a^2}{R^2}\right]dR. \tag{3.22}$$

Since we have obtained expansions in orthogonal polynomials for $\psi(a,\mu_a)$ for various values of the sphere radius, it suffices to calculate

$$Z_n(r) = \frac{1}{2r}\int_{\substack{\sqrt{(r^2-a^2)},\ \text{if } r>a \\ a-r,\ \text{if } r<a}}^{r+a} e^{-R}\left[\frac{r^2-a^2-R^2}{2Ra}\right]^n\left[1-\frac{r^2-a^2}{R^2}\right]dR \tag{3.23}$$

corresponding to the various powers of μ_a^n in $\psi(a,\mu_a)$. These components of $Z(r)$ can then be combined according to the coefficients of μ_a^n in the expansion (3.7) to give the final approximation to $Z(r)$.

For example, we obtain

$$Z_0(r) = \frac{1}{2r}\left\{e^{-\sqrt{(r^2-a^2)}}-e^{-(r+a)}-(r^2-a^2)\left[\frac{E_2[\sqrt{(r^2-a^2)}]}{\sqrt{(r^2-a^2)}}-\frac{E_2(r+a)}{(r+a)}\right]\right\}, \quad r>a \tag{3.24}$$

$$= \frac{1}{2r}\left\{e^{-(a-r)}-e^{-(r+a)}-(r^2-a^2)\left[\frac{E_2(a-r)}{a-r}-\frac{E_2(r+a)}{r+a}\right]\right\}, \quad r<a.$$

The other $Z_n(r)$ used in our calculations are listed in Appendix I. In the above formulae $E_n(x)$ is one of the functions $E_n(x)$ defined by

$$E_n(x) = \int_1^\infty e^{-xu}u^{-n}du. \tag{3.25}$$

Some properties of these functions and tables for various n are given in CHP, Appendix A.

Since $\rho_0(r)$ as given by equation (3.18) is not known as a simple analytic expression, and since $Z(r)$ is spherically symmetric, the integration in equation (3.17) involves a double numerical integration for each $Z_n(r)$. This can be reduced to a single integration if a suitable accurate expression for $\rho_0(r)$ can be found. Such an expression is derived in Appendix II.

All that remains now, for any particular problem is to evaluate (3.17), and then determine the amount of source-free solution to be subtracted, using (3.15).

The asymptotic solution from (3.17) for $r>a$ will have the form

$$\rho_{\text{as. outside}}(r) = B\frac{e^{-\kappa_0 r}}{r} \tag{3.26}$$

and subtracting off the amount of $\sinh(\kappa_0 r)/\kappa_0 r$ given by (3.15) the final asymptotic solution will be

$$\rho_{as}(r) = B\frac{e^{-\kappa_0 r}}{r}-A\frac{\sinh(\kappa_0 r)}{\kappa_0 r} \tag{3.27}$$

and in the limit as c approaches unity, with κ_0 approaching zero

$$\rho_{as}(r) = \frac{B}{r} - A$$

whence

$$\lambda = \frac{A}{B}a^2 - a. \tag{3.28}$$

A is readily obtained from (3.15) and (3.17) as

$$A = Z(0) + 4\pi c \int_0^\infty \rho_0(r')Z(r')r'^2 dr'. \tag{3.29}$$

B can be obtained from (3.17) by noting that in the integral only the term of the form

$$e^{-\kappa_0|\mathbf{r}-\mathbf{r}'|}/|\mathbf{r}-\mathbf{r}'|$$

will contribute to B and this term can be expanded as

$$\frac{e^{-\kappa_0|\mathbf{r}-\mathbf{r}'|}}{|\mathbf{r}-\mathbf{r}'|} = \frac{\sinh(\kappa_0 r')}{\kappa_0 r'}\frac{e^{-\kappa_0 r}}{r} + \left\{\begin{array}{l}\text{terms decreasing faster} \\ \text{than } \dfrac{e^{-\kappa_0 r}}{r} \text{ for } r \to \infty.\end{array}\right\}. \tag{3.30}$$

The terms decreasing faster than $e^{-\kappa_0 r}/r$ do not contribute to the value of B, whence, since $Z(r)$ is of order e^{-r} also, we obtain

$$B = \frac{-c\partial\kappa_0^2}{\partial c}\int_0^\infty \frac{\sinh(\kappa_0 r')}{(\kappa_0 r')}Z(r')r'^2 dr', \tag{3.31}$$

which can easily be expressed in terms of the Fourier transform of $Z(r)$ (with κ_0 replaced by $-ik$), which in turn is simply related to $Y(k)$.

We obtain finally

$$B = \frac{-ca^2}{2}\frac{\partial\kappa_0^2}{\partial c}\int_{-1}^{0}\mu\psi(a,\mu)d\mu\int_{-1}^{1}\frac{e^{-\kappa_0 a\mu_0}d\mu_0}{\sqrt{[1+2\kappa_0\mu\mu_0-\kappa_0^2(1-\mu^2-\mu_0^2)]}}. \tag{3.32}$$

For $c = 1$, $\kappa_0 = 0$,

$$B = -3a^2\int_{-1}^{0}\mu\psi(a,\mu)d\mu. \tag{3.33}$$

Having now obtained the expression for A and B it remains only to consider the various values of a for which λ is desired and to use the iterated angular distributions from (3.5) and (3.7) in the computation.

We will consider the limiting cases of small a and large a first of all since it is only in these cases that accurate results are known for λ (Davison and Kushneriuk 1946; Davison 1951). These results are:

$$\begin{array}{ll}\text{for large } a, & \lambda = .7104 + 0(1/a), \\ \text{for small } a, & \lambda = 4/3 + 0(a).\end{array} \tag{3.34}$$

For large a, the spherical surface of the sphere approaches a plane surface

and we return to the Milne problem, which has already been solved by the iterative method proposed (Conkie 1959), the result being

$$\lambda = .7113+0(1/a).$$

For small a, we have the simple result that

$$\psi(a,\mu) = \frac{q_0}{a^2}+\left\{\text{terms of order } \frac{1}{a}\right\},$$

and to this order is independent of angle. Thus

$$B = 3\frac{q_0}{2}+0(a). \tag{3.35}$$

Also for the interior of a small sphere, the probability of a collision is small, and consequently the first term in the expression (3.17) for $\rho(r)$ dominates inside the sphere. This means, since it is $\rho(0)$ which determines A, that only the $Z(0)$ terms in equation (3.29) are important for small a, the scattered terms being of order a relative to the unscattered terms. In particular we need $Z_0(0)$ for small a.

This is easily calculated from equation (3.24) from the formula for $r<a$, and gives

$$Z_0(0) = 2+0(a)$$

and then

$$A = 2q_0/a^2. \tag{3.36}$$

Substituting (3.35) and (3.36) into (3.28), we get, for small a

$$\lambda = 4/3+0(a).$$

Combining our iterative results for large a and small a, we have then

$$\begin{aligned} &\text{for large } a, && \lambda = .7113+0(1/a), \\ &\text{for small } a, && \lambda = 4/3+0(a). \end{aligned} \tag{3.37}$$

Comparing these results with (3.34), we see that for large a we have an error of about 0.1% and for small a we obtain the exact result. These results might lead us to hope that for intermediate a, high accuracy can be attained by this method. Unfortunately there are no very accurate results for intermediate a with which comparisons can be made. There do exist some approximate results obtained from various methods and these will be discussed in the next section.

4. COMPARISONS WITH THE RESULTS OF OTHER METHODS

We will consider the results of two other workers for the black sphere problem, and we will use their results for comparison with the results of our iterative method. Among the results we will consider are those of Davison and Kushneriuk (1946), who used a combination of spherical harmonics

calculations and perturbation calculations to estimate the graphical form of the dependence of λ on a. We will also consider the variational results of Marshak (1947), who used a stationary expression for λ. However, Marshak's results were calculated using a rather crude trial function and we will not lay much stress on this comparison. Indeed, it would be desirable to repeat Marshak's calculation, using a better trial function before going into any detailed comparisons with his variational results.

The improved angular distribution was expanded in shifted Legendre polynomials as in equation (3.7) and terms up to and including $P_3^*(\mu)$ were used in most of the calculations. Estimates of the effect of retaining higher order terms will be given later. The integration in (3.29) was done by Simpson's rule with an interval of $\Delta r' = .02$ for a range of values of a. (The integration was stopped at values of r', where only further contributions of order 10^{-6} were being made.) The integration was repeated with $\Delta r' = .035$ for $a = 1.0$ in order to assess the truncation errors due to the quadrature formula used. This comparison will be given below as well.

The results obtained are given in Table III and the corresponding values from Davison and Kushneriuk's estimated curve are given for comparison.

TABLE III

Values of λ as a function of sphere radius

a	Davison's value of λ	Iterative value of λ
0	4/3	4/3
.2	1.256	1.2557
.4	1.195	1.1757
.6	1.145	1.1339
.8	1.100	1.0761
1.0	1.060	1.0535
1.5	.988	.9876

Davison and Kushneriuk's curve and a curve drawn from the iterative results are shown in Fig. 3. The curves differ by less than 2% from $a = 0.4$ to $a = 0.8$, by about 1% at $a = 1.0$, and are very close at $a = 1.5$. The precise numerical value obtained from the estimated curve cannot of course be taken very seriously, but the results seem to show that the estimated curve follows quite well the accurate form of the curve for λ as a function of a, the greatest errors being in the neighborhood of $a = 0.7$–0.8.

Marshak's variational value is $\lambda = 1.024$ for $a = 1.0$, which is about 3% below the iterative value. Presumably this value would be improved considerably if a more accurate trial function were used. It should be noted that owing to the form of variational principle used, Marshak's approximate value should indeed lie below the accurate value.

As a check on the internal consistency of the calculation, further calculations were carried out retaining only up to $P_2^*(\mu)$ and $P_4^*(\mu)$ terms in the expansion (3.7) for $a = 1.0$. The results obtained for $Z(0)$ for both of these distributions and for the $P_3^*(\mu)$ distributions are given in Table IV.

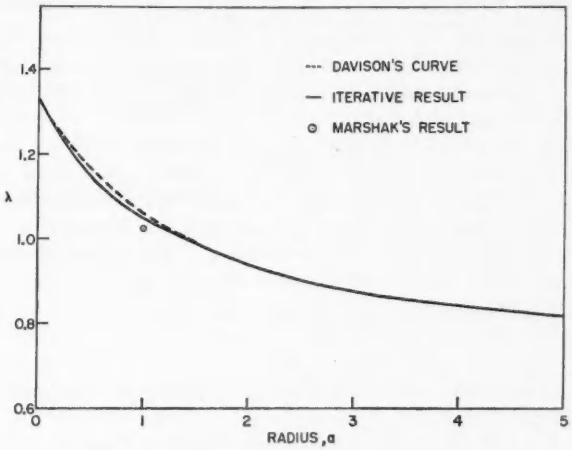

FIG. 3. A comparison of the linear extrapolation length λ, calculated by the iterative method, with other estimates of λ.

TABLE IV

Values of $Z(0)$ for various angular expansions. $a = 1.0$

Order of expansion	$Z(0)$
$P_3^*(\mu)$	.72076
$P_3^*(\mu)$	.72194
$P_4^*(\mu)$	.72177

We see that there is a very small difference between the P_3^* and P_4^* results, this difference being about .02%. Thus we can take the P_3^* results for $Z(r)$ to be accurate enough for most purposes, assuming that the accuracy in $Z(0)$ is an indication of the accuracy in $Z(r)$. Any other quantity which we may wish is obtained from the second term on the right of equation (3.17), which involves an integration over the function $Z(r)$, which should have an oscillatory error due to the orthogonal function expansion used. These other quantities should then be even more accurate than $Z(r)$.

For example, for the $P_2^*(\mu)$ distribution we obtain $\lambda = 1.0514$, which differs by only 0.2% from the $P_3^*(\mu)$ value, $\lambda = 1.0535$.

By changing the interval in the Simpson's rule integration from $\Delta r = .02$ to $\Delta r = .035$, we obtain from the $P_3^*(\mu)$ distribution, $\lambda = 1.0442$, which differs by about 1% from the presumably more accurate value.

Considering all these factors, and the fact that we have used an approximation to $\rho_0(r)$, our iterative results should be accurate to better than 1%, the errors lying mostly in the numerical approximations made in evaluating the various integrals involved.

5. EXTENSION TO GENERAL PROBLEMS WITH SPHERICAL SYMMETRY

Having discussed the particular problem of the black sphere in Section 3 in some detail, we can easily determine how a general multilayer problem should be tackled. The iterative procedure follows through the first two steps and we obtain the iterated angular distribution at the surfaces $r = r_i$ from equation (3.4). It should be noted here that although in most problems the angular distribution will not vanish over part of its range, as it does vanish for $\Omega \cdot \mathbf{r}/r > 0$ for the black sphere problem, it is still best to expand the distribution in two sets of shifted Legendre polynomials, one adjusted to the range $-1 \leqslant \mu \leqslant 0$ and the other to the range $0 \leqslant \mu \leqslant 1$. Then the coefficients in the angular expansion for $\mu \geqslant 0$ are obtained by inserting the density and value of c for $r_{i-1} < r < r_i$ in equation (3.4) *et seq.* and the coefficients for $\mu \leqslant 0$ are obtained by inserting the values of density and c for $r_i < r < r_{i+1}$ in equation (3.4) *et seq.* This takes into account the boundary conditions that at the surface $r = r_i$, neutrons with $\mu > 0$ have come from $r < r_i$ and neutrons with $\mu < 0$ have come from $r > r_i$.

Now we go on to step 3 of our iterative procedure. For $r_i \leqslant r \leqslant r_{i+1}$ only the surface sources at $r = r_i$ and $r = r_{i+1}$ contribute to the density. The complete solution in this region is then obtained as a superposition of the contribution from each surface, and the amount of source-free solution which is added in is determined as before by $\rho(r = 0) = 0$ and $\rho(r \gg r_{i+1}) = 0$, where $\rho(r)$ is determined from the surface sources at $r = r_i$ and $r = r_{i+1}$.

Going on in this way determining the contribution from the boundary surfaces of each region we can determine the iterated density for that region in the form of equation (3.17), whence one numerical integration will give us the explicit values for the density in the region being considered.

6. CONCLUSION

We see then, that our iterative method can readily be extended to problems with spherical symmetry. The calculations required are considerably more complicated than the original spherical harmonics calculations or even than the iterative calculations for problems with plane symmetry. For a preliminary design calculation on a spherical system the amount of computation and analysis required is probably prohibitive, and a P_3 or P_5 calculation will prove less troublesome. On the other hand for such a problem where the usual spherical harmonics method converges slowly or where more accurate results are required, the more elaborate scheme proposed here seems capable of giving results of extremely good accuracy.

ACKNOWLEDGMENTS

I would like to thank Dr. B. Davison for many helpful discussions.

REFERENCES

CASE, K. M., DE HOFFMAN, F., and PLACZEK, G. 1953. Introduction to the Theory of Neutron Diffusion. U.S. Government Printing Office.
CONKIE, W. R. 1959. Nuclear Sci. and Eng. **6**, 267.
——— 1960*a*. Nuclear Sci. and Eng. **7**, 295.
——— 1960*b*. Trans. Am. Nuclear Soc. **3** (1), 267.
DAVISON, B. 1951. Proc. Phys. Soc. **64**, 881.
——— 1957. Neutron transport theory (Oxford University Press).

DAVISON, B. and KUSHNERIUK, S. 1946. M.T. 214.
GREULING, E., CLARK, F., and GOERTEZEL, G. 1953. NDA 10–96.
KOURGANOFF, V. 1952. Basic methods in transport problems (Oxford University Press).
LANCZOS, C. 1956. Applied analysis (Prentice Hall).
MARK, C. 1957. Chalk River Reports CRT-338 and CRT-340 (revised).
MARSHAK, R. E. 1947. Phys. Rev. **71**, 688.
WEINBERG, A. M. and WIGNER, E. P. 1958. The physical theory of neutron chain reactors (University of Chicago Press).

APPENDIX I

The $Z_n(r)$ used in the calculations are:

$$Z_0(r) = \frac{1}{2r}\left\{e^{-(a-r)} - e^{-(r+a)} - (r^2-a^2)\left[\frac{E_2(a-r)}{a-r} - \frac{E_2(r+a)}{(r+a)}\right]\right\}, \qquad r < a,$$

$$= \frac{1}{2r}\left\{e^{-\sqrt{(r^2-a^2)}} - e^{-(r+a)} - (r^2-a^2)\left[\frac{E_2[\sqrt{(r^2-a^2)}]}{\sqrt{(r^2-a^2)}} - \frac{E_2(r+a)}{r+a}\right]\right\}, \qquad r > a.$$

$$Z_1(r) = \frac{1}{4ra}\left\{2(r^2-a^2)[E_1(a-r) - E_1(r+a)] + e^{-(r+a)}(r+a+1)\right.$$

$$\left. - e^{-(a-r)}(a-r+1) - (r^2-a^2)\left[\frac{E_3(a-r)}{(a-r)^2} - \frac{E_3(r+a)}{(r+a)^2}\right]\right\}, \qquad r < a,$$

$$= \frac{1}{4ra}\left\{2(r^2-a^2)[E_1[\sqrt{(r^2-a^2)}] - E_1(r+a)] + e^{-(r+a)}(r+a+1)\right.$$

$$\left. - e^{-\sqrt{(r^2-a^2)}}(\sqrt{r^2-a^2}+1) - (r^2-a^2)^2\left[\frac{E_3[\sqrt{(r^2-a^2)}]}{(r^2-a^2)} - \frac{E_3(r+a)}{(r+a)^2}\right]\right\}, \qquad r > a.$$

$$Z_2(r) = \frac{1}{8a^2r}\left\{3(r^2-a^2)^2\left[\frac{E_2(a-r)}{a-r} - \frac{E_2(r+a)}{(r+a)}\right] - 3(r^2-a^2)[e^{-(a-r)} - e^{-(r+a)}]\right.$$

$$+ e^{-(a-r)}[(a-r)^2 + 2(a-r) + 2] - e^{-(r+a)}[(r+a)^2 + 2(r+a) + 2]$$

$$\left. - (r^2-a^2)^3\left[\frac{E_4(a-r)}{(a-r)^3} - \frac{E_4(a+r)}{(a+r)^3}\right]\right\}, \qquad r < a,$$

$$= \frac{1}{8a^2r}\left\{3(r^2-a^2)^2\left[\frac{E_2[\sqrt{(r^2-a^2)}]}{\sqrt{(r^2-a^2)}} - \frac{E_2(r+a)}{r+a}\right] - 3(r^2-a^2)[e^{-\sqrt{(r^2-a^2)}} - e^{-(r+a)}]\right.$$

$$+ e^{-\sqrt{(r^2-a^2)}}[(r^2-a^2) + 2\sqrt{(r^2-a^2)} + 2] - e^{-(r+a)}[(r+a)^2 + 2(r+a) + 2]$$

$$\left. - (r^2-a^2)^3\left[\frac{E_4[\sqrt{(r^2-a^2)}]}{(r^2-a^2)^{3/2}} - \frac{E_4(a+r)}{(a+r)^3}\right]\right\}, \qquad r > a.$$

$$Z_3(r) = \frac{1}{16a^3r}\left\{4(r^2-a^2)^3\left[\frac{E_3(a-r)}{(a-r)^2} - \frac{E_3(r+a)}{(r+a)^2}\right]\right.$$

$$- 6(r^2-a^2)^2[E_1(a-r) - E_1(r+a)] + 4(r^2-a^2)[e^{-(a-r)}(a-r+1)$$

$$- e^{-(r+a)}(r+a+1)] - e^{-(a-r)}[(a-r)^3 + 3(a-r)^2 + 6(a-r) + 6]$$

$$+ e^{-(r+a)}[(a+r)^3 + 3(a+r)^2 + 6(a+r) + 6]$$

$$\left. - (r^2-a^2)^4\left[\frac{E_5(a-r)}{(a-r)^4} - \frac{E_5(r+a)}{(r+a)^4}\right]\right\}, \qquad r < a,$$

$$= \frac{1}{16a^3r}\Bigg\{4(r^2-a^2)^3\left[\frac{E_3[\sqrt{(r^2-a^2)}]}{(r^2-a^2)}-\frac{E_3(r+a)}{(r+a)^2}\right]$$

$$-6(r^2-a^2)^2[E_1[\sqrt{(r^2-a^2)}]-E_1(r+a)]+4(r^2-a^2)[e^{-\sqrt{(r^2-a^2)}}[\sqrt{(r^2-a^2)}+1]$$

$$-e^{-(r+a)}(r+a+1)]-e^{-\sqrt{(r^2-a^2)}}[(r^2-a^2)^{3/2}+3(r^2-a^2)+6\sqrt{(r^2-a^2)}+6]$$

$$+e^{-(r+a)}[(a+r)^3+3(a+r)^2+6(a+r)+6]$$

$$-(r^2-a^2)^4\left[\frac{E_5[\sqrt{(r^2-a^2)}]}{(r^2-a^2)^2}-\frac{E_5(r+a)}{(r+a)^4}\right]\Bigg\}, \qquad r > a.$$

APPENDIX II

An Analytical Expression for the Point Source Solution

We wish to obtain a simple, accurate expression for

$$\rho_1(r) = \frac{1}{4\pi r}\int_0^1 g(c,\mu)e^{-\tau/\mu}\frac{d\mu}{\mu^2} \tag{II.1}$$

where

$$g(c,\mu) = \frac{1}{(1-c\mu\tanh^{-1}\mu)^2+[(\pi/2)c\mu]^2}$$

(CHP, Section 14). Since $g(c,\mu)$ is a function of μ^2 only, we will try and find an expansion of $g(c,\mu)$ in the orthogonal polynomials $p_n(\mu^2)$, such that

$$\int_0^1 p_n(\mu^2)p_m(\mu^2)d\mu = N_m\delta_{nm} \tag{II.2}$$

where δ_{nm} is the Kronecker delta.

The three term recurrence relationship between these polynomials is easily determined to be

$$p_{n+1}(x) = xp_n(x)-\left[\frac{8n^2}{16n^2-1}-\frac{1}{(16n^2-1)(4n+3)}\right]p_n(x) \tag{II.3}$$

$$-\frac{(2n)^2(2n-1)^2}{(4n-3)(4n-1)^2(4n+1)}p_{n-1}(x).$$

The first few polynomials are

$$p_0(\mu^2) = 1, \qquad N_0 = 1$$

$$p_1(\mu^2) = \mu^2-\frac{1}{3}, \qquad N_1 = \frac{4}{45}$$

$$p_2(\mu^2) = \mu^4-\frac{6}{7}\mu^2+\frac{3}{35}, \qquad N_2 = \frac{8^2}{5^2\cdot 7^2\cdot 3^2}.$$

$$p_3(\mu^2) = \mu^6-\frac{15}{11}\mu^4+\frac{5}{11}\mu^2-\frac{5}{11\cdot 21}, \qquad N_3 = \frac{4^4}{3^2\cdot 7^2\cdot 11^2\cdot 13}.$$

Expanding

$$g(c,\mu) = \sum_{n=0}^{N} A_n p_n(\mu^2) \tag{II.4}$$

we obtain

$$A_m = \frac{1}{N_m}\int_0^1 p_m(\mu^2) g(c,\mu)\, d\mu. \tag{II.5}$$

The moments $\langle \mu^{2n} \rangle$ of $g(c,\mu)$ are given in CHP (p. 78 *et seq.*) for various values of c.

Let us consider $c = 1.0$ and $N = 2$ in the expansion (II.4). Then we obtain

$$\begin{aligned} g(c,\mu) &= .8 - .6859\, p_1(\mu^2) - .4484\, p_2(\mu^2) \\ &= .9902 - .3016\, \mu^2 - .4484\, \mu^4. \end{aligned}$$

Inserting this into equation (II.1), we obtain

$$\rho_1(r) = \frac{1}{4\pi r}\left\{ .9902\frac{e^{-r}}{r} - .3016 E_2(r) - .4484 E_4(r) \right\} \tag{II.6}$$

where the $E_n(x)$ are the same functions referred to in Section 3.

Comparing this with the tabulated values given by CHP, we obtain the results given in Table V for $\epsilon(r) = 4\pi r^2 e^r \rho_1(r)$.

TABLE V

Comparison of $N = 2$ approximation with exact results.
$c = 1.0$

r	ϵ exact	ϵ approximate	% error
0	1.0000	.9902	−1
.5	.8460	.8479	+.2
1.0	.7612	.7635	+.3
2.0	.6568	.6571	Very small

We see that the error in $\epsilon(r)$ is greatest at $r = 0$, and drops off fairly quickly, being oscillatory in sign. This latter is a useful property since it will mean some cancellation of errors in integrals involving our approximate function. The agreement between the two sets of results is good considering the rather low order of approximation.

It was felt that the $N = 3$ approximation would be good enough for the calculations done on the black sphere, and the results for this case are as follows.

$$g(c,\mu) = 1.0055 - .6220\, \mu^2 + .5130\, \mu^4 - .7050\, \mu^6$$

and

$$\rho_1(r) = \frac{1}{4\pi r}\left\{ 1.0055\frac{e^{-r}}{r} - .6220 E_2(r) + .5130 E_4(r) - .7050 E_6(r) \right\}. \tag{II.7}$$

Table VI shows the comparison between the $\epsilon(r)$.

TABLE VI

Comparison of $N = 3$ approximation with exact results.
$c = 1.0$

r	ϵ exact	ϵ approximate	% error
0	1.0000	1.0055	+.5
.5	.8460	.8450	−.1
1.0	.7612	.7604	−.1
2.0	.6568	.6570	Very small

The results show that this approximation should be accurate enough for most practical purposes although it should be noted that it is very easy to increase the order of approximation in the expansion of $g(c,\mu)$.

Although not used in our calculations, the results of such an expansion for $c = 0.5$ may also be of interest, and will indicate the usefulness of this expansion for other values of c.

We obtain, for the $N = 2$ approximation,

$$\rho_1(r) = \frac{1}{4\pi r}\left\{.9866\frac{e^{-r}}{r} + .5224E_2(r) + .2048E_4(r)\right\}. \tag{II.8}$$

Table VII shows the comparison with exact results.

TABLE VII

Comparison of $N = 2$ approximation with exact results.
$c = 0.5$

r	ϵ exact	ϵ approximate	% error
0	1.0000	.9866	−1.4
.5	1.1529	1.1551	+ .2
1.0	1.2412	1.2454	+ .2
2.0	1.3504	1.3521	+ .1

Again the error is oscillatory and largest near $r = 0$. A low order approximation should be adequate for calculations with this value of c, and, the indications are, for all values of c of physical interest.

ON THE PRODUCTION OF Be^{7}, Mg^{28}, AND Ni^{66} IN THE SLOW NEUTRON FISSION OF U^{235} [1]

J. C. Roy

ABSTRACT

The yields of 53-day Be^{7}, 21.3-hour Mg^{28}, and 56.6-hour Ni^{66} from the slow neutron fission of U^{235} have been investigated. Upper limits of $3\times10^{-7}\%$ and $4.2\times10^{-9}\%$ have been set for the fission yields of Be^{7} and Mg^{28} respectively. A fission yield of $2.0\pm1.0\times10^{-8}\%$ has been found for the formation of Ni^{66}. These results are compared with the current knowledge of the frequency of triple fission of U^{235}.

INTRODUCTION

The possibility of slow neutron fission of U^{235} in three fragments has been studied by many investigators with a variety of techniques. From the findings of these studies, reviewed by Whitehouse (1952), Perfilov (1958), Demers (1958), and Hyde (1960), some features of the ternary fission of U^{235} by slow neutrons have been well established while others are not yet clarified.

One type of ternary fission, namely the emission of long range alpha particles in coincidence with two heavy fragments has been completely proved. The frequency of this process for slow neutron fission of U^{235} is one in 325 ± 100 binary events.

The emission of short range light particles associated with two heavy fragments is often described as another type of ternary fission. Cassels *et al.* (1947), Allen and Dewan (1951) working with counters, Green and Livesey (1947, 1948), and Titterton (1951*a*), working with nuclear emulsions have found that one slow neutron fission of U^{235} in about 100 resulted in the emission of short range particles with a charge of 1, 2, or slightly higher. Tsien and his collaborators (1947, 1947*b*) also observed short range particles of about the same abundance in nuclear emulsions, but they could not decide on the source. They may result from fission or they may be protons and other light particles recoiling from collisions between the nuclei in the emulsion and fission fragments. Marshall (1949), Demers (1953, 1958), and Perfilov (1958) support the latter view. deLaboulaye *et al.* (1953, 1954) using cloud chambers concluded that if the emission of short range light particles exists at all, its frequency is smaller than 1 ± 3 in 1000 binary events.

The possibility that some of these fragments are beryllium nuclei have been investigated by Cook (1952), who set an upper limit of $10^{-5}\%$ for the yield of Be^{7} and by Flynn *et al.* (1956), who set an upper limit of $4\times10^{-4}\%$ for the yield of Be^{10}. Titterton (1951*a*, *b*) from the examination of 250,000 fission tracks has observed no instance of Li^{7}, B^{8}, or Be^{8}. Recently Albenesius (1959) has reported evidence for the formation of tritium in the ratio of one to 10^{4}

[1]Manuscript received October 28, 1960.
Contribution from the Research Chemistry Branch, Atomic Energy of Canada Limited, Chalk River, Ontario.
Issued as A.E.C.L. No. 1164.

binary fissions. He interpreted the formation of tritium as due to ternary fission. From these studies one may conclude that the frequency of emission of a short range particle is not yet established, with the exception, perhaps, of tritium.

In the present work a further radiochemical search for Be^7 was made. Radiochemical investigations cannot show what type of fission produces Be^7 and therefore the discussion of possible mechanism will be postponed until the formation of Mg^{28} and Ni^{66} is discussed.

A third type of ternary fission, the splitting of U^{235} in three fragments of comparable mass, can be differentiated and is usually called tripartition. Theories of nuclear fission (Bohr and Wheeler 1939; Present and Knipp 1940; Present 1941) do not rule out tripartition but say little about the frequency of the process.

Tsien and his collaborators (1947, 1947*b*), Chastel and Vigneron (1949), Perfilov (1958), and Catala *et al.* (1959, 1960) have observed triple tracks in nuclear emulsions which they ascribed to tripartition. Using the same technique Demers (1946, 1947, 1953, and 1958), Green and Livesey (1947), Titterton (1951*a*), and Dutta (1953) upon examination of 1500, 25,000, 250,000, and 20,000 fission tracks respectively could not definitely assign any of the observed events to tripartition of U^{235}. Rosen and Hudson (1950), from a careful study of tripartition of U^{235} with triple ionization chambers, concluded that triple fissions occur to the extent of 6.7 ± 3.0 per 10^6 binary fissions.

In the wartime radiochemical research on fission, attempts were made to detect radioactive products in the mass range of 30 to 60 which could have been formed by tripartition, but the results were negative (Metcalf *et al.* 1951). Upper limits of about $10^{-4}-10^{-5}\%$ were set for the formation of such products. The findings of these studies on tripartition are collected in Table I.

The frequency of tripartition obtained by Perfilov and Tsien *et al.* seems to be too high in comparison with that obtained by the other investigators. The first group of workers may have mistaken for a tripartition a triple track due to a binary fission event plus a heavy recoil originating in the emulsion at approximately the point of fission (cf. Demers 1958 for a discussion of the question). Actually Dutta (1953) observed one tripartition, but he ascribed it to the interaction of a fast neutron of cosmic origin. Demers (1958) does not exclude the possibility that the triple events observed by Rosen and Hudson (1958) could be due to collisions of binary fragments with C, N, or O atoms at the point of fission.

In summary, it appears from the work of Titterton, Catala *et al.*, and Rosen and Hudson that the frequency of tripartition is one or less per 2×10^5 binary fissions. Physical methods are able to detect single events whereas the yield of radioactive product represents a fraction only of the total tripartitions. If one assumes that radioactive products in Table I form about 1% of the total tripartition, an upper limit of about one per 10^4 binary events is obtained from the radiochemical studies.

Another type of fission which could produce the radioactive products investigated in our study is the quadripartition of U^{235} by thermal neutrons.

TABLE I

Summary of the findings on the tripartition of U^{235} by thermal neutrons

Authors	Particle masses M_1	M_2	M_3	Ratio = triple fission / binary fission
	(A) Photographic emulsions			
Perfilov (1958)	62	113	60	1/5000
	73	76	86	
Tsien *et al.* (1947, 1947*b*)	127	77	32	1/6000
Catala *et al.* (1959, 1960)	150	74	12	1/175,000
	169	55	11	
Demers (1958)	None in 1,500 b.f.			<1/1500
Green and Livesey (1947)	None in 25,000 b.f.			<1/25,000
Titterton (1951*a*)	None in 250,000 b.f.			<1/250,000
Dutta (1953)	None in 20,000 b.f.			<1/20,000
	(B) Ionization chambers			
Rosen and Hudson (1950)				$6.7/10^6$
	(C) Radiochemical studies			
Metcalf *et al.* (1951)				
	Nuclide	Yield		
	87-day S^{35}	$<1.8\times10^{-4}\%$		
	160-day Ca^{45}	$<1.4\times10^{-4}\%$		
	4.7-day Ca^{47}	$<10^{-5}\%$		
	Scandium isotopes	$<10^{-4}\%$		
	45-day Fe^{59}	$<4\times10^{-5}\%$		

Tsien and his collaborators (1947, 1947*a*, *b*, *c*; Ho *et al.* 1946; Chastel and Vigneron 1949) claimed to have observed cases of quadripartition with a frequency of one in 5000 binary fissions. However, Perfilov, who has observed similar cases, attributed them to elastic collisions of each fragment with nuclei of elements in the emulsion. Demers (1958) supports the latter view. This is also in agreement with the observations of Green and Livesey (1947), who found no quadripartition in 25,000 events, and of Titterton (1952), who saw only two tracks in 600,000 events which could be possibly classed as quadripartitions.

One may conclude from this review that additional evidence is required to establish with certainty the occurrence of tripartition and quadripartition and that the frequency of such events is low, in particular the yield of any product resulting from these processes is probably less than $10^{-5}\%$. For such a low yield a search for suitable radioactive products seems to be the best approach to explore anew tripartition or quadripartition of U^{235} by slow neutrons. Identification of a radionuclide which cannot be produced by reactions other than fission should provide evidence for the processes. Of course the formation of such a product by binary fission should also be ruled out. Three radionuclides, 53-day Be^7, 21.3-hour Mg^{28}, and 56.6-hour Ni^{66} are the best candidates for such an investigation. These three nuclides cover a wide range of mass; in a thermal neutron irradiation of uranium they can be formed only by fission, except for very rare processes like double neutron capture; they have suitable radioactive properties and they can be easily purified. The present paper reports the results of a search for these three radionuclides in the slow neutron irradiation of U^{235}.

EXPERIMENTAL

(a) Irradiation and Purification

One sample of natural uranium trioxide (~150 mg) and one sample of reactor grade uranium dioxide (~5 mg) enriched to 93% in U^{235} were used as starting materials. These were sealed in a quartz tube and irradiated in an iron capsule for 16.6 hours in an empty fuel rod position in the NRX reactor (Hurst 1955). The reactor neutron flux in the position used was about 7×10^{13} n/cm^2 sec; about 94% of the flux is thermal, 3% is in the resonance neutron region, and the other 3% are fast neutrons (Roy and Wuschke 1959). After the end of the irradiation, the iron capsule was taken out of the reactor by means of a pneumatic carrier and received and opened in a shielded cell where simple remote controlled operations could be done. The contents of the capsule were poured into a beaker containing known amounts of Be, Mg, Ni, and Ba carriers. The barium was extracted in order to determine the number of fissions. The irradiated uranium oxide was heated for about half an hour in concentrated HCl; this treatment dissolved about one-half of the oxide. The solution was transferred to another beaker, diluted with water, and the barium was precipitated as the sulphate. The $BaSO_4$ was filtered and then put aside for further purification. The filtrate was evaporated to a small volume, made 10 to 12 *N* in HCl, and passed through a Dowex-1 ion exchange column; this step eliminated the uranium and some fission products (Kraus and Nelson 1955). The eluate was evaporated to a small volume, neutralized with ammonium hydroxide, and beryllium hydroxide was precipitated by the addition of a few drops in excess. The hydroxide was filtered and kept for further purification. Sodium hydroxide was added to the filtrate and, on boiling, nickel and magnesium hydroxides precipitated. The precipitates were filtered. The hydroxides were dissolved in HCl and the solution was passed twice through Dowex-1 in 10 *N* and 1 *N* HCl respectively. Ferric hydroxide was precipitated in the solution several times and the nickel was separated from the magnesium by a dimethylglyoxime precipitation followed by a centrifugation. Complete purification of the nickel was achieved by the procedure described in Kleinberg (1958). Finally nickel was electroplated on a weighed platinum foil, weighed, placed on an aluminum tray, and its radioactivity determined with an anthracene beta counter described in the next section.

The magnesium fraction in the supernatant resulting from the dimethylglyoxime precipitation was boiled with sodium hydroxide. The magnesium hydroxide precipitate was dissolved in concentrated HNO_3 and two MnO_2 scavengings were done. The magnesium was precipitated as the ammonium phosphate by the method of Epperson (Treadwell and Hall 1945). The precipitate was dissolved in 1.5 *N* HCl and passed twice through Dowex-50 at a temperature of 50° C (Milton and Grummitt 1957). Finally the magnesium was precipitated as the ammonium phosphate, filtered on a "Millipore" filter paper, dried at 50° C, weighed, placed on an aluminum tray, and counted with the anthracene beta counter.

The purification of beryllium hydroxide obtained in the first stage of the

separation was done according to the method of Buchanan (1958). Finally the beryllium was transformed to BeO, deposited on an aluminum tray, weighed, and counted with the NaI(Tl) scintillation spectrometer described in the next section.

The $BaSO_4$ precipitate obtained at the beginning of the separation was dissolved in a sodium carbonate solution. The purification was done according to the procedure described in Kleinberg (1958). The final $BaCrO_4$ precipitate was dissolved in dilute HCl and the solution made up to a known volume. Aliquots were pipetted out on thin plastic films and the activities of the sources were measured by $4\pi\ \beta-\gamma$ coincidence techniques (Campion 1959).

(b) Counting

The sources of $Mg(NH_4)PO_4.6H_2O$ and Ni were covered with 42 mg/cm^2 of aluminum. This eliminated several counts of long-lived unidentified activities: it also completely cut out the low energy beta particles of Ni^{66} and most of those from Mg^{28}. Thus the anthracene counter detected only the beta radiations of Al^{28} and Cu^{66} in equilibrium with their parents Mg^{28} and Ni^{66}. The distance between the source and the detector was about 1 cm of air. The counting efficiency of the apparatus for the beta radiations of Al^{28} and Cu^{66} was 28%. The background of the detector was 8.5 ± 0.2 counts/min.

The intensity of the 0.48-Mev gamma ray of Be^7 in the BeO source was measured with a 3 in.$\times$3 in. NaI(Tl) crystal used in conjunction with a 100-channel pulse height analyzer. The efficiency of detection of the crystal for the 0.48 gamma ray was 11%.

RESULTS

(a) Determination of Fission Yields

The fission yield of Be, Mg, and Ni were calculated from the saturation activities of the species and of Ba^{140} produced in the same sample using the equation (Coryell and Sugarman 1951)

$$Y_B = \frac{S_B}{S_A} Y_A \tag{1}$$

where Y_B is the yield of the species to be calculated,
S_B is the saturation activity of the species at end of irradiation,
S_A is the saturation activity of Ba^{140} at end of irradiation,
and Y_A is the yield of Ba^{140} taken to be 6.44% (Katcoff 1958).

The saturation activities of Ba^{140} were obtained from the measured equilibrium activities of Ba^{140}–La^{140}, with the application of a correction factor (2.14) for transient equilibrium.

(b) Beryllium-7

In the examination of the two sources of BeO with the scintillation spectrometer no evidence was found for the presence of the 0.48-Mev gamma ray. Thus upper limits only could be set for the formation of Be^7; it was done in the following manner. Alternate measurements of the activities of the source and of background were repeated several times for periods of 30 minutes (for

sample 1) and of 10 minutes (for sample 2) over the energy range of 0.05 to 2 Mev. The absolute difference of the activities between the source and background in the 0.42 to 0.54 Mev interval was taken as a measure of the limit of the detection of the 0.48-Mev gamma ray of Be^7. The mean of the values of the several measurements recorded in succession was taken as the best estimate for the limit of detection of Be^7. The data for the calculation of the fission yield of Be^7 are given in Table II. In the calculation of the yield, the

TABLE II

Fission yield data for 53-day Be^7

	Run 1	Run 2
Nature of the uranium target	Natural	Enriched
Maximum activity of Be^7 extrapolated to the end of the irradiation (counts/min)	1.2	0.9
Abundance of the 0.48 Mev γ-ray (%)	11	11
Chemical yield (%)	73.8	35.0
Counting efficiency (%)	11.0	11.0
Disintegration rate of Be^7 at the end of the irradiation (d.p.s.)	2.23	3.54
Correction of disintegration rate for destruction of Be^7	2.45	3.89
Fractional saturation (16.6 hours)	9.04×10^{-3}	9.04×10^{-3}
Saturation activity of Ba^{140} (d.p.s.)	1.85×10^{9}	9.2×10^{9}
Saturation activity of Be^7 (d.p.s.)	2.71×10^{2}	4.3×10^{2}
Fission yield (%)	$<9.4\times10^{-7}$	$<3.0\times10^{-7}$

destruction cross section of Be^7 by thermal neutrons, the cross section of which is 4.8×10^4 barns (Hanna 1955), has been taken into account.

(c) Magnesium-28

The source of $Mg(NH_4)PO_4.6H_2O$ had a counting rate of 10 counts/min above background 31 hours after the end of the irradiation. This activity had decayed to 8.4 counts/min 4 days after the beginning of the counting of the sample. Since it represented 4.5 half-lives of Mg^{28}, 1.6 counts/min was taken as the maximum possible amount of activity due to Mg^{28} 31 hours after the end of the irradiation. Examination of the source with the scintillation spectrometer gave similar limits for the gamma radiations of the doublet Mg^{28}–Al^{28}. The value of 4.2×10^{-9}% is considered an upper limit for the fission yield of Mg^{28} since no positive identification of Mg^{28} was made. The data for the determination of the fission yield of Mg^{28} are presented in Table III.

TABLE III

Fission yield data for 21.3-hour Mg^{28}

Nature of the uranium target	Natural
Maximum activity of Al^{28} daughter at the end of irradiation (counts/min)	4.0
Chemical yield (%)	41.3
Counting efficiency of the 2.87-Mev beta-ray (%)	28.0
Disintegration rate of Mg^{28} at the end of irradiation (d.p.s.)	0.58
Fractional saturation (16.6 hours)	0.463
Saturation activity of Ba^{140} (d.p.s.)	1.85×10^{9}
Saturation activity of Mg^{28} (d.p.s.)	1.2
Fission yield (%)	$<4.2\times10^{-9}$

(d) Nickel-66

Evidence for the formation of Ni^{66} in the slow neutron fission of U^{235} has been found. An activity which decayed with a half-life close to that accepted for Ni^{66} (56-hour from the compilation of Strominger *et al.* 1958) has been measured in the two sources of Ni. Decay curves of the total activity and of that attributed to Ni^{66} are drawn in Fig. 1. From sample 2, the more

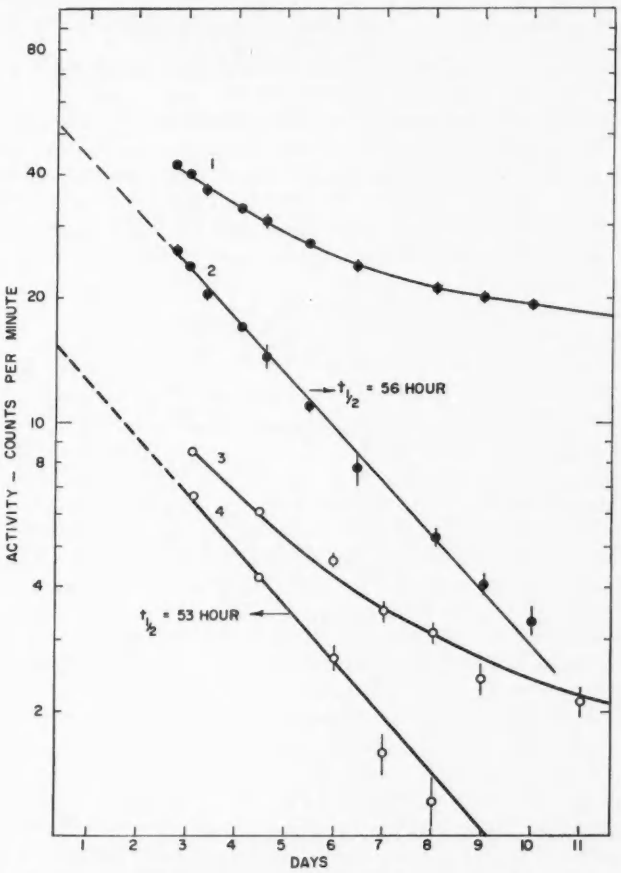

FIG. 1. Activities of Ni^{66} fraction: curves 1 and 3 gross decay curves; curves 2 and 4 activities attributed to Ni^{66}. Residual activities of 16 and 1.9 counts/min have been subtracted from curves 1 and 3, respectively, to obtain 2 and 4.

active source (from enriched sample), it was shown that the activity was definitively Ni^{66} by separation and measurement of the 5.1-minute daughter Cu^{66}. Four successive separations of copper sulphide in 2 *N* HCl from the purified nickel solution gave a CuS fraction with an average activity of

12 counts/min, 5 minutes (or one half-life) after the end of the separation. The activity of Ni^{66} from the decay curve 2 (Fig. 1) is 26 counts/min at the time of separation. This established clearly that the measured activity (curves 2 and 4, Fig. 1) was Ni^{66}.

The only reactions other than neutron fission of uranium which could possibly produce Ni^{66} are successive neutron capture in Ni^{64} as follows:

$$\underset{\text{stable}}{Ni^{64}} \longrightarrow (n,\gamma) \longrightarrow \underset{\text{2.36-hour}}{Ni^{65}} \longrightarrow (n,\gamma) \longrightarrow \underset{\text{56.6-hour}}{Ni^{66}}$$

(1.0% of natural Ni; cross sections 2 barns, 20 barns (Hughes and Schwartz 1958)).

The amount of Ni required to form the observed activity is calculated to be 0.1% in the natural uranium sample and 10% in the enriched sample. Analyses of the two samples gave 5 and 50 p.p.m. of Ni in natural and enriched samples respectively. Thus the reactions given above cannot be responsible for the formation of Ni^{66}. The data on the fission yield of Ni^{66} are assembled in Table IV. Considering the very low counting rate, which introduces a large

TABLE IV

Fission yield data for 56.6-hour Ni^{66}

	Run 1	Run 2
Nature of the uranium target	Natural	Enriched
Activity of 5.1-minute Cu^{66} daughter extrapolated to end of irradiation (counts/min)	15.0	53.0
Chemical yield (%)	57.0	56.3
Counting efficiency of the 2.6 Mev beta of Cu^{66} (%)	28.0	28.0
Disintegration rate of Ni^{66} at the end of irradiation	1.57	5.7
Fractional saturation	0.187	0.187
Saturation activity of Ni^{66} (d.p.s.)	8.7	30.0
Saturation activity of Ba^{140} (d.p.s.)	1.85×10^{9}	9.2×10^{9}
Fission yield (%)	2.9×10^{-8}	2.0×10^{-8}

error in the measurement, the agreement between the two yields is reasonable. More weight is given to experiment 2 and the best value for the fission yield of Ni^{66} is taken to be $2\pm1\times10^{-8}$%.

The nature of the process which resulted in the production of Ni^{66} is considered in the discussion which follows.

DISCUSSION AND CONCLUSIONS

A summary of the results are given in Table V. Unfortunately, because of time requirement, it was not possible to dissolve all the uranium target. It could then be argued that some of the elements could have been preferentially leached from the target. If this is the case, a systematic error amounting, perhaps, to a factor of 2 would arise in the yields given in Table V.

The present result for Be^{7} reduces, by a factor of 30, the limit of 10^{-5}% set by Cook (1952). It shows, in agreement with other investigators (Flynn *et al.* 1956; Titterton 1951*a*, *b*) that the formation of beryllium nuclei in the thermal neutron fission of U^{235} is an extremely rare event.

TABLE V

Summary of the results

Sample	Yields (%) in the slow neutron fission of U^{235}		
	Be^{7}	Mg^{28}	Ni^{66}
1	$<9.4\times10^{-7}$	$<4.2\times10^{-9}$	2.9×10^{-8}
2	$<3\times10^{-7}$	—	1.9×10^{-8}
Best value	$<3\times10^{-7}$	$<4.2\times10^{-9}$	$2.0\pm1.0\times10^{-8}$

The upper limit of $4.2\times10^{-9}\%$ for the yield of Mg^{28} indicates that the formation of fission products in the region of mass 30 are so rare that their detection will require major revision and refinements of current techniques. This result does not support the observation of Tsien *et al.* (1947, 1947*b*; cf. Table I), who have reported one case of tripartition with a fragment of mass 32 in nuclear emulsions.

It can be shown that fast fission of U^{235} or U^{238} cannot account for the observed yield of Ni^{66}. The fast fission cross section of U^{235} and U^{238} are 1.3 and 0.31 barns respectively and the fast neutron flux in the irradiation position used in the experiment is about 3% of the thermal flux. Hence the fast fission yield of Ni^{66} in the enriched and natural sample would have to be 14,000 and 300 times higher than its thermal fission yield in order to compete with thermal fission of U^{235}. The yields of fission products (Katcoff 1958) indicate that fast fission in a reactor could possibly increase the yield of an element like Ni^{66} only by a factor of 3 to 5. It is therefore concluded that Ni^{66} is a product of the thermal neutron fission of U^{235}, but the exact process cannot be decided on the basis of the radiochemical evidence. Binary fission cannot be ruled out because an extrapolation of the fission yields of light mass fragments (Katcoff 1958) gives 10^{-8}–$10^{-10}\%$ at mass 66, and this range borders on the observed value. One can only conclude that the yield of Ni^{66} is equal to or smaller than $2.0\pm1.0\times10^{-8}\%$ either for binary, triple, and quaternary fission.

Assuming that Ni^{66} is produced by tripartition it is of interest to compare the frequency with that observed in other investigations of tripartition. To do so it is necessary to further assume that Ni^{66} is formed in 1% of all tripartitions. This assumption is reasonable if Ni represents most of the yield of the mass 66 chain, if the splitting of the uranium nucleus in three fragments of comparable mass is the most favorable mode of tripartition, and finally if tripartition is not too narrow. On this basis the frequency of tripartition is one in 5×10^{7} binary fissions, a value much less than those reported by other workers and shown in Table I. The discrepancy could be explained if the yield of Ni^{66} in tripartition was very low; it would have to be $5\times10^{-3}\%$ to agree with the lowest value reported previously. Some causes which could have led to a confusion of a triple event for a tripartition in nuclear emulsions and in the work of Rosen and Hudson (1950) have been discussed in the Introduction. Our results indicate that the problem requires new measurements.

The nuclear emulsion techniques offer little possibility; it would take Herculean labors to examine enough fission events to settle the question. However, the type of experiment of Rosen and Hudson could be repeated with special attention to eliminate the interference of C, N, and O atoms (Demers 1958) in addition to all the other precautions taken by the same authors.

ACKNOWLEDGMENTS

The author wishes to acknowledge the assistance of Mr. J. J. Hawton with the radiochemical analyses. Also, appreciation is expressed to Mr. G. C. Hanna for his critical review of the manuscript.

REFERENCES

ALBENESIUS, E. L. 1959. Phys. Rev. Letters, **3** (6), 274.
ALLEN, K. W. and DEWAN, J. T. 1951. Phys. Rev. **82**, 527.
BOHR, N. and WHEELER, J. A. 1939. Phys. Rev. **55**, 426.
BUCHANAN, J. D. 1958. J. Inorg. & Nuclear Chem. **7**, 1740.
CAMPION, P. 1959. Intern. J. Appl. Radiation and Isotopes, **4**, 232.
CASSELS, J. M., DAINTY, J., FEATHER, N., and GREEN, J. L. 1947. Proc. Roy. Soc. A, **191**, 428.
CATALA, J., CASANOVA, J., and DOMINGO, V. 1959. Nature, **184**, 1057.
——— 1960. Anales real soc. espan. fis. y quim. LVI(A), No. 1–2, 29.
CHASTEL, R. and VIGNERON, L. 1949. Phys. Rev. **76**, 870.
COOK, G. B. 1952. Nature, **169**, 622.
CORYELL, C. D. and SUGARMAN, N. 1951. Introduction to Part IV. Radiochemical studies: the fission products, National Nuclear Energy Series, Division IV, Vol. 9 (McGraw-Hill Book Co., Inc., New York).
DELABOULAYE, H., TZARA, C., and OLKOWSKY, J. 1953. Compt. rend. **237**, 155.
——— 1954. J. phys. radium, **15**, 470.
DEMERS, P. 1946. Phys. Rev. **70**, 974.
——— 1947. Can. J. Research, A, **25**, 223.
——— 1953. Can. J. Phys. **31**, 78.
——— 1958. Ionographie, les émulsions nucléaires, principes et applications (Les Presses Universitaires de Montréal), p. 353.
DUTTA, S. P. 1953. Indian J. Phys. **27**, 547.
FLYNN, K. F., GLENDENIN, L., and STEINBERG, E. P. 1956. Phys. Rev. **101**, 1492.
GREEN, L. L. and LIVESEY, D. L. 1947. Nature, **159**, 332.
——— 1948. Phil. Trans. Roy. Soc. A, **241**, 323.
HANNA, R. C. 1955. Phil. Mag. **46**, 381.
HO, Z. W., TSIEN, S. T., VIGNERON, L., and CHASTEL, R. 1946. Compt. rend. **223**, 1119.
HUGHES, D. J. and SCHWARTZ, R. B. 1958. U.S. Atomic Energy Commission Report BNL-325, 2nd ed.
HURST, D. G. 1955. Proceedings of the International Conference on the Peaceful Uses of Atomic Energy, Vol. 5, 111.
HYDE, E. K. 1960. U.S. Atomic Energy Commission Report UCRL-9036.
KATCOFF, S. 1958. Nucleonics, **16** (4), 78.
KLEINBERG, J. 1958. Collected Radiochemical Procedures. Los Alamos Scientific Laboratory Report LA-1721, 2nd ed.
KRAUS, K. A. and NELSON, F. 1955. Proceedings of the International Conference on the Peaceful Uses of Atomic Energy, Vol. 7, 113.
MARSHALL, L. 1949. Phys. Rev. **75**, 1339.
METCALF, P. P., SEILER, J. A., STEINBERG, E. P., and WINSBERG, L. 1951. *In* Coryell, C. D. and Sugarman, N. Radiochemical studies: the fission products, National Nuclear Energy Series, Division IV, Vol. 9 (McGraw-Hill Book Co., Inc., New York), Papers 47–51.
MILTON, G. M. and GRUMMITT, W. E. 1957. Can. J. Chem. **35**, 541.
PERFILOV, N. A. 1958. *In* Physics of nuclear fission (Pergamon Press Ltd., London), Chap. 7, p. 84.
PRESENT, R. D. 1941. Phys. Rev. **59**, 466.
PRESENT, R. D. and KNIPP, J. K. 1940. Phys. Rev. **57**, 751, 1188.
ROSEN, L. and HUDSON, A. M. 1950. Phys. Rev. **78**, 533.
ROY, J. C. and WUSCHKE, D. 1959. Atomic Energy of Canada Limited, Report CRC-852.

STROMINGER, D., HOLLANDER, J. M., and SEABORG, G. T. 1958. Revs. Modern Phys. **30**, 385.
TITTERTON, E. W. 1951*a*. Nature, **168**, 590.
——— 1951*b*. Phys. Rev. **83**, 1076.
——— 1952. Nature, **170**, 794.
TREADWELL, F. P. and HALL, W. T. 1945. Analytical chemistry (John Wiley & Sons, Inc., New York), p. 259.
TSIEN, S. T., HO, Z. W., CHASTEL, R., and VIGNERON, L. 1947*a*. Compt. rend. **224**, 272.
——— 1947*b*. J. phys. radium, **8**, 165.
——— 1947*c*. Phys. Rev. **71**, 382.
TSIEN, S. T., HO, Z. W., VIGNERON, L., and CHASTEL, R. 1947. Nature, **159**, 773.
WHITEHOUSE, W. J. 1952. *In* Progress in nuclear physics, Vol. 2 (Academic Press Inc., New York), p. 120.

THE STATISTICAL BEHAVIOR OF INSTABILITIES IN DISPLACEMENT PROCESSES IN POROUS MEDIA[1]

ADRIAN E. SCHEIDEGGER[2] AND EDWARD F. JOHNSON[3]

ABSTRACT

The problem of growth of instabilities (fingers) in displacement processes in porous media is analyzed from a statistical viewpoint. The relative area occupied by fingers is represented as a "saturation", and the equations of motion for this "saturation" are derived. It is shown that these equations are analogous to the Buckley–Leverett equations of immiscible displacement, with a fictitious "relative permeability" being introduced. The latter can be calculated and thus the statistical equations of motion of a fingered-out front can be written down explicitly. These equations of motion can then be solved by the well-known method of characteristics. It is shown that the statistical theory does not lead to any stabilization of the fingers.

1. INTRODUCTION

The problem of instability has been of great importance with regard to displacement experiments in porous media and displacement processes in underground rock strata in which the displacing fluid is less viscous than the displaced fluid. It has been observed that, under the conditions just mentioned, protuberances may occur which may shoot through the porous medium at comparatively great speed. This phenomenon is called "fingering". A typical example of a fingered-out displacement front (after Terry *et al.* 1958), is shown in Fig. 1.

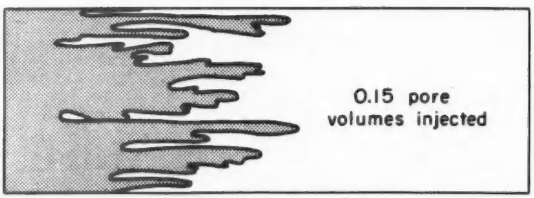

FIG. 1. Example of a fingered-out front after Terry *et al.* (1958).

In previous theoretical investigations (Chuoke *et al.* 1960; Scheidegger 1960*a*, *b*, 1961; Perrine 1960), the problem of fingering has been treated from a "microscopic" standpoint. In this, the displacement front was assumed as uniform, small disturbances were superimposed, the differential equations governing the growth of the latter were linearized, and the further behavior of the front was obtained by an integration. Any theory of this type is valid only for infinitesimally small ("microscopic") fingers. The result is invariably

[1]Manuscript received September 29, 1960.
Contribution from Imperial Oil Limited, Calgary, Alberta, and Jersey Production Research Company, Tulsa, Oklahoma (U.S.A.).
[2]Imperial Oil Limited, Calgary, Alberta.
[3]Jersey Production Research Company, Tulsa, Oklahoma.

that fingers, once started, should grow indefinitely (this is simply a consequence of the linearization of the equations). Emphasis has therefore been directed towards a determination as to whether instabilities of a certain wavelength do become started at all.

However, one of the big questions is whether an array of fingers could stabilize itself while it is progressing through the porous medium. In order to investigate this problem, it is not sufficient to deal with the linearized displacement equations since any existing fingers can no longer be regarded as infinitesimally small. Therefore, a different approach must be sought after.

In the present paper, it is proposed to treat the fingers statistically. Thus, only the average cross-sectional area occupied by the fingers is taken into account, the shape and size of the individual fingers are disregarded. The displacement of one fluid by the other is regarded as complete with no mixing occurring at the finger tips. The relative cross-sectional area occupied by the fingers is then analogous to a fictitious "saturation" of the displacing fluid in the porous medium. It turns out that the equation of motion for this "saturation" is similar to the Buckley–Leverett equation for the saturation change in immiscible, stable displacement, with a special expression for the relative permeability which becomes, in the present theory, a "fictitious" relative permeability. It is then necessary to introduce a theoretical model for the pressure distribution during the displacement. In particular, it is assumed that the pressures in adjacent elements in the two fluids are the same. This simplification will result in a description of a limiting case. With this theoretical model, it is possible to obtain a theoretical expression for the fictitious relative permeability. The solution for the spreading of fingers in a linear displacement experiment with fingering is then obtained and it is shown that the present theory does not yield any possibility of stabilization of the fingers.

Owing to the simplicity of the theoretical model employed, more than a qualitative agreement with experimental data ought not to be expected. In any theoretical treatment of fingers, simplifications either at the microscopic (linear wave theory) or at the macroscopic level (present theory) have to be introduced. It is believed that the present attempt is the first instance of a treatment of fingers on the macroscopic level.

2. THE MUSKAT MODEL

The present treatment of the fingering process will be based upon what has been called the *Muskat model* of displacement theory, indicating its originator. This model assumes that there is a sharp front between the displacing and the displaced fluid, and that on each side the flow proceeds according to Darcy's law, based on the corresponding viscosity. The Muskat model does not specify whether the fluids are miscible or immiscible, since only saturations (concentrations) of zero or unity are allowed.

The Muskat model represents an oversimplification of the actual facts inasmuch as some mixing will always occur at the interface between two fluids. Nevertheless, it is known that it yields acceptable results in many cases.

3. STATISTICS OF FINGERS

As noted in the Introduction, in endeavoring to describe the fingering process from a macroscopic standpoint, one is concerned only with the average behavior of the two fluids involved.

Thus, consider a linear displacement experiment parallel, say, to the $+x$-direction which progresses with time (t). For certain values of x and t, there will be some fingers present.

The fingers present in the porous medium can be schematically drawn as represented in Fig. 2. The problem, then, is to set up a determining equation

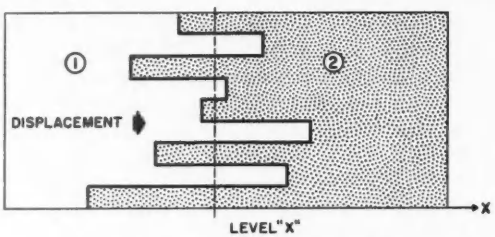

FIG. 2. Schematic representation of fingers.

for the function

$$s_i = s_i(x,t) \tag{3.1}$$

where s_i represents the average relative area occupied by the ith fluid at the level x.

This is done as follows: Using Darcy's law for each of the phases, the pore velocities v_1 and v_2 (referring to the displacing and displaced fluids, respectively) are obtained according to the following equation of motion

$$v_i = \frac{k}{\mu_i P} \operatorname{grad} p, \tag{3.2}$$

where k is the permeability of the medium, P its porosity, and μ_1, μ_2, are the viscosity of the displacing and displaced fluid, respectively. Furthermore, p is the local pressure.

The theory cannot be carried further at this stage without assuming that, at the level x, the pressure p does not vary along any line on that level (a modification could be made, however, allowing for a capillary pressure differential between the two fluids). Thus at the level x, the pressure is uniform. This leads to an expression for the flow of the phase i across the unit of area

$$q_i = \frac{k s_i}{\mu_i} \operatorname{grad} p. \tag{3.3}$$

The problem is determined, if in addition to the equations of motion (3.3) the continuity conditions are considered

$$P \frac{\partial s_i}{\partial t} = -\operatorname{div} q_i, \tag{3.4}$$

$$s_1+s_2 = 1. \tag{3.5}$$

It is assumed, then, that the fluids involved are incompressible.

Equations (3.3), (3.4), and (3.5) constitute the equations describing the average behavior of fingers in the present theory.

4. FICTITIOUS RELATIVE PERMEABILITY

The statistical treatment of the fingers outlined in the last section leads to a description of the displacement process which is formally identical with the description of immiscible displacement by means of "relative permeabilities" (denoted by k_i).

One could have arrived at such a description of fingers also from a direct analogy with relative permeability. Accordingly, by again considering a linear displacement parallel to the x-direction and an analogy with immiscible displacement, it stands to reason that the behavior of the "saturation" s (i.e. the relative area occupied by fingers) as a function of x and t can be treated in a manner analogous to the saturation in the Buckley–Leverett theory of immiscible displacement.

Thus, a "fictitious relative permeability" is introduced which describes the seepage flow q_i of each phase

$$q_i = -k\frac{k_i}{\mu_i}\operatorname{grad} p \tag{4.1}$$

where k is the total permeability, μ_i the viscosity of the phase under consideration, and grad p the pressure gradient. This, together with the continuity equations

$$P\frac{\partial s_i}{\partial t} = -\operatorname{div} q_i, \tag{4.2}$$

$$\sum s_i = 1, \tag{4.3}$$

(where P is the porosity) fully describes the flow process if the two fluids are taken as incompressible. It is assumed that the k_i's are functions of s_i only.

It is well known that the above equations have an eliminant

$$P\frac{\partial s_1}{\partial t} + r'(s_1)q_x\frac{\partial s_1}{\partial x} = 0 \tag{4.4}$$

with q_x denoting the filtration velocity in the x-direction and

$$r(s) = \frac{k_1/\mu_1}{k_1/\mu_1+k_2/\mu_2}. \tag{4.5}$$

The problem now is to find a suitable expression for $k_i(s)$. From the analogy with "relative permeability" only, it is not possible to arrive at such an expression. However, by recalling the remarks on the statistical description of fingers made in the previous section, it is apparent that one must set

$$k_i = s_i. \tag{4.6}$$

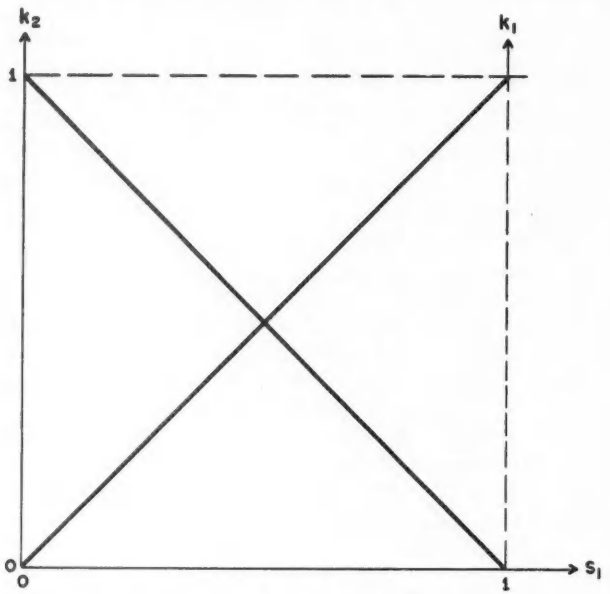

FIG. 3. Fictitious relative permeability curves.

The corresponding "relative permeability curves" are shown in Fig. 3. Using eq. (4.5) and eq. (4.6) the expression for r as a function of s becomes

$$r(s_1) = \frac{s_1/\mu}{s_1/\mu_1+(1-s_1)/\mu_2} = \frac{m}{m-1+1/s_1} \tag{4.7}$$

with

$$m = \mu_2/\mu_1. \tag{4.8}$$

It will now be convenient to drop the index 1 referring to the displacing fluid. Thus r and its first and second derivatives with respect to s become

$$r(s) = \frac{m}{(m-1)+1/s}, \tag{4.9}$$

$$r'(s) = \frac{m}{[s(m-1)+1]^2}, \tag{4.10}$$

$$r''(s) = -\frac{2m}{[s(m-1)+1]^3}(m-1). \tag{4.11}$$

The shapes of the $r(s)$ and $r'(s)$ curves for a typical case are those given in Figs. 4 and 5 respectively. It is obvious that $r(s)$ has no inflection point, $r'(s)$ no extremal values, so that no shock front can develop (cf. the discussion in Scheidegger's (1960*c*) book, p. 224).

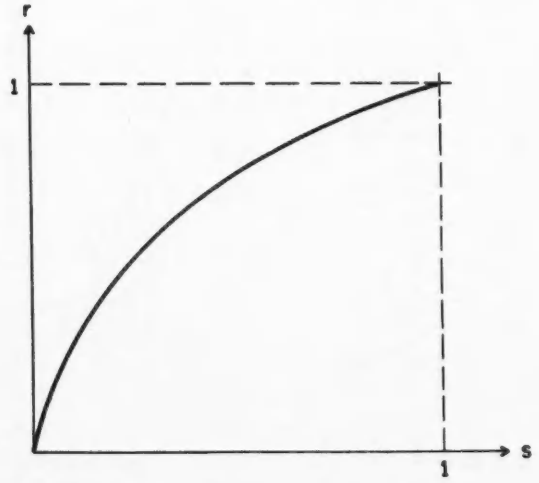

FIG. 4. Fractional flow curve for a typical case.

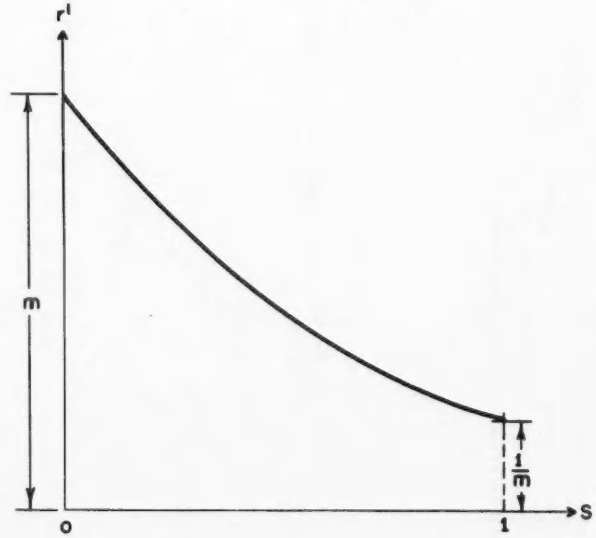

FIG. 5. Derivative of fractional flow for a representative case.

5. THE SPREADING OF FINGERS

In order to determine the behavior of fingers as described in the present theory, it will be necessary to find appropriate solutions of the eliminant equation (4.4). Solutions of this equation can be obtained most easily by the method of characteristics. The characteristic equations corresponding to (4.4) are

$$\frac{dx}{dt} = r'(s)q_x(t)/P \tag{5.1}$$

$$ds/dt = 0. \tag{5.2}$$

Thus, eqs. (5.1) and (5.2) describe the paths along which a constant saturation moves. Inserting eq. (4.10) into eq. (5.1), results in

$$\frac{dx}{dt} = \frac{m}{[s(m-1)+1]^2}\frac{q_x(t)}{P} \tag{5.3}$$

which yields upon integration

$$x = \frac{m}{[s(m-1)+1]^2}\frac{1}{P}\int_0^t q(t)dt. \tag{5.4}$$

Assuming the over-all injection velocity as constant, the equation for the characteristic lines can be expressed as

$$x = \frac{mt}{[s(m-1)+1]^2} \times \text{const.} \tag{5.5}$$

where the "const." depends only on the porosity and the injection velocity (and is thus independent of the viscosity ratio). The characteristics, thus, are straight lines; they are shown in Fig. 6.

Assuming that the displacement in the porous medium starts with a sharp front, one can now calculate its spread due to fingering. Since the characteristics are straight lines in the $x-t$ plane, the speed $c(s)$ with which each saturation value proceeds, is given by the slope of that line:

$$c(s) = \text{const.}\frac{m}{[s(m-1)+1]^2} \tag{5.6}$$

where the "const." is the same as that in eq. (5.5). The speed for each saturation value is independent of time; thus the distance $x(s)$ to which it travels is given by $c(s)t$:

$$x(s) = \text{const.}\frac{m}{[s(m-1)+1]^2}t. \tag{5.7}$$

This is the connection between x and s for the time t which is sought after. A sketch of it is given in Fig. 7.

The manner in which time is involved in eq. (5.7) shows that no stabilization is possible in the present model of fingering. The basic form of the saturation curve (Fig. 7) simply grows ad infinitum by similarity stretching.

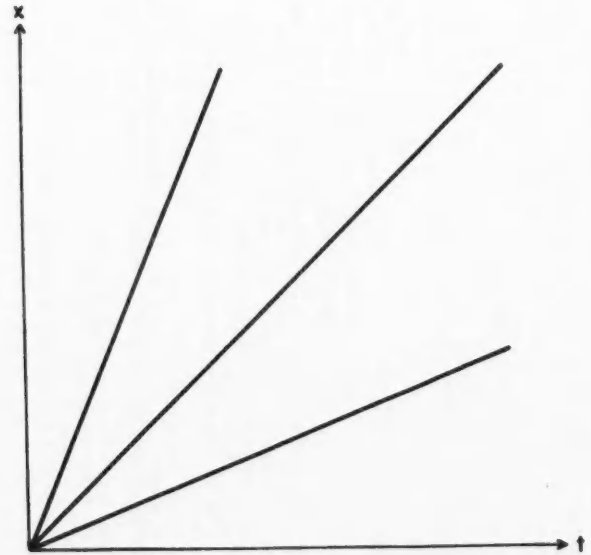

FIG. 6. Characteristics for the fingering problem.

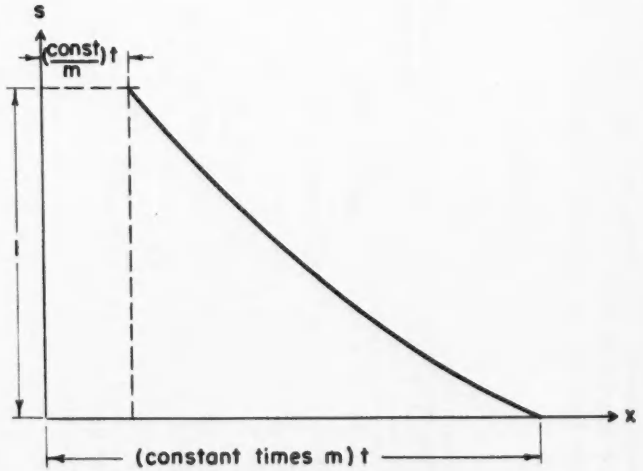

FIG. 7. Distribution of saturation as a function of distance.

It may be of interest to rewrite the above formulas in terms of pore volumes ($\bar{t}$) and pore lengths ($\bar{x}$). Thus, considering a system of length L, one may introduce the following dimensionless variables:

$$\bar{t} = \int_0^t q_x dt/(PL) \tag{5.8}$$

$$\bar{x} = x/L. \tag{5.9}$$

Then one has from (5.4)

$$\bar{x} = \frac{m}{[s(m-1)+1]^2}\bar{t}. \tag{5.10}$$

The *break-through value* of $\bar{t}$ is obtained if s is set equal to zero, and $\bar{x}$ equal to 1; hence

$$\bar{t}_{\text{break-through}} = 1/m. \tag{5.11}$$

Similarly, the value of $\bar{t}$ for complete recovery is obtained if s is set equal to 1 and $\bar{x}$ equal to 1; hence

$$\bar{t}_{\text{complete recovery}} = m. \tag{5.12}$$

It is obvious from eqs. (5.11) and (5.12) that the above development can only have meaning when $m \geqq 1$.

NOMENCLATURE

$c(s)$ = velocity of saturation movement (cm sec^{-1}).
k = permeability (cm^2).
k_i = relative permeability (fractional; dimensionless).
L = length of a system (cm).
m = viscosity ratio (dimensionless).
p = pressure (g cm^{-1} sec^{-2}).
P = porosity (fractional; dimensionless).
q = filtration velocity (cm sec^{-1}).
r = fractional flow (dimensionless).
s = fictitious saturation (fractional; dimensionless).
t = time (sec).
v = velocity (cm sec^{-1}).
x = linear co-ordinate (cm).
μ = viscosity (g cm^{-1} sec^{-1}).

REFERENCES

CHUOKE, R. L., VAN MEURS, P., VAN DER POEL, C. 1960. Trans. AIME, **216**, T.P. 8073.
PERRINE, R. L. 1960. Conditional instability in miscible liquid–liquid displacement, Paper No. 42, 52nd. AICh.E. Meeting, San Francisco. Preprint, 33 pp.
SCHEIDEGGER, A. E. 1960*a*. Can. J. Phys. **38**, 153.
——— 1960*b*. Phys. Fluids, **3**, 94.
——— 1960*c*. The physics of flow through porous media, revised edition (University of Toronto Press).
——— 1961. Geofis. pura e appl. **47**. In press.
TERRY, W. M., BLACKWELL, R. J., RAYNE, J. R. 1958. Factors influencing the efficiency of miscible displacement, AIME Paper No. 1131-G.

EQUIVALENCE BETWEEN CONTINUOUS AND DISCRETE RADIATING ARRAYS[1]

A. KSIENSKI

ABSTRACT

The radiation patterns produced by continuous excitation distributions and discrete arrays are compared and the conditions are derived under which one type of source may be substituted for the other with negligible errors. It is shown that the aperture lengths in both cases should be the same but the element spacing is dependent on the type of pattern desired. Examples are computed to demonstrate these relations for both directive patterns and shaped beams.

INTRODUCTION

The pattern synthesis problem received considerable attention in the past, and a large amount of information is presently available. Many of the results are given for continuous distributions; in practice, however, it is hard to control amplitude and phase independently across a continuous aperture. Usually, then, the continuous excitation distribution is used as the envelope for the excitations of a discrete array. It is the purpose of the present paper to examine the relationship between continuous and discrete arrays and estimate the errors involved in substituting one for the other.* It is shown that the current practice of using the continuous distribution as an envelope is justified in most cases. It is also shown that the parameter to be adjusted for different classes of patterns is the element spacing and that the aperture width should remain the same if the error tolerance is to be preserved. Examples are computed to show these effects for patterns of greatest interest, namely directive beams and cosecant squared patterns.

THE EQUIVALENCE THEOREM

Let $F(u)$ represent the pattern produced by a linear aperture with a continous distribution ($u = \pi \sin \theta$, where θ is the observation angle). Let $P(u)$ represent the pattern produced by a linear array of point sources. It will be shown that under certain conditions $P(u) = F(u)$. If the array represents a Fourier series it can also be shown that the feeding coefficients A_n are proportional to the continuous distribution at corresponding points.

Let $F(u)$ be a function prescribed for $-\pi \leqslant u \leqslant \pi$ under the following conditions:

No. 1. $F(u)$ is of bounded variation (which is satisfied by almost all practical patterns);

No. 2. $F(u) = 0$ for $|u| > \pi$.

[1]Manuscript received September 6, 1960.

Contribution from the Aerospace Engineering Division, Hughes Aircraft Company, Culver City, California.

*Several of the mathematical results derived in this paper may be obtained from Shannon's sampling theorem. It was felt, however, preferable to derive all the results in a consistent form in antenna terminology rather than to transcribe formulas derived in another field and attempt to justify their applicability, particularly in view of the simplicity of the mathematics involved.

The second condition is closely approached by a large number of directive patterns. Let the continuous excitation distribution which produces $F(u)$ be given by $g(p)$ where p is the spatial, or position variable, measured in half wavelengths ($p = x/(\lambda/2)$). Then (Silver 1949)

$$F(u) = \int_{-\infty}^{\infty} g(p)e^{jpu}dp, \tag{1}$$

$$g(p) = \frac{1}{2\pi}\int_{-\infty}^{\infty} F(u)e^{-jpu}du. \tag{2}$$

However, if $F(u) = 0$ for $u > \pi$, then

$$g(p) = \frac{1}{2\pi}\int_{-\pi}^{\pi} F(u)e^{-jpu}du. \tag{3}$$

Now consider an array of discrete sources which are represented by an orthogonal set of functions, whose orthogonality is defined over the range from $-\pi$ to π. For example, a set of $2N+1$ point sources, where consecutive sources are displaced by a distance $\lambda/2$ from each other, the resultant pattern of such an array will be given by

$$P(u) = \sum_{-N}^{N} A_n e^{jnu} \tag{4}$$

where $u = \pi \sin\theta$, and where A_n are the amplitude and phase of the excitation coefficients. In order to approximate $F(u)$ by means of $P(u)$ we have to determine appropriately the coefficients A_n of $P(u)$. The coefficients are given by

$$A_n = \frac{1}{2\pi}\int_{-\pi}^{\pi} F(u)e^{-jnu}du. \tag{5}$$

The right-hand side of equation (5) is identical with the one of equation (3) except for n replacing p. Hence,

$$A_n = g(n). \tag{6}$$

Thus it is seen that the feeding coefficients A_n for the discrete array are obtained from the continuous distribution $g(p)$ by inserting the proper integer. Hence for any pattern $F(u)$ obeying condition No. 2, its Fourier transform forms the envelope of its Fourier coefficients.

No mention has been made yet of the size of the aperture, or the total number of sources. Assume the continuous aperture producing $F(u)$ is M wavelengths wide, namely

$$g(p) = 0 \qquad \text{for } |p| > M.$$

Actually $g(p)$ can be only approximately zero for $p > M$, but M being arbitrary, it may be so chosen as to make $g(p)$ as close to zero as desired for $p > M$. (Otherwise the integral in equation (1) would not converge.) We will show now that the necessary discrete array is also M wavelengths wide. Using equation (6)

$$A_n = g(n)$$

and from the above condition on $g(p)$ it follows the

$$A_n = 0 \qquad \text{for } |n| > M$$

or all feeding coefficients beyond the Mth will be zero. This requires that the array have $2M+1$ sources, or be M wavelengths long, i.e. the same as the continuous aperture.

We shall presently prove that the pattern produced by the discrete array would be exactly $F(u)$ if the condition that $g(p) = 0$ for $|p| > M$ were satisfied. Given a complete orthonormal set of functions $\{f_n(u)\}$ defined over the interval $-\pi \leqslant u \leqslant \pi$, and given $F(u)$ on the same interval and subject to condition No. 1 the summation $\sum \gamma_n f_n(u)$ converges to $F(u)$ where γ_n are given by (Courant and Hilbert 1953)

$$\gamma_n = \int_{-\pi}^{\pi} F(u) f_n^*(u) du. \tag{7}$$

The set $\{\epsilon^{\pm jnu}/\sqrt{2\pi}\}$ where $n \to \infty$ is a complete orthonormal set, hence

$$F(u) = \sum_{-\infty}^{\infty} A_n \epsilon^{jnu} \tag{8}$$

where

$$A_n = \gamma_n/\sqrt{2\pi}. \tag{9}$$

However, all A_n are zero for $|n| > M$, hence

$$F(u) = \sum_{-M}^{M} A_n \epsilon^{jnu} = P(u), \tag{10}$$

which proves that the pattern has been exactly reproduced by the discrete array. Note that $F(u)$ was specified only over the interval $|u| \leqslant \pi$, and the discrete array of $2M+1$ elements will reproduce $F(u)$ exactly over that interval. The equality between $F(u)$ and $P(u)$ breaks down, of course, outside the visible range that is, for $|u| > \pi$, due to the essential difference between the Fourier series and the Fourier transform. It might be well to point out that one cannot have both $F(u)$ and $g(p)$ vanish identically outside a finite range of the variables, hence the assumption that $g(p) = 0$ for $|p| > M$ implies that $F(u)$ does not identically vanish for $|u| > \pi$ although its magnitude may be as small as desired. This means that if one expects to approximate very closely a desired pattern by means of a finite aperture one has to refrain from specifying $F(u)$ to vanish outside the visible range. In this respect the discrete array is somewhat less restricted since in the latter case one has to request only that $g(p)$ vanish at integral values of p.

Error Evaluation

If condition No. 2 is satisfied only approximately an error will result in the excitation distribution that will be proportional to that part of the integral which was neglected in the Fourier expansion. More often the practical

approximation problem will be of the following nature. The continuous aperture which is finite in extent will usually not be sufficient to contain the distribution $g(p)$ required for the prescribed pattern. In other words, the actual span of the aperture is only a portion of that required by an exact synthesis. For example, the required length is M wavelengths where M is very large and the available aperture is only N wavelengths wide, where $N < M$. This results in an error in the desired pattern $F(u)$. Let us denote this resulting pattern by $F_e(u)$. The discrete array of the same span will likewise produce an approximate pattern $P_e(u)$. However, the error produced by the discrete array will not necessarily be larger than that of the continuous aperture. If we denote the mean square error caused by the continuous aperture as E_c and that of the discrete array as E_d we shall obtain for the discrete array,

$$(11) \qquad E_d = \frac{1}{2\pi}\int_{-\pi}^{\pi} |F(u)-P_e(u)|^2 du = \frac{1}{2\pi}\int_{-\pi}^{\pi} \left| F(u)-\sum_{-N}^{N} A_n \epsilon^{jnu} \right|^2 du$$

$$= \frac{1}{2\pi}\int_{-\pi}^{\pi} |F(u)|^2 du - \sum_{-N}^{N} A_n^2$$

then

$$(12) \qquad E_d = \sum_{-M}^{-N} |A_n|^2 + \sum_{N}^{M} |A_n|^2.$$

For the continuous aperture

$$(13) \qquad E_c = \frac{1}{2\pi}\int_{-\pi}^{\pi} |F(u)-F_e(u)|^2 du = \frac{1}{2\pi}\int_{-\pi}^{\pi} \left| F(u)-\int_{-N}^{N} g(p)\epsilon^{jpu} dp \right|^2 du$$

$$= \frac{1}{2\pi}\left\{ \int_{-\pi}^{\pi} |F(u)|^2 du + \int_{-\pi}^{\pi} |F_e(u)|^2 du \right\} - 2\int_{-N}^{N} |g(p)|^2 dp.$$

Using Parseval's relations in equation (13) we obtain

$$(14) \qquad E_c = \int_{-M}^{M} |g(p)|^2 dp - \int_{-N}^{N} |g(p)|^2 dp$$

where we have assumed that $F_e(u)$ is negligibly small for $|u| > \pi$, i.e., that its contribution to the total error is small. This assumption is justified in the majority of patterns, particularly the directive ones. From equation (14) we can see that the error in the case of the continuous distribution is proportional to the part of the area of $|g(p)|^2$ which was left out due to the finite extent of the aperture. In the discrete distribution the error is proportional to the sum of the $|A_n|^2$ which were left out due to the finite extent of the discrete array. Clearly the two errors are very close to each other. In the case that $F_e(u)$ is not negligible in the range $|u| > \pi$ additional terms have to be included in the error expression

$$(14a) \qquad E_c = \int_{-M}^{M} |g(p)|^2 dp - \int_{-N}^{N} |g(p)|^2 dp - \frac{1}{2\pi}\int_{-\infty}^{-\pi} |F_e(u)|^2 du$$

$$- \frac{1}{2\pi}\int_{\pi}^{\infty} |F_e(u)|^2 du.$$

The last two terms reduce the error of the continuous aperture in comparison to the discrete one. This reduction is actually a correction term since the first two terms in equation (14*a*) represent the total r.m.s. deviation of $F_e(u)$ from $F(u)$ for all values of u over the infinite range, while E_e is the r.m.s. error over the finite limits $\pm\pi$. Thus it is clear that in the case where the continuous aperture produces a pattern which significantly extends into the invisible range the discrete array of half wavelength spaced elements will produce a poorer approximation. This case is discussed in more detail in the following sections where the appropriate inter-element spacing is derived in order to approximate more closely the continuous aperture.

We now consider an example of the case where condition No. 2 is only approximately satisfied (Fig. 1). Then we compare in Figs. 2 and 3 the patterns

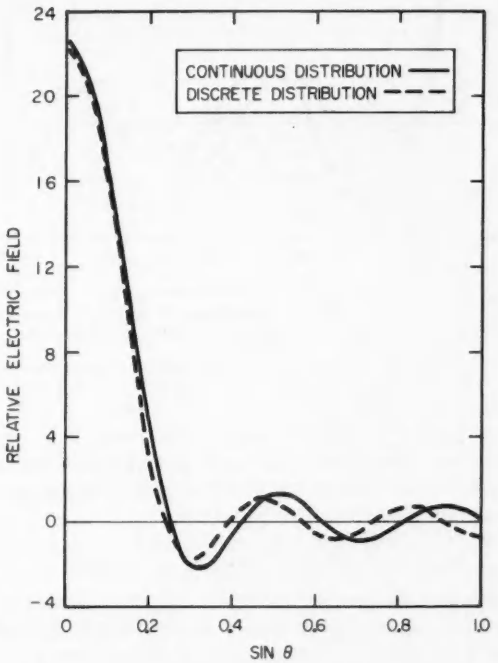

FIG. 1. Patterns produced by a Taylor excitation distribution. Comparison between a continuous distribution 5λ long and an array of 11 elements spaced half wavelength apart.

of uniformly illuminated continuous apertures and corresponding discrete arrays which illustrate the case when both only approximate a desired pattern.

Examples

Taylor Pattern

A Taylor pattern (Taylor 1953)

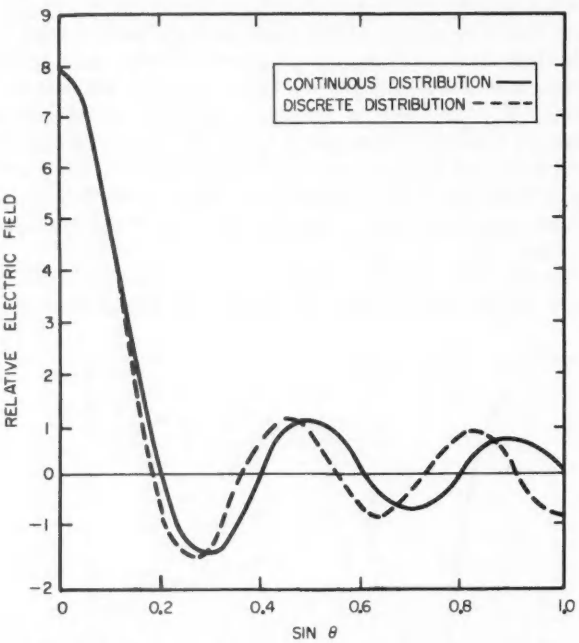

FIG. 2. Patterns produced by a uniform illumination. Comparison between a continuous distribution 5λ long and an array of 11 elements spaced half wavelength apart.

$$(15) \qquad F(u) = \frac{\sin \pi\sqrt{(u^2-B^2)}}{\pi\sqrt{(u^2-B^2)}} \qquad u = \frac{2a}{\lambda}\sin\theta; \qquad a = \frac{5\lambda}{2}$$

satisfies condition No. 2 approximately, and the patterns produced by the continuous distribution and the discrete array should be approximately the same. The continuous distribution is given by

$$(16) \qquad g(p) = J_0[jB\sqrt{(\pi^2-p^2)}]; \qquad p = \pi x/a$$

where $B = 0.7386$ and the aperture width $= 5\lambda$. Now compare this with a discrete array which consists of 11 source points, at $\lambda/2$ separation, so the over-all distance is 5λ. The excitation coefficients are

$$(17) \qquad A_n = J_0\left\{jB\sqrt{\left[\pi^2\left(1-\left(\frac{n}{5}\right)^2\right)\right]}\right\}.$$

As is seen from Fig. 1 the patterns are quite similar to each other. The main beam of the discrete array is somewhat narrower and the sidelobes are shifted correspondingly. The physical reason for this behavior is that the "space factor" effect of a point source is equivalent to a half wavelength aperture centered at the point source. Hence an array consisting of N point

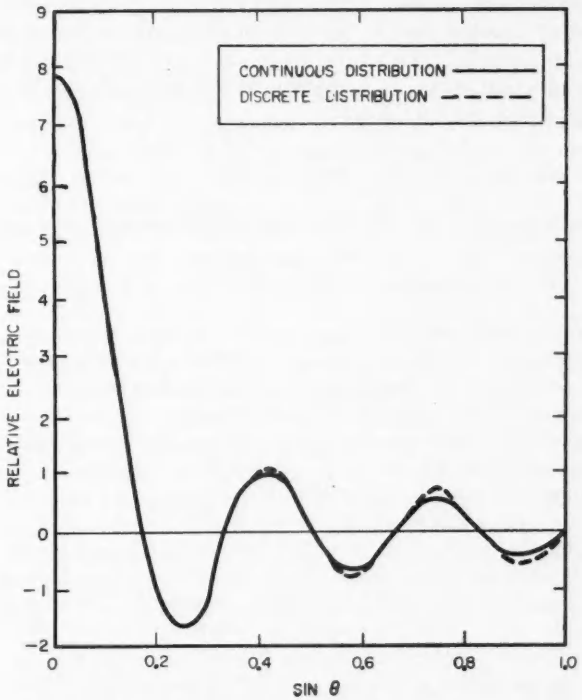

FIG. 3. Patterns produced by a uniform illumination. Comparison between a continuous distribution 6λ long and an array of 12 elements spaced half wavelength apart, i.e., 5½λ long.

sources spaced $\lambda/2$ apart may be considered to be equivalent to an array $N/2$ wavelengths long rather than $(N-1)/2$ which is the physical length of the array. The main difference lies in the element factor of a half wavelength continuous aperture which multiplies the pattern of the continuous aperture and thus progressively reduces the sidelobes. The mathematical explanation can be obtained directly from the error formulas, equations (12) and (14). Thus imagine an aperture distribution which vanishes at a distance of $(N+\frac{1}{2})$ half wavelengths from the origin. From equation (12) it is clear that an array of $2N+1$ sources would produce the exact pattern since all terms after the Nth would vanish, thus the array would be N wavelengths long. On the other hand the continuous distribution $g(p)$ would have to extend to $(N+\frac{1}{2})$ half wavelengths on each side of the origin to produce the exact pattern. This would result in an aperture whose length would be $(N+\frac{1}{2})\lambda$, or one half wavelength longer than the discrete array. From these considerations it is clear that this effect may result in a difference of up to one wavelength. (This limit depends on the orthogonality interval for which the Fourier expansion is defined.)

Uniform Illumination

Another rather classical case is the uniform illumination. Let us examine and compare the pattern produced by the continuous distribution versus the corresponding discrete array. A uniformly illuminated aperture of over-all dimension a produces the field pattern,

$$F_e(u) = A\frac{\sin[(\pi a/\lambda)u]}{u} \qquad -1 \leqslant u \leqslant 1 \tag{18}$$

while for a discrete array of N half wavelength spaced elements the pattern is

$$P_e(u) = B\frac{\sin[(N/2)\pi u]}{\sin[(\pi/2)u]}. \qquad -1 \leqslant u \leqslant 1 \tag{19}$$

The reason that the subscript (e) was attached to the above pattern expressions is due to the fact that the uniform illumination is the result of attempting to produce a delta function whose Fourier transform is a constant. However, due to the finiteness of the aperture the excitation is cut off at a finite distance from the origin. Thus both the continuous and the discrete distribution are finite approximations to the required distribution. Consider a continuous aperture 5λ long and uniformly illuminated and an array of the same length with its element spaced $\lambda/2$ apart thus consisting of 11 elements. From Fig. 2 one can see that the resulting patterns are quite similar except for the effects that occurred in the previous example, that is, the main beam is narrower in the discrete case and the sidelobes shifted accordingly. As an additional example consider a 6λ continuous aperture and compare it to $5\frac{1}{2}\lambda$ discrete array, both uniformly illuminated. In the present case (see Fig. 3) the two patterns are almost identical and the only difference is in the sidelobe ratio. The difference between the patterns shown in the above example is a good indication of what one might expect in substituting a discrete array for a continuous aperture. It might be worth noting that the good agreement between the patterns is due to the fact that all of the above patterns approximate quite closely condition No. 2.

Energy Consideration

Observe that condition No. 2 refers to the invisible range ($|u| > \pi$) of $u = \pi \sin\theta$. The behavior of $F(u)$ in that range is related to the reactive energy stored in the vicinity of the antenna (Woodward and Lawson 1948). Thus the physical significance of condition No. 2 is the requirement that the antenna be predominantly resistive, namely, that it should be an efficient radiator. It may be interesting to note that whenever Fourier coefficients are computed, the integration is carried out only over the visible range ($|\sin\theta| \leqslant 1$). Thus if the pattern of the continuous aperture has a large value of $F(u)$ in the region $|u/\pi| = |\sin\theta| > 1$ it would not carry over into the discrete array. This implies that an array representing a Fourier set of functions is of low reactive nature, and, for example, free from supergain effects.*

*The reactive energy would, of course, be infinite if one were to consider infinitesimal elements, since the pattern would repeat indefinitely in the invisible range. The finite size, however, of physical elements insures that the pattern vanish for $u \gg 1$.

THE EQUIVALENCE FOR PATTERNS NOT SUBJECT TO CONDITION NO. 2

For most cases the assumption of $F(u) = 0$ for $u > \pi$ is quite realistic, that is, $F(u)$ is either zero or close to zero. This condition implies directive beams, for which the pattern is desired to vanish outside a small interval of u covering the main beam. We shall presently extend the treatment to non-directive patterns which require a non-vanishing signal for the end of the visible range, namely a certain amount of "end fire" energy. For such patterns $F(u)$ usually vanishes outside an interval $\pm\sigma\pi$ where $\sigma > 1$. We will show that if the function $F(u)$ is non-zero for intervals larger than π, the spacing of the elements in the array necessary for good pattern agreement decreases to values smaller than $\lambda/2$. This indicates mathematically that the array is susceptible to increased amounts of reactive energy. The same is clear from physical considerations due to the increased coupling between elements caused by their proximity to each other. As the interval for which $F(u) \neq 0$ tends to infinity the spacing tends to zero, producing a continuous distribution. The converse is also true, namely, if $F(u) = 0$ outside an interval of u smaller than π the spacing between the elements may be larger. The faster $F(u)$ vanishes the larger can the spacing between the elements become. This would permit the use of fewer elements in the antenna without increasing the error of approximation. This last effect, however, is not very useful, since for spacing much larger than $\lambda/2$ the pattern will repeat in the visible range, producing a main beam or a portion of it in the sidelobe region.

Consider $F(u) = 0$ for $u \geqslant \sigma\pi$ where $\sigma > 1$. Using the same notation as before

$$g(p) = \frac{1}{2\pi}\int_{-\infty}^{\infty} F(u)\epsilon^{-jpu}du = \frac{1}{2\pi}\int_{-\sigma\pi}^{\sigma\pi} F(u)\epsilon^{-jpu}du. \tag{20}$$

In order to obtain relations similar to the previous ones between the discrete and continuous excitations, we consider a set of functions ω_n defined to be orthogonal over the interval form $-\sigma\pi$ to $+\sigma\pi$. Then

$$\int_{-\sigma\pi}^{\sigma\pi} \omega_k \cdot \omega_l du = 0 \qquad \text{for } k \neq l$$

and

$$A\int_{-\sigma\pi}^{\sigma\pi} \omega_k \cdot \omega_l du = 1 \qquad \text{for } k = l \tag{21}$$

where A is a constant independent of k and l.

Let us consider a linear array of radiators and determine how the above requirement can be met. The pattern of such an array is given by

$$P(u) = \sum_n A_n e^{jnau} \tag{22}$$

where $u = \pi \sin\theta$, and a is the distance in half wavelengths between consecutive radiators. To approximate a prescribed pattern $F(u)$, let

$$F(u) \simeq \sum_n A_n e^{jnau} \tag{23}$$

where

$$A_n = \frac{a}{2\pi} \int_{-\pi/a}^{\pi/a} F(u) e^{-jnau} du.$$

Note that if we let $a = 1/\sigma$ we obtain

$$A_n = \frac{1}{2\pi\sigma} \int_{-\pi\sigma}^{\pi\sigma} F(u) e^{-jn(u/\sigma)} du, \tag{24}$$

which is the desired result, and $\omega_n = e^{jn(u/\sigma)}$. The above relation means that the distance between consecutive sources has to decrease from $\lambda/2$ by the same factor as the range of $F(u) \neq 0$ extends beyond $\pm\pi$ to permit the synthesis of the pattern in the invisible range as well as in the visible portion. As $F(u)$ extends more into the invisible range, the spacing of the sources decreases producing more coupling, and acquiring more of the disadvantages of continuous distributions and making the physical construction of the array almost as hard, if not harder, than the continuous distribution.

Example

To give an example of a pattern that benefits by spacing the array elements at distances somewhat smaller than $\lambda/2$ we now consider a pattern which is required to have a non-vanishing signal at one end of the visible range ($u = \pi$) and zero signal at the other ($u = -\pi$). The desired pattern is specified as

$$F(u) = \frac{1}{\sin\theta} = \frac{\pi}{u} \qquad 2/13\,\pi \leqslant u \leqslant \pi \tag{25}$$

$$F(u) = 0 \qquad -\pi \leqslant u \leqslant 2/13\,\pi.$$

Considering an array of elements spaced $\lambda/2$ apart we obtain for the array expression

$$P(u) = \sum_{-N}^{N} A_n e^{jnu},$$

which is periodic for intervals of 2π. This implies that

$$P(\pi) = P(-\pi)$$

and thus the conditions given by equation (25) cannot be simultaneously satisfied at $u = \pm\pi$. The resulting pattern, using a Woodward synthesis, would compromise the two conditions and the signal would fall somewhere between unity and zero. This is shown in Fig. 4 by the broken line. The present difficulty can be easily removed by extending the synthesis interval into the invisible range. Thus if 15 elements are placed within the same space of 6λ as was formerly occupied by the 13 elements, the resulting inter-element spacing will be $[(13/15)\lambda/2]$ and the synthesis range or the interval of periodicity will extend to $u = \pm 15/13\,\pi$. The result is shown by the solid line of Fig. 4. $P_1(u)$ is given by

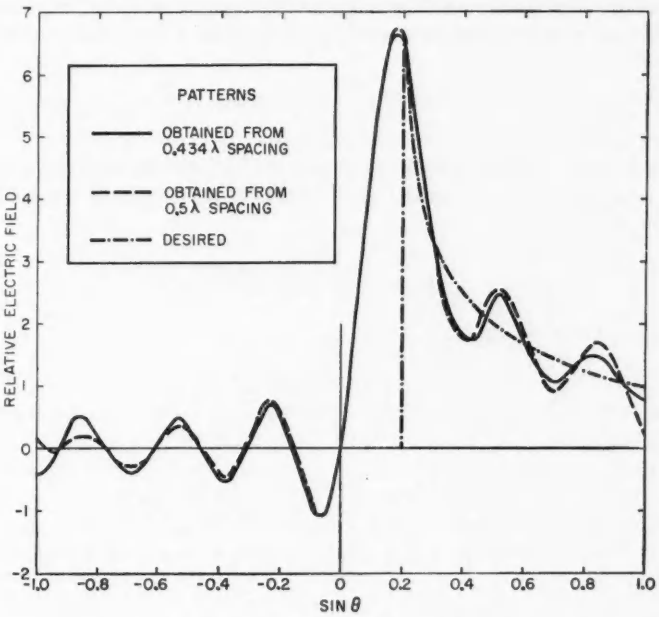

FIG. 4. A cosecant squared pattern obtained by a Woodward synthesis for a discrete array 6λ long. Comparison between the pattern resulting from λ/2 spacing and that resulting from an inter-element spacing .434λ.

$$P_1(u) = \sum_{n=1}^{7} \frac{1}{2n} \frac{\frac{13}{15}\sin\left[\frac{13}{2}\pi\left(u-\frac{2n}{13}\right)\right]}{\sin\left[\frac{13}{15}\cdot\frac{\pi}{2}\left(u-\frac{2n}{13}\right)\right]} \tag{26}$$

and $P_1(\pi) = 0.7961$; $P_1(-\pi) = 0.4221$. The value of $P_1(u)$ for $u = \pi$ is thus within approximately the same error as for the rest of the range, while the sidelobes in the zero signal range are below the same peak value. The modified pattern has somewhat smaller ripples near $u = \pi$; the reason being that the first zero signal point has been removed further from the non-zero portion of the pattern. The invisible range can thus serve as a region into which some of the difficulties of the visible range synthesis may be carried and settled. In the present example the change in reactive energy is negligible, however, a useful objective has been achieved by using a set of elements spaced somewhat less than $\lambda/2$ apart.

In the above example the continuous aperture excitation required to produce the pattern described by the solid line would have a non-vanishing pattern outside the visible range. The failure to notice it would produce a distorted pattern in the visible range if one would use the continuous excitation distri-

bution as the envelope for the discrete array. To emphasize the importance of checking the total pattern produced by a continuous distribution consider the following pattern,

$$F(u) = 0 \qquad -\pi \leqslant u \leqslant 0$$
$$= 1, \qquad 0 \leqslant u \leqslant \pi \tag{27}$$

which may be synthesized equally well by either a continuous aperture or a discrete array of elements spaced $\lambda/2$ apart. Computing the continuous excitations we obtain

$$g(p) = \frac{1}{2\pi}\int_0^{\pi} e^{-jpu}du = e^{j(\pi p/2)}\frac{\sin(p\pi/2)}{\pi p}. \tag{28}$$

The discrete array results in

$$A_n = e^{j(\pi n/2)}\frac{\sin(n\pi/2)}{n\pi}. \tag{29}$$

This approximation may be quite satisfactory except at $u = 0$ and $u = \pi$ due to Gibb's phenomenon.

The vicinity of $u = \pi$ may be easily adjusted in the continuous aperture by adjusting the excitation to extend the pattern into the invisible range similarly to the previous example. This would involve a change of the excitation which would be

$$g(p) = \frac{1}{2\pi}\int_0^{\alpha\pi} e^{-jpu}du = e^{(\alpha\pi p/2)}\frac{\sin(\alpha\pi p/2)}{\pi p} \tag{30}$$

where $1 < \alpha < 2$. If this excitation were used as an envelope for the discrete array we would obtain

$$A_n = e^{j(\alpha\pi n/2)}\frac{\sin\alpha\pi n}{\pi n}. \tag{31}$$

This excitation would result in the following pattern for a $\lambda/2$ spaced array

$$P(u) = \sum \frac{\sin\alpha\pi n}{\pi n}\cos n\left(u-\frac{\pi\alpha}{2}\right), \tag{32}$$

which would extend the main beam into the range of angles between $-\pi$ and zero:

$$P(u) = 1 \qquad -\pi \leqslant u \leqslant (\alpha-2)\pi$$
$$= 0 \qquad (\alpha-2)\pi \leqslant u \leqslant 0$$
$$= 1 \qquad 0 \leqslant u \leqslant \pi$$

In other words a beam of width $\alpha\pi$ is produced whose center is scanned to $u = \alpha\pi/2$. Thus a completely unacceptable pattern is produced unless one uses element spacing of $\lambda/2\alpha$. This obviously does not mean that an acceptable pattern cannot be obtained by means of an array of elements spaced $\lambda/2$ apart. It only means that in this case the continuous distribution cannot be

used as the envelope for the discrete array. The pattern has to be directly synthesized for the given array since the inter-element spacing was prespecified.

EQUIVALENCE THEOREM FOR TWO-DIMENSIONAL DISTRIBUTIONS

The one-dimensional derivation can be generalized to include two-dimensional planar apertures. We can represent the far field of a two-dimensional aperture by means of a transform (Silver 1949)

$$g(k_x,k_y) = \int_{-\infty}^{\infty}\int_{-\infty}^{\infty} F(\xi,\eta)e^{j(k_x\xi+k_y\eta)}d\xi d\eta \tag{33}$$

and

$$F(\xi,\eta) = \frac{1}{4\pi^2}\int_{-\infty}^{\infty}\int_{-\infty}^{\infty} g(k_x,k_y)e^{-j(k_x\xi+k_y\eta)}dk_x dk_y \tag{34}$$

where we shall measure the variable ξ and η in half wavelengths as before,

$$\xi = \frac{x}{\lambda/2}; \qquad \eta = \frac{y}{\lambda/2}$$

and

$$\begin{aligned} k_x &= \pi \sin\theta\cos\phi \\ k_y &= \pi \sin\theta\sin\phi. \end{aligned} \tag{35}$$

Here $g(k_x,k_y)$ is the desired pattern usually specified for the visible range alone, namely for $-\pi \leqslant k_x, k_y \leqslant \pi$. The conditions imposed on $g(k_x,k_y)$ are:

condition No. 1, $g(k_x,k_y)$ is of bounded variation as a function of k_x and k_y;
condition No. 2, $g(k_x,k_y) = 0$ for $|k_x,k_y| > \pi$.

The procedure for proving the equivalence between continuous distributions and discrete arrays is the same as in the one-dimensional case,* and will, therefore, not be repeated.

The error formula is likewise similar and is given by

$$E_d = \frac{1}{4\pi^2}\int_{-\pi}^{\pi}\int_{-\pi}^{\pi} |g(k_x k_y)|^2 dk_x dk_y - \sum_{m,n} |A_{mn}|^2 \tag{36}$$

where

$$A_{mn} = \frac{1}{4\pi^2}\int_{-\pi}^{\pi}\int_{-\pi}^{\pi} g(k_x k_y)e^{-jmk_x - jnk_y}dk_x dk_y.$$

CONCLUSIONS

We have shown that a discrete array can always be substituted for a continuous distribution in a plane, without changing the pattern significantly. This holds for both directive and shaped beams. The over-all dimensions of

*For details of obtaining a two-dimensional Fourier series representing a planar array, which is required for the derivation, see (Ksienski 1960).

the array are the same as that of the continuous distribution, and the excitation coefficients of the array are proportional to the continuous excitations. The spacing of the sources in the array are determined from the behavior of the pattern outside the visible range. Increasing the density of sources per unit length beyond the one indicated by the above considerations does not improve the resulting pattern. Certain minor differences in the pattern may occur, depending on the orientation of the elements in the array. Thus, for a given antenna dimension, a set of transverse slots would produce the effect of a somewhat longer and less directive array than a line source. This is evidenced by a somewhat narrower beam and higher sidelobes produced by the discrete array. For a set of longitudinal slots, however, these differences would be virtually eliminated.

ACKNOWLEDGMENTS

This work was sponsored by the Electronics Research Directorate of the Air Force Cambridge Research Center, Air Research and Development Command, under Contract AF 19(604)-3508. The author wishes to express his gratitude to Dr. L. L. Bailin for his helpful suggestions and continued interest in this work.

REFERENCES

COURANT, R. and HILBERT, D. 1953. Methods of mathematical physics (Interscience Publishers, New York), p. 52.
KSIENSKI, A. 1960. IRE Trans. **AP-8**, 224.
SILVER, S. 1949. Microwave antenna theory and design (McGraw-Hill Book Company, New York).
TAYLOR, T. T. 1953. One parameter family of line sources producing modified $\sin \pi u/\pi u$ patterns, Tech. Memo. No. 324, Hughes Aircraft Company, Culver City, California.
WOODWARD, P. M. and LAWSON, J. D. 1948. J. Inst. Elec. Engrs. **95** (III), 363.

APPENDIX

ERRORS IN APPROXIMATING A CONTINUOUS FINITE APERTURE BY A SMALLER APERTURE, DISCRETE OR CONTINUOUS*

We are interested in evaluating the mean square error that results when the pattern, $F(u)$, produced by a continuous linear aperture of finite length $2M$ is approximated by that produced by a continuous linear aperture of length $2N < 2M$. This is in contrast to the assumption made in the main text that the aperture size for obtaining $F(u)$ exactly is infinite. The present assumption results in $F(u)$ extending over an infinite range, the error being evaluated only over the visible range. The aperture distribution of the smaller aperture is identical with that of the larger but is merely chopped off at $\pm N$. Denote the aperture distribution as $g(p)$ where p is a normalized aperture variable and call the pattern from the shortened aperture $F_e(u)$. Then the mean square pattern error in the visible range is given by

$$(1a) \qquad E_e = \frac{1}{2\pi}\int_{-\pi}^{\pi} [F(u) - F_e(u)][F^*(u) - F_e^*(u)]\, du.$$

*Derived by Dr. A. T. Villeneuve, Hughes Aircraft Company, Culver City, California.

If the patterns are expressed in terms of their aperture distributions the error may be put into the following form

$$(2a) \qquad E_e = \int_{-M}^{M}\int_{-M}^{M} g(p)g^*(\zeta)\frac{\sin(p-\zeta)\pi}{(p-\zeta)\pi}\,dp\,d\zeta + \int_{-N}^{N}\int_{-N}^{N} g(p)g^*(\zeta)\frac{\sin(p-\zeta)\pi}{(p-\zeta)\pi}\,dp\,d\zeta - \int_{-N}^{N}\int_{-M}^{M}[g(p)g^*(\zeta)+g^*(p)g(\zeta)]\frac{\sin(p-\zeta)\pi}{(p-\zeta)\pi}\,dp\,d\zeta.$$

This may be written in a form as follows

$$(3a) \qquad E_e = \int\int_A g(p)g^*(\zeta)\frac{\sin(p-\zeta)\pi}{(p-\zeta)\pi}\,dA$$

where A is given by four squares of side $|M-N|$ in the (ζ,p) plane located at the four corners and inside the large square whose corner points are given by $(M, M; -M, M; -M, -M; M, -M)$.

If we attempt to approximate $F(u)$, the pattern from a continuous aperture of normalized length $2M$, with a discrete array of elements separated by $\alpha\lambda/2$ the resulting pattern will be periodic with period $2\pi/\alpha$ and will coincide with $F(u)$ in the interval $-\pi/\alpha < u < \pi/\alpha$. Call the periodic pattern $F_1(u)$. Then

$$(4a) \qquad F_1(u) = \sum_n a_n e^{jn\alpha u}.$$

The source distribution which gives rise to this may be written formally as

$$(5a) \qquad g_1(p) = \frac{1}{2\pi}\int_{-\infty}^{\infty} F_1(u)e^{-jpu}\,du = \frac{1}{2\pi}\int_{-\infty}^{\infty}\sum_n a_n e^{j(n\alpha u-pu)}\,du$$

$$= \sum_n a_n\delta(p-\alpha n).$$

This represents a discrete aperture distribution of point sources where in view of equation (4a) and the conditions preceding it,

$$(6a) \qquad a_n = \frac{\alpha}{2\pi}\int_{-\pi/\alpha}^{\pi/\alpha} F_1(u)e^{-jn\alpha u}\,du = \frac{\alpha}{2\pi}\int_{-\pi/\alpha}^{\pi/\alpha} F(u)e^{-jn\alpha u}\,du.$$

Due to the finite available aperture the number of discrete sources are limited to $2N+1$ where N is the largest integer in M/α. Therefore there will be an error in the resultant pattern. If the mean square error between $F(u)$ and the resultant pattern is computed one gets

$$(7a) \qquad E_e = \int_{-M}^{M}\int_{-M}^{M} g(p)g^*(\zeta)\frac{\sin(p-\zeta)\pi}{(p-\zeta)\pi}\,dp\,d\zeta + \sum_{-N}^{N}\sum_{-N}^{N} a_m a_n^*\frac{\sin\alpha(m-n)\pi}{\alpha(m-n)\pi} - \int_{-M}^{M}\sum_{-N}^{N}[g(p)a_n^*+g^*(p)a_n]\frac{\sin(p-\alpha n)\pi}{(p-\alpha n)\pi}\,dp.$$

DIPOLE-FIELD TYPE MAGNETIC DISTURBANCES AND AURORAL ACTIVITIES[1]

B. K. BHATTACHARYYA[2]

ABSTRACT

The characteristics of the magnetic field components at Agincourt have been calculated for a current system produced by an electric dipole located in the region of auroral activity near Ottawa. It is noted that, irrespective of the orientation of the dipole, the horizontal magnetic field component rotates in the clockwise and anticlockwise senses for motion of the dipole towards the east and the west respectively, when the dipole is situated in the north half of the sky as seen from the observing station.

Next, the magnetograms obtained at Agincourt have been studied at those times of the night when auroral activity was recorded in the all-sky camera photographs at Springhill near Ottawa. It is noted that the horizontal magnetic field describes a loop during a particular phase of auroral activity because of its gradual growth and decay. The distributions of clockwise and anticlockwise rotations with respect to local time are found to be very similar in many respects to those of auroral motions to the east and west respectively. The sense of rotation of the loop is predominantly anticlockwise in the early part of the night and clockwise in the late hours of the night.

It is found that eastward and westward orientations of the dipole are the most probable ones. The direction of movement and the initial location of the predominant auroral form in the sky are found to tally well with those of the dipole deduced from a study of the magnetograms.

It seems that there is a time sequence relationship between successive phases of auroral activity and changes of characteristics of the loops described by the horizontal magnetic field vector. The area of a loop and the maximum magnitude of the field vector in the loop appear to be related to the brightness and horizontal extent of the auroral forms.

INTRODUCTION

From the early days of research on auroral and geomagnetic phenomena, it has been known that the onset of auroral activity is very closely associated in time with the magnetic perturbations recorded on the surface of the earth. This has led many to investigate whether the current system responsible for magnetic perturbations is spatially coincident with the visible auroral forms in the sky or not. 'Polar elementary storms' which are practically always accompanied by aurora, were shown by Birkeland (Harang 1951) to be attributable to the field of an infinite linear current or to that of a fairly narrow sheet of current flowing in the upper atmosphere. Since then attempts have been made to correlate the location of the linear current and that of the auroral arc observable in the sky.

The lines of the field of force of an infinitely long current conductor are represented by a system of circles around the conductor and so the magnetic disturbance vector will be tangent to one of these circles passing through the place of observation. This fact can be utilized to determine the angle of elevation of the infinite linear current from the horizon by knowing the direction of

[1]Manuscript received November 22, 1960.
Contribution from the Division of Radio and Electrical Engineering, National Research Council, Ottawa.
Issued as N.R.C. No. 6129.
[2]National Research Council Postdoctorate Fellow.

the disturbance vector. Stagg and Paton (1939) have calculated for several cases the elevation γ of the auroral arc and the elevation θ of the line current. They found that the frequency of γ and θ lying on the same side of the magnetic vertical plane was five times that on the opposite side. The difference between θ and γ was less than 10 degrees in 35 per cent of the cases and less than 20 degrees in 60 per cent. A similar conclusion was reached by Heppner (1954) from his analysis of magnetic and auroral records at College, Alaska.

A study on the same lines was undertaken at Ottawa with the help of auroral all-sky camera photographs taken at Springhill (geographic 45.2° N., 75.5° W.; geomagnetic 56.5° N., 6.9° W.) and the magnetograms taken at Agincourt (geographic 43.8° N., 79.3° W.; geomagnetic 55° N., 11.6° W.). Since Springhill is about 230 miles northeast from Agincourt and the latitude separation is only 1.4°, it can reasonably be assumed that the effect of current associated with auroral forms observed at Springhill will be felt at Agincourt.

First the all-sky camera photographs are studied for the three months of March, April, and June, 1958, which cover the Spring equinoxial period when auroral activity was at its peak in that year. Some nights on which the sky condition was perfectly clear and the elevations of auroral arcs could be reasonably accurately measured, are chosen. Then the magnetic records on those nights are scaled at intervals of 15 minutes to obtain the values of the horizontal component H (positive northward), the declination D (positive eastward), and the vertical component Z (positive vertically downward) of the earth's magnetic field. With the help of the median values H_q, D_q, and Z_q of the 5-quiet-day values in the respective month, the deviations ΔH, ΔD, and ΔZ are calculated. ΔH and ΔD are then combined together trigonometrically to determine the disturbance horizontal magnetic field vector, H_d. H_d and ΔZ are used to find the disturbance field vector.

Though the preliminary calculations indicate the validity of the conclusion reached by Stagg and Paton on many occasions, there are, nevertheless, periods ranging from half an hour to several hours on every night studied when the perpendicular to the disturbance field vector points consistently deep into the south whereas auroral activity is confined within 45° of the northern horizon. A typical example is shown in Fig. 1 for a 5-hour period on the night of April 16, 1958. During this period arcs and rayed arcs, confined within 30° of the northern horizon, constituted the auroral activity. But from the H_d and ΔZ plots in Fig. 1, it is evident that the infinite 'line' current, if responsible for the perturbed magnetic field, was always in the southern part of the sky. If we take the effect of earth current into account and assume that twice the vertical component ΔZ and two-thirds of the horizontal component ΔH are of external origin, the position of the 'line' current is shifted still further to the south. The line current model of the magnetic disturbances does not therefore associate itself spatially with the visual auroral arc during a considerable length of time on every night at Springhill near Ottawa. Even when the locations of the line current and auroral arc are in the same part of the sky, they differ, in most of the cases, by quite an appreciable angle in elevation as was noted by Stagg and Paton.

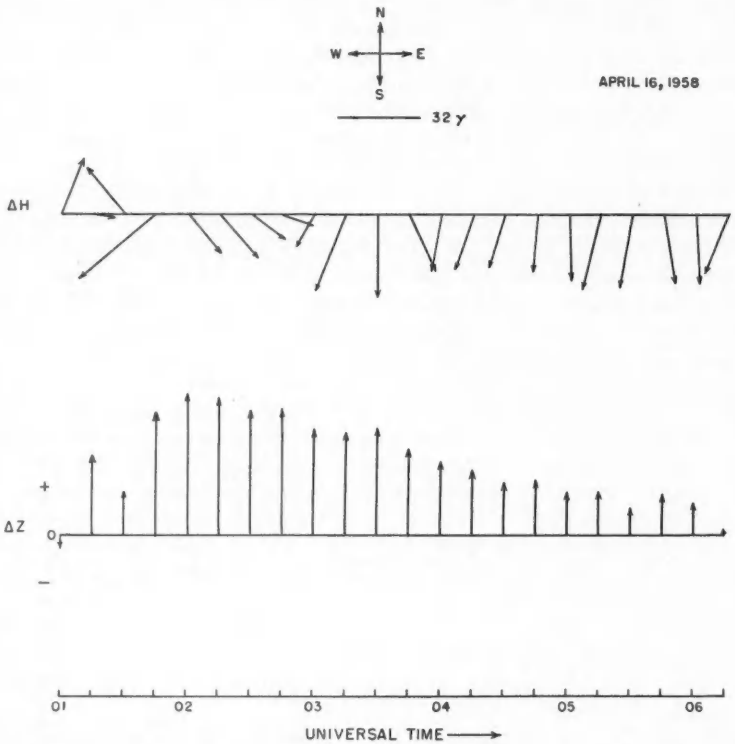

FIG. 1. Magnetic field disturbance vectors for a period of 5 hours on April 16, 1958.

In addition to what has been mentioned, there is another factor to be noted. Bands, draperies, glow, and such other forms which are limited in horizontal extent from the observational point of view, are sometimes the main constituents of auroral activity. During these periods, it does not seem reasonable to assume an infinite linear current or many such currents as representing the perturbed magnetic field.

Furthermore, if a series of vectors of the horizontal magnetic field component are plotted on a polar diagram, the position of the end of the vector rotates clockwise or anticlockwise and forms a loop during any active phase of auroral activity. The description of a loop by the horizontal component cannot be due only to the growth and decay of the intensity of the current system but must also result from some kind of movement or rotation of the current system as a whole. An infinite line current obviously cannot explain all the features of this characteristic of the magnetic field disturbance.

In recent years Nagata and Fukushima (1952) and Fukushima (1953) have shown that polar magnetic storms are composed of a number of elementary

disturbances which take place intermittently or successively with duration from a few tens of minutes to about 2 hours. It has been suggested that each elementary disturbance is caused by the production of an electromotive force in a rather small area of high ionization produced in the upper atmosphere over the auroral zone. The equivalent current system corresponding to each elementary disturbance is generally much simpler, being approximated by the current system produced by an electric dipole at the center of the highly ionized area.

The present study is undertaken to determine as far as practicable the suitability of representing the cause of the magnetic field disturbances by a current system due to an electric dipole spatially located in the region of brightest auroral activity. An explanation of the loop characteristics of the horizontal magnetic field disturbances will be attempted by assuming the movement of the electric dipole itself, i.e., of the small region of high conductivity. Since in the case of severe magnetic disturbances many elementary disturbances play their part successively one after another and sometimes simultaneously, it is very difficult to separate their individual effects and to analyze them one by one. In this paper, therefore, only those disturbances, which are not very complicated and are classified under small or medium range, have been studied. We have considered only the case when a single electric dipole is present in the sky.

MAGNETIC FIELD COMPONENTS OF AN OVERHEAD CURRENT SYSTEM DUE TO AN ELECTRIC DIPOLE

When an electric dipole directed to $\Lambda = 0$ is situated at the pole of a spherical co-ordinate system (Θ, Λ) of a conducting spherical surface, the current function J of the resulting electric current is given by (Fukushima 1953)

$$J(\Theta,\Lambda) = \frac{I_0\sigma_0}{2a} \cdot \frac{\sin\Theta \sin\Lambda}{1-\cos\Theta} \tag{1}$$

where a denotes the radius of the spherical surface of the ionosphere, I_0 the moment of the electric dipole, and σ_0 the electric conductivity of the spherical surface outside the dipole. This expression of the current function is valid everywhere except in the neighborhood of the region of high conductivity containing the dipole. Expressing (1) in terms of spherical harmonics, we have

$$J(\Theta,\Lambda) = \frac{I_0\sigma_0}{2a}\sum_{n=1}^{\infty}\frac{2n+1}{n(n+1)}P_{n,1}(\cos\Theta)\sin\Lambda \tag{2}$$

where $P_{n,1}$ is the associated Legendre function of the nth degree and of the first order. When the current function is expressed in terms of spherical functions, e.g., $J = \sum J_n(\Theta,\Lambda)$, the magnetic potential W at the point (r,Θ,Λ) is given by (Chapman and Bartles 1940)

$$W = -4\pi\sum_{n=0}^{\infty}\frac{n+1}{2n+1}J_n(\Theta,\Lambda)\left(\frac{r}{a}\right)^n \tag{3}$$

$$= -\frac{I_0\sigma_0}{2a}4\pi\sum_{n=1}^{\infty}\frac{1}{n}\left(\frac{r}{a}\right)^n P_{n,1}(\cos\Theta)\sin\Lambda \tag{4}$$

where r is inside the sphere of radius a and the current and current function are expressed in electromagnetic units.

The generating function of the Legendre polynomial is given by

$$\phi = \frac{1}{(1-2hx+h^2)^{1/2}} = \sum_{n=0}^{\infty} P_n(x)h^n \tag{5}$$

where $P_n(x)$ is the Legendre polynomial of the nth degree.

With the help of the relation

$$P_{n,1}(x) = (1-x^2)^{1/2}\frac{dP_n(x)}{dx} \tag{6}$$

we easily obtain

$$\sum_{n=1}^{\infty} h^{n-1}P_{n,1}(x) = (1-x^2)^{1/2}\cdot\frac{1}{(1-2hx+h^2)^{3/2}}. \tag{7}$$

Integrating both sides of (7) with respect to h from 0 to h, we have

$$\sum_{n=1}^{\infty}\frac{h^n}{n}P_{n,1}(x) = \frac{1}{(1-x^2)^{1/2}}\cdot\left[x+\frac{(h-x)}{(1-2hx+h^2)^{1/2}}\right]. \tag{8}$$

With the help of (4) and (8) we can express the magnetic potential W in the following form:

$$W = -4\pi\cdot\frac{I_0\sigma_0}{2a}\cdot\sin\Lambda\left[\frac{1}{(1-x^2)^{1/2}}\left\{x+\frac{(h-x)}{(1-2hx+h^2)^{1/2}}\right\}\right] \tag{9}$$

where $x = \cos\Theta$ and $h = r/a$.

We now introduce a new spherical co-ordinate system in which the axis passes through the geomagnetic poles. Let (θ,λ) be the co-latitude and longitude of the point of observation in the new system, and let (θ_0,λ_0) be corresponding co-ordinates for the position of the dipole. If the dipole be oriented geomagnetically eastward, the mutual relations between the two co-ordinate systems are

$$\begin{aligned}
\sin\Theta\cos\Lambda &= \sin\theta\sin(\lambda-\lambda_0),\\
\sin\Theta\sin\Lambda &= \cos\theta\sin\theta_0 - \sin\theta\cos\theta_0\cos(\lambda-\lambda_0),\\
\cos\Theta &= \cos\theta\cos\theta_0 + \sin\theta\sin\theta_0\cos(\lambda-\lambda_0).
\end{aligned} \tag{10}$$

If the dipole be oriented along a geomagnetic meridian towards the south, we have

$$\begin{aligned}
\sin\Theta\cos\Lambda &= \sin\theta\cos\theta_0\cos(\lambda-\lambda_0) - \cos\theta\sin\theta_0,\\
\sin\Theta\sin\Lambda &= \sin\theta\sin(\lambda-\lambda_0),\\
\cos\Theta &= \cos\theta\cos\theta_0 + \sin\theta\sin\theta_0\cos(\lambda-\lambda_0).
\end{aligned} \tag{11}$$

With the aid of (10) and (11) we can express (9) in terms of geomagnetic co-ordinates and then determine the northward, eastward, and vertically

downward components of the magnetic field in the usual way. The expressions of these components for a dipole oriented in the geomagnetically east direction are:

Northward component:

$$(12)\qquad X = \frac{\partial W}{r\partial\theta} = \frac{4\pi}{r}\cdot\frac{I_0\sigma_0}{2a}\cdot\left[-\frac{\sin\Lambda}{\sin\Theta}\left\{-\sin\theta\cos\theta_0+\cos\theta\sin\theta_0\cos(\lambda-\lambda_0)\right\}\cdot C+\{\sin\theta\sin\theta_0+\cos\theta\cos\theta_0\cos(\lambda-\lambda_0)\}\cdot B\right]$$

Eastward component:

$$(13)\qquad Y = -\frac{\partial W}{r\sin\theta\partial\lambda} = \frac{4\pi}{r}\cdot\frac{I_0\sigma_0}{2a}\left[-\frac{\sin\Lambda}{\sin\Theta}\sin\theta_0\sin(\lambda-\lambda_0)C+\cos\theta_0\sin(\lambda-\lambda_0)B\right].$$

Vertically downward component:

$$(14)\qquad Z = \frac{\partial W}{\partial r} = -\frac{4\pi}{r}\cdot\frac{I_0\sigma_0}{2a}\cdot\frac{h\sin\Lambda\sin\Theta}{(1-2h\cos\Theta+h^2)^{3/2}}\cdot$$

Similarly, for the dipole oriented to the south, we have

$$(15)\qquad X = \frac{4\pi}{r}\cdot\frac{I_0\sigma_0}{2a}\left[-\frac{\sin\Lambda}{\sin\Theta}\left\{-\sin\theta\cos\theta_0+\cos\theta\sin\theta_0\cos(\lambda-\lambda_0)\right\}\cdot C-\cos\theta\sin(\lambda-\lambda_0)\cdot B\right]$$

$$(16)\qquad Y = \frac{4\pi}{r}\cdot\frac{I_0\sigma_0}{2a}\left[-\frac{\sin\Lambda}{\sin\Theta}\sin\theta_0\sin(\lambda-\lambda_0)C+\cos(\lambda-\lambda_0)B\right]$$

$$(17)\qquad Z = -\frac{4\pi}{r}\cdot\frac{I_0\sigma_0}{2a}\cdot\frac{h\sin\Lambda\sin\Theta}{(1-2hx+h^2)^{3/2}}$$

where

$$B = \frac{1}{(1-x^2)}\cdot\left\{x+\frac{h-x}{(1-2hx+h^2)^{1/2}}\right\}$$

and

$$C = \left\{1+\frac{hx-1}{(1-2hx+h^2)^{3/2}}\right\}+\frac{2x}{(1-x^2)}\left\{x+\frac{h-x}{(1-2hx+h^2)^{1/2}}\right\}.$$

In equations (12)–(17), the trigonometrical functions of Λ and Θ are used for the sake of writing simplicity. The first two equations in both cases of dipole orientation are for geomagnetic north and east components respectively. They can be easily manipulated to calculate the expressions for the geographic north and east components. Then these latter components are combined to

yield the horizontal field component H and the declination D. In Fig. 2 are plotted the expressions for $(ar/2\pi I_0\sigma_0)H$ (solid lines) and $(ar/2\pi I_0\sigma_0)Z$ (dotted lines) as a function of various locations and two different orientations (geomagnetic east and south respectively) of the electric dipole taking the

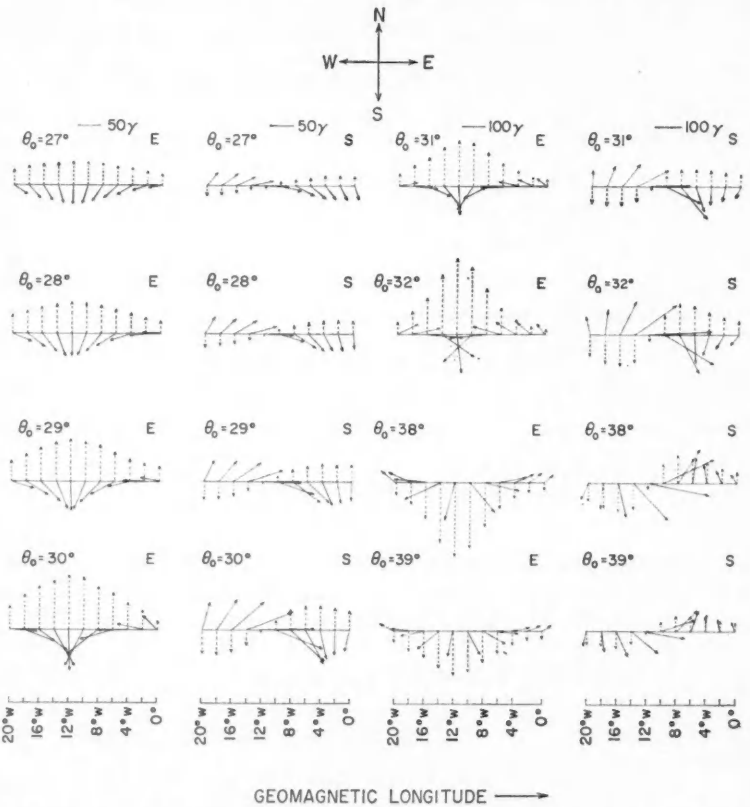

FIG. 2. A plot of the theoretical magnetic field components at Agincourt as a function of various locations of the electric dipole and for two different dipole orientations marked E (geomagnetic east) and S (geomagnetic south) respectively. At the top of the figure N, E, S, and W stand for the four cardinal directions, the geographic north, east, south, and west respectively. The solid lines indicate $(ar/2\pi I_0\sigma_0)H$ and the dotted lines $(ar/2\pi I_0\sigma_0)Z$.

observing station at Agincourt ($\theta = 35°$ and $\lambda = 348.4°$ E.). The dipole is assumed to be at a height of 100 km from the surface of the earth.

From the expressions of the magnetic field components for two perpendicular orientations of the dipole, it is quite easy to obtain their values for any other dipole orientation, whatsoever. For example, if the dipole be oriented westward, the directions of H and Z will be opposite to those in the case of east

orientation. For a dipole pointing at an angle with the geomagnetic east, the values in cases of south and east orientations will have to be combined vectorially to obtain the field components.

A study of Fig. 2 reveals some very interesting facts. The horizontal component is found to rotate either clockwise or anticlockwise as the dipole moves. The direction of the rotation depends upon the location of the dipole and the direction to which it is moving. In the following table are summarized the various possible cases for specific sense of rotation of H.

Sense of rotation of H	Direction of movement of the dipole	Location of the dipole	Orientation of the dipole
(i) Clockwise	East	North of the parallel of latitude through Agincourt	All possible
	West	South of the parallel of latitude through Agincourt	All possible
	North	West of the geomagnetic meridian through Agincourt	All possible
	South	East of the geomagnetic meridian through Agincourt	All possible
(ii) Anticlockwise	West	North of the parallel of latitude through Agincourt	All possible
	East	South of the parallel of latitude through Agincourt	All possible
	South	West of the geomagnetic meridian through Agincourt	All possible
	North	East of the geomagnetic meridian through Agincourt	All possible

Aurora is usually observed in the northern sky at Springhill except for very disturbed days. Since Agincourt is only 1.5° south of Springhill, these aurorae will also be on the same part of the sky at Agincourt. Auroral motion is predominantly in the geomagnetic east–west direction, though a small north–south component of motion is always present (Kim and Currie 1958; Bhattacharyya 1960). There are some cases when the motion is mainly in the north–south direction. If the region of high conductivity in the upper atmosphere which contains the electric dipole be spatially coincident with the brightest and most active auroral form seen in the sky, the dipole will also move in most cases along the geomagnetic east or west direction. Consequently the horizontal field component due to current system of the dipole will rotate either in clockwise or anticlockwise sense and will eventually form a loop because of the gradual growth and decay of the intensity of the current system.

It is, indeed, difficult and susceptible to error to predict the motion of the dipole from the sense of rotation of the horizontal field component. Nevertheless, by noting the sense of rotation and the mean direction of H and the variation of the vertical field component it is often possible to deduce the direction of motion, orientation and location of the dipole and to associate it with the important auroral form in the sky as recorded in the all-sky camera photograph at that time.

CHARACTERISTICS OF THE LOOP FORMED BY THE HORIZONTAL FIELD VECTOR DIAGRAM

In the previous section we have already discussed the reason why the vector diagram of the horizontal magnetic field component due to an electric dipole whose moment increases up to a peak value and then decreases in a gradual fashion with time, will form a loop. The sense of rotation of the horizontal disturbance vector will depend upon the location and, most important of all, the direction of motion of the dipole.

In this section we shall study the characteristics of these loops formed on those nights when aurora was recorded on the all-sky camera at Springhill during the months of March, April, and June, 1958. The magnetograms used for this purpose were obtained from Agincourt and only small and moderate intensity disturbances were analyzed.

Generally, the magnetic activity follows the auroral activity. The latter undergoes a cycle of changes in its form, illumination, spread, and motion. Any particular period during which one specific form builds up to its full grandeur and then decays gradually due to diffusion, de-excitation, and a host of other factors, may be called a phase of auroral activity. It should be noted that a phase does not in general consist of one specific form but several different forms and that it may not be isolated in time, i.e., before one phase has died down, one or more other phases may start. Due to this overlapping of phases, the loop described by the horizontal disturbing force will, in general, not be complete. So it is normally expected that before a particular vector diagram has reached even less than the half-way mark in its decay, a new phase will start. This tallies with what is actually observed.

Since the duration of a phase, and hence that of a loop, ranges from a few tens of minutes to 2 hours, we have scaled the magnetograms normally at every 5- or 10-minute interval. The vector diagrams for the horizontal component of the magnetic field are plotted in Figs. 3 and 4 for selected periods of high auroral activity. It is evident from the plots that the individual loops can be identified, though they are not necessarily isolated from other loops. The period of a particular loop can also be determined from the plots without difficulty.

Next, the time at which the horizontal field vector in a particular loop reaches its maximum, is noted and thus the distributions of clockwise and anticlockwise rotations of loops with respect to time are obtained. The distributions are shown in Fig. 5. The number of anticlockwise rotations is quite high in the early evening and assumes peak values during the intervals 0100–0200 and 0400–0500 U.T. After local midnight, the number begins to decrease gradually. In the case of clockwise rotations, the number begins to increase from about 0100 U.T., reaches its peak value in the interval 0700–0800 U.T., and then begins to decrease. After 0700 U.T., the number of clockwise rotations far exceeds that of anticlockwise rotations.

It is clear from Fig. 5 that the sense of rotation of the loop is predominantly anticlockwise in the early part of the night and clockwise in the late hours of the night. The reversal of the sense of rotation from anticlockwise to clockwise

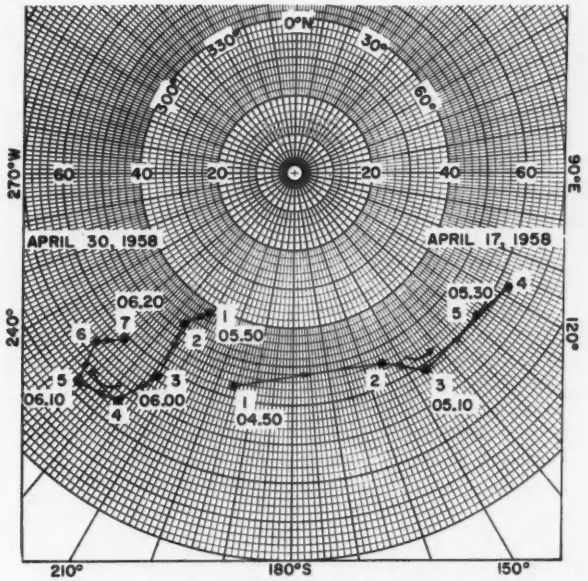

FIG. 3. Vector diagrams of the horizontal magnetic field component during specific intervals on April 17 and April 30, 1958. The field strength in gammas has been plotted against azimuth measured eastward from geographic north. The time for each vector is given in U.T.

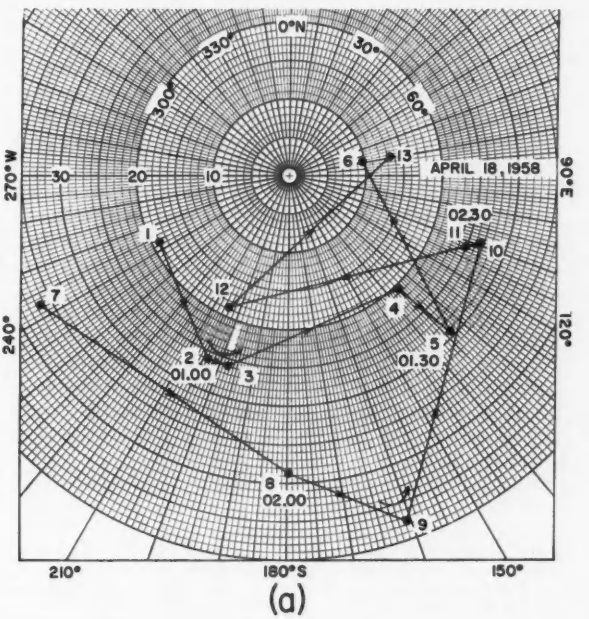

FIG. 4

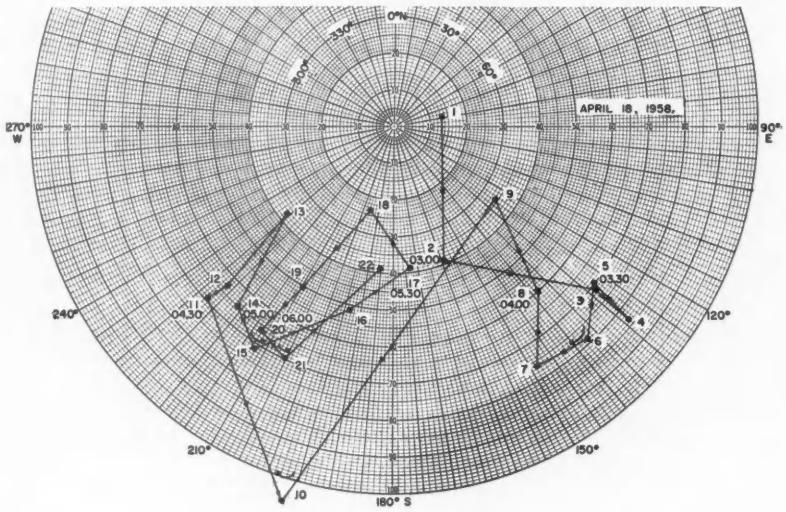

(b)

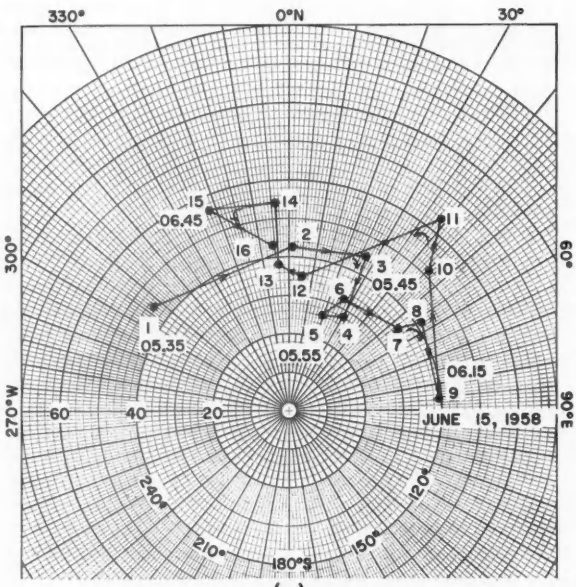

(c)

FIG. 4. Vector diagrams of the horizontal magnetic field component during specific intervals on April 18 and June 15, 1958. The field strength in gammas has been plotted against azimuth measured eastward from geographic north. The time for each vector is given in U.T.

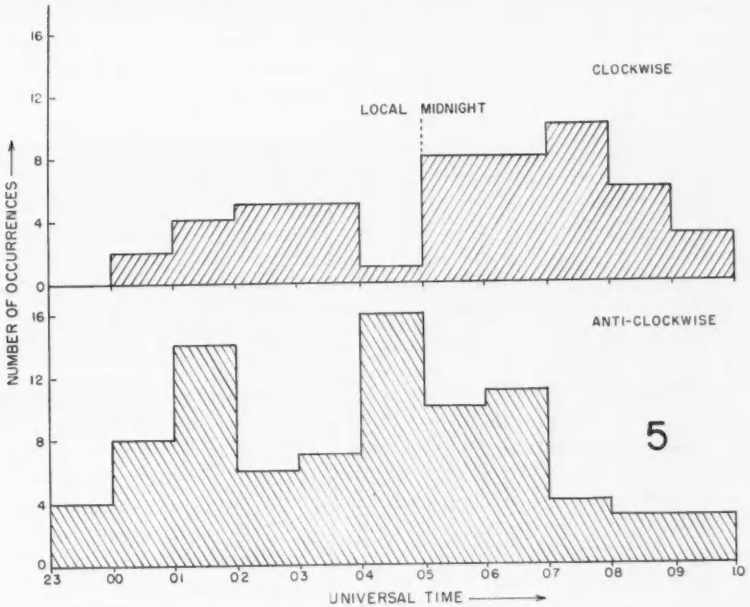

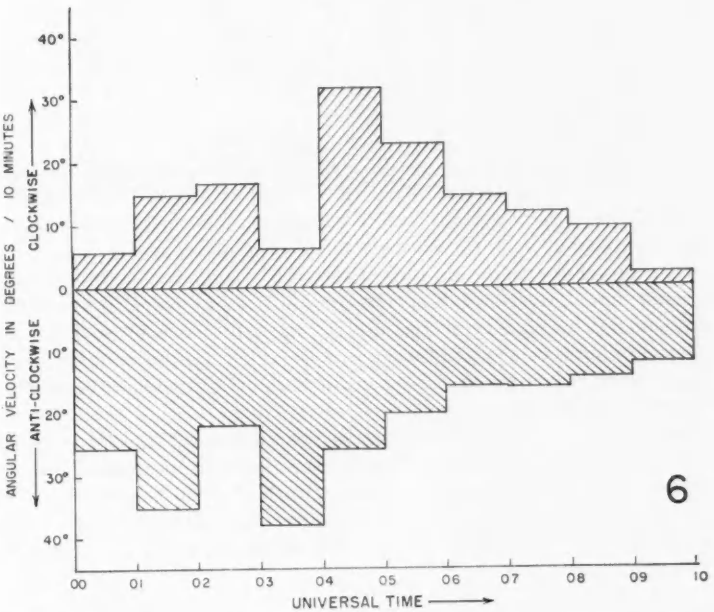

FIG. 5. Distribution of clockwise and anticlockwise rotations of the horizontal magnetic field component with respect to the time of the night.

FIG. 6. Distribution of the mean angular velocity of the horizontal magnetic field component in degrees per 10 minutes with respect to the time of the night.

seems to be a systematic process, occurring at a time very close to local midnight. The distributions of clockwise and anticlockwise rotations with respect to local time follow quite closely in characteristics the distributions of auroral motions to the east and the west respectively (Kim and Currie 1958; Bhattacharyya 1960), though the times of the peaks of the distributions do not coincide exactly. This is to be expected because, as mentioned earlier, the east–west component of auroral motion is always accompanied by a normally small north–south component. There are a few cases when the latter is quite predominant. We have not made any attempt to separate the east–west component of motion from the north–south one. This is the reason why the effect of the north–south component of auroral motion will be somewhat reflected in Fig. 5. It seems that most of the cases of clockwise rotations before 0400 U.T. are due to southward progress of auroral forms located to the east of the geomagnetic meridian passing through Agincourt.

From the disturbing force vectors at times just before and after the time of occurrence of the maximum horizontal field vector in a particular loop, the mean angular velocity of the rotation of the vector for all loops in a particular hour is calculated. The mean angular velocity is plotted in Fig. 6 as a function of universal time. It is found that the angular velocity is maximum within approximately the interval 0300–0400 U.T. for anticlockwise rotation and within 0400–0500 U.T. for clockwise rotation. We note (Bhattacharyya 1960) that the approximate time interval is 0200–0300 U.T. for the occurrence of maximum speeds in the case of auroral motion to the west and 0300–0400 U.T. for that to the east. It seems that the angular velocity of the field vector describing the loop lags somewhat behind the corresponding auroral motion either in the eastward or westward direction. After midnight, the angular velocities in both the curves of Fig. 6 are gradually decreasing.

AURORAL MOTIONS AND MOTIONS OF THE CURRENT SYSTEM

Let us now attempt to deduce the direction of motion, orientation and location of the dipole by comparing the sense of rotation of the horizontal field vector and the nature of variation of the corresponding vertical field component observed at Agincourt with the relevant theoretical curves in Fig. 2.

The distribution of orientation thus obtained is as follows: 50 cases of eastward orientation, 32 westward, 8 northward, and 18 southward. It seems that eastward and westward orientations are the most probable ones. Strangely, no relationship between the orientation and direction of motion of the dipole has been noticed. As an example, an eastward-oriented dipole has been found to move in practically all directions.

It is encouraging to note that at most of the times when auroral motion is clearly detectable, the direction of movement and initial location of the predominant auroral form in the sky tally well with those of the dipole. Three examples are described in the following table. In Figs. 3, 4, and 7 are shown the horizontal field vector diagrams and the all-sky camera photographs for three nights in April, 1958.

PLATE I

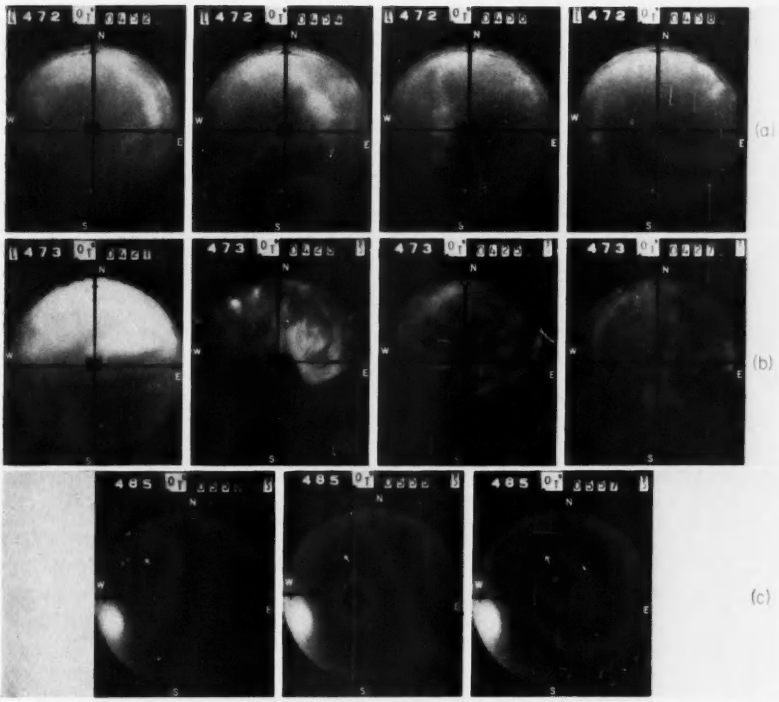

FIG. 7. All-sky camera photographs taken at Springhill on the nights of April 17, 18, and 30, 1958. The serial day number appears at the upper left of each photograph and the U.T., in hours and minutes, at upper right.

Date and time interval	Sense of rotation of the loop	Characteristics in the variation of Z	Possible dipole orientation and location	Characteristics of auroral motion
(1) April 17, 1958 0450–0520 U.T.	Anticlockwise; H always negative and minimum at 0510 U.T.	Z always positive; maximum at 0510 U.T.	East-oriented dipole; moving westward; initial location N.E. of Agincourt	An auroral band moving westward from N E. horizon to western horizon
(2) April 18, 1958 0410–0450 U.T.	Clockwise; H negative and minimum at 0420 U.T.	Z always positive and maximum at 0430 U.T.	South-oriented dipole; moving south; location east of Agincourt	Auroral curtain mainly located in the east; moving towards south
(3) April 30, 1958 0500–0645 U.T.	Clockwise; H negative and minimum at 0610 U.T.	Z always negative; minimum at 0610 U.T.	West-oriented dipole; moving east; location N.W. of Agincourt	Auroral patches mainly located in the N.W.; moving towards east

A study of cases like those given in the above table suggests that there is a good possibility of the highly conducting region being coincident with the moving auroral forms.

AURORAL ACTIVITY AND CHARACTERISTICS OF THE HORIZONTAL FIELD VECTOR DIAGRAM

Previously we have discussed to some extent the various phases of auroral activity which range in period from a few minutes to half an hour or more. The durations of successive loops formed by the horizontal field vector also vary within the same range. Some sort of relation may then be reasonably expected between the different phases of auroral activity and the corresponding loops of the horizontal magnetic field. With this in mind, auroral activity is studied on different nights from all-sky camera records and compared with the diagrams of the horizontal field vector. It is, indeed, noticed that (*a*) most of the loops are associated with particular phases of auroral activity; (*b*) the width and extent of a loop increase with the intensity of illumination, horizontal extent, and movement of the particular forms taking part in the corresponding phase of auroral activity; (*c*) the overlapping loops are observed when the decay of one phase and the growth of the succeeding phase are not separated by an interval of time.

Different phases of auroral activity on two nights are described below and the corresponding horizontal field vector diagrams are shown in Fig. 4.

The following examples definitely indicate a time sequence relationship between auroral activity and characteristics of the loop described by the horizontal field vector. The area and maximum magnitude of the loop seem to have a connection with the brightness and horizontal extent of the auroral forms.

Date and time interval	Sense of rotation of the loop	Characteristics in the variation of Z	Possible dipole orientation and location	Characteristics of auroral motion
(1) April 17, 1958 0450–0520 U.T.	Anticlockwise; H always negative and minimum at 0510 U.T.	Z always positive; maximum at 0510 U.T.	East-oriented dipole; moving westward; initial location N.E. of Agincourt	An auroral band moving westward from N E. horizon to western horizon
(2) April 18, 1958 0410–0450 U.T.	Clockwise; H negative and minimum at 0420 U.T.	Z always positive and maximum at 0430 U.T.	South-oriented dipole; moving south; location east of Agincourt	Auroral curtain mainly located in the east; moving towards south
(3) April 30, 1958 0500–0645 U.T.	Clockwise; H negative and minimum at 0610 U.T.	Z always negative; minimum at 0610 U.T.	West-oriented dipole; moving east; location N.W. of Agincourt	Auroral patches mainly located in the N.W.; moving towards east

A study of cases like those given in the above table suggests that there is a good possibility of the highly conducting region being coincident with the moving auroral forms.

AURORAL ACTIVITY AND CHARACTERISTICS OF THE HORIZONTAL FIELD VECTOR DIAGRAM

Previously we have discussed to some extent the various phases of auroral activity which range in period from a few minutes to half an hour or more. The durations of successive loops formed by the horizontal field vector also vary within the same range. Some sort of relation may then be reasonably expected between the different phases of auroral activity and the corresponding loops of the horizontal magnetic field. With this in mind, auroral activity is studied on different nights from all-sky camera records and compared with the diagrams of the horizontal field vector. It is, indeed, noticed that (*a*) most of the loops are associated with particular phases of auroral activity; (*b*) the width and extent of a loop increase with the intensity of illumination, horizontal extent, and movement of the particular forms taking part in the corresponding phase of auroral activity; (*c*) the overlapping loops are observed when the decay of one phase and the growth of the succeeding phase are not separated by an interval of time.

Different phases of auroral activity on two nights are described below and the corresponding horizontal field vector diagrams are shown in Fig. 4.

The following examples definitely indicate a time sequence relationship between auroral activity and characteristics of the loop described by the horizontal field vector. The area and maximum magnitude of the loop seem to have a connection with the brightness and horizontal extent of the auroral forms.

Auroral activity	Characteristics of loops
(*a*) April 18, 1958	
From 0107 rays and arcs are visible in the northern sky. At 0112 rays become very bright. At 0121 they have been transformed into glow and arc which begin to decrease in intensity rapidly after 0126. They regain their intensity of illumination after 0136 and break up into separate glows and bands at 0140. At 0145 homogeneous glow covers the whole northern sky right up to zenith, spreads southward, and thus becomes diffused.	Anticlockwise rotation of a loop from 0050 to 0140. The horizontal field vector is maximum at 0130.
At 0153 a band appears in the N.E. part of the sky, growing in intensity and moving westward. At 0156 several bands and glows cover the northern sky up to zenith. At 0212 glows, bands, rays, and arcs fill up the sky up to 35° S. of zenith. This activity begins to recede towards the north at 0216 and diminishes in intensity.	Anticlockwise rotation of a loop from 0150 to 0230. The horizontal field vector is maximum at 0210.
At 0221 new bands and arcs appear and extend up to 15° S. of zenith. The spread is maximum −45° south of zenith at 0237.	
At 0330 several auroral forms are visible up to 32° south of zenith, become very bright, and stay up to 0348. From 0349 separate bright bands and glows appear in the north and are later transformed into glow and homogeneous arcs confined to the northern sky practically up to zenith.	Clockwise rotation of a loop from 0330 to 0410. The horizontal field vector is maximum at 0340.
At 0421 a very intense band is formed in the northeast, moving towards southwest, becoming brightest at 0423, and breaking up at 0427. This activity subsides down to a great extent at 0439.	Clockwise rotation of a loop from 0410 to 0440. The horizontal field vector is maximum at 0420. Note the high magnitude of the field vector at maximum.
At 0446 two quite bright bands are growing in intensity, one in the eastern horizon and the other in the northwest sector of the sky. The former is moving towards the west and spreading in the north–south direction at 0450 whereas the latter is moving towards the south and also spreading in the north–south direction. At 0454 the former is very bright and extends from the northern horizon to 60° south of zenith through the zenith. It gains in intensity and spreads with time. At 0504 it is decreasing in brightness and has broken up into two parts. At 0514 quite bright auroral forms are again observed in the N.W., N.E., and S.W. sectors of the sky, moving north at 0516. At 0530 there is no trace of this auroral activity.	Anticlockwise rotation of a loop from 0440 to 0530. The horizontal field vector is maximum at 0510.
Cloudy intervals.	
At 0552 auroral activity is again building up in the whole northern sector of the sky up to zenith. Auroral forms are found to move to the north and are reduced to a narrow arc in the northern horizon at 0600. At 0608 a few bright patches and bands appear in the north. They are transformed later into a bright glow which stays up to 0626.	Anticlockwise rotation of a loop from 0540 to 0620. The horizontal field vector is maximum at 0610.
(*b*) June 15, 1958	
Up to 0530 patches of cloud prevented observation.	
At 0540 auroral forms such as arcs, glows, and bands are observable in the sky up to 55° S. of zenith and quite active up to 0550.	Clockwise rotation of a loop from 0535 to 0550. The horizontal field vector is maximum at 0545.

Auroral activity	Characteristics of loops
At 0554 auroral activity is concentrated mainly near the zenith and consists of a very bright band and a faint glow to the north. At 0556 the band has moved slightly to the north and at 0558 has broken up into two segments, one near eastern horizon and the other near western horizon of the sky. At 0600 the segment in S.E. sector of the sky becomes prominent, continues to move toward N.W. through zenith, and begins to decay in intensity. At 0608 another band appears near zenith in N.W. sector, moving to S.E., expanding, and getting diffused. This exists up to 0616.	Clockwise rotation of a loop from 0555 to 0615. The horizontal field vector is maximum at 0610.
At 0618 arcs and glows are observed in the north. At 0620 a part of an arc is transformed into a bright band extending from about 60° above the northern horizon to zenith. It is getting diffused from 0622 and vanishes at 0630 leaving only diffuse glow and arc in the north.	Anticlockwise rotation of a loop from 0615 to 0630. The horizontal field vector is maximum at 0625.
From 0632 another band is growing in intensity near the zenith. It proceeds gradually towards the south and extends up to 38° S. of zenith at 0642. After 0642 it begins to break up and becomes diffused. At 0650 there is no trace of the band.	Anticlockwise rotation of a loop from 0635 to 0650. The horizontal field vector is maximum at 0645.
Cloudy intervals.	

SUMMARY AND DISCUSSION

In this paper are presented the results of an attempt to represent the magnetic field perturbations associated with aurorae by a dipole field. It has been shown that the clockwise and anticlockwise senses of rotation of the horizontal magnetic field vector can be explained by assuming the region of high conductivity containing the dipole to be coincident in space and moving along with the predominant auroral form in the sky.

The electric dipoles are found to be oriented in all directions, though they seem to prefer the eastward or westward directions to the others. These orientations do not appear to be related to the directions of velocities and so it does not seem likely that they are produced by a dynamo action of the highly ionized area, as suggested by Nagata and Fukushima (1952) and Fukushima (1953). Furthermore, for the dynamo action to be valid we have to invoke a close connection between the wind motion of the upper atmosphere and auroral motion. But normally auroral forms move with a very high velocity with respect to the ionospheric wind motion and this does not tend to justify any general relation between them.

The assumption of a single dipole may not hold good on many occasions when there are several auroral forms simultaneously active in the sky. This is the reason why severe magnetic disturbances have not been analyzed in our study. In the case of disturbances of small or moderate intensity, the presence of a single dipole seems to be able to explain most of our observations. If there are several dipoles simultaneously active but moving in the same direction, the horizontal magnetic field will rotate in the same sense as in the case of a single dipole. Hence the distributions of clockwise and anticlockwise rotations with universal time (Fig. 5) need not be modified. However, in cases when these

conditions are not satisfied, it is not at all simple to predict the locations and directions of movement of a number of dipoles by comparing observational curves with theoretical ones.

It has been noticed in this study that magnetic perturbations are normally associated with a display of rays, draperies, and other active forms. They are very rarely detected when there is only a quiet homogeneous arc in the vicinity of the northern horizon. These observations may be explained by the discharge theory of aurora (Reid 1958) which states that at the base of the *E*-layer of the ionosphere, there will be very little extra ionization associated with homogeneous arcs but large amounts of ionization with the onset of an active display of rays, draperies, pulsating and flaming aurorae.

Recently, Weaver and Skinner (1960) have derived the current systems induced by dynamo action in a sheet of partially ionized gas surrounding an elliptical region of greater ionization density and have applied the results to conditions existing in the ionosphere in the presence of a long, homogeneous auroral arc. It has been shown that in the case of a long arc, a line current whose magnitude is linearly dependent on the height-integrated Cowling conductivity within the arc, can account for the observed magnitude of the disturbed magnetic field. A line current model has also been used by Bless *et al.* (1959) to explain the magnitude of the bay-type disturbances associated with aurora. Though a line current may, in some cases, be quite a reasonable model just for estimating the magnitude of the magnetic field disturbances, it cannot explain, as noted in this study, the clockwise or anticlockwise rotation of the magnetic field vector. Also in cases of auroral forms, limited in horizontal extent, the assumption of a line current model seems hardly to be justified. It appears, therefore, that a dipole model is, in general, preferable to a line current model for a correlation study of the different characteristics of the magnetic field disturbances and of the successive phases of accompanying aurora.

ACKNOWLEDGMENTS

The author is deeply indebted to Dr. A. G. McNamara for many helpful discussions and suggestions. He is also thankful to Dr. P. M. Millman and Dr. B. A. McIntosh for their help in the preparation of the manuscript.

The author takes this opportunity to record his grateful thanks to Mr. R. G. Madill of the Dominion Observatory at Ottawa for supplying him with the magnetograms of Agincourt.

REFERENCES

BHATTACHARYYA, B. K. 1960. Can. J. Phys. **38**, 1279.
BLESS, R. C., GARTLEIN, C. W., KIMBALL, D. S., and SPRAGUE, G. 1959. J. Geophys. Research, **64**, 949.
CHAPMAN, S. and BARTELS, J. 1940. Geomagnetism, Vol. 2 (Oxford University Press).
FUKUSHIMA, N. 1953. J. Fac. Sci. Univ. Tokyo, Sect. II, Vol. **8**, Part V, 293.
HARANG, L. 1951. The aurorae (Chapman & Hall Ltd.).
HEPPNER, J. P. 1954. Ph.D. Dissertation, California Institute of Technology, Pasadena, California.
KIM, J. S. and CURRIE, B. W. 1958. Can. J. Phys. **36**, 160.
NAGATA, T. and FUKUSHIMA, N. 1952. Rept. Ionosphere Research Japan, **6**, 85.
REID, G. C. 1958. Geophysical Research Rept. No. 4, University of Alaska, College, Alaska.
STAGG, J. M. and PATON, J. 1939. Nature, **143**, 941.
WEAVER, J. T. and SKINNER, R. 1960. Can. J. Phys. **38**, 1089, 1104.

NOTES

TYPICAL FAILURES IN PULSED FIELD MAGNET COILS*

RICHARD STEVENSON

A pulsed field magnet capable of producing fields in the megagauss range has been used here for some time. It appears worth while to describe, in the light of our experience, some of the factors which affect its successful operation.

The magnet itself is patterned after the type built at the M.I.T. Lincoln Laboratory (Foner and Kolm 1956). Energy is supplied to the magnet from a 2000-μf bank of 3000-v capacitors. The capacitors are charged by a separate power supply, and discharged into the magnet coil by means of an electrical spark. The maximum energy available from the capacitor bank is 10,000 joules; a field of 500,000 gauss can be produced with about 2600 joules in a solenoid (described below) of a 3/16 in. inner diameter.

The basic element of the magnet is a flat helical solenoid machined from a rod of beryllium copper with a parting tool, and heat-treated. The standard designs used here are described in Table I. In the assembly of the coil, adjacent

TABLE I

Inner diameter (in.)	Outer diameter (in.)	No. of turns	Thickness of turn	Approximate useful maximum field
3/8	1½	10	.060	300,000
1/4	1	10	.060	550,000
3/16	1	10	.060	750,000

turns are separated from each other by washers of shock resistant impregnated teflon or of Fiberglas impregnated with teflon. Our experience is that the reinforced teflon is superior to mica insulation for this purpose, and far more convenient.

The magnetic forces which act on the coils are of two types. There is a radial force tending to increase the inner diameter, which is a maximum at the center. Also there is an axial force which tends to warp inwards the innermost portion of each turn (Furth and Waniek 1956). These forces are resisted by the mechanical strength of the conductor. Photographs of a coil which has failed under these circumstances are given in Figs. 1 and 2. This coil was subjected to approximately a megagauss; at the center, the inner diameter was doubled, and the turns were fractured at each end. The failure is, of course, explosive, and apparatus placed in the solenoid is destroyed or severely damaged.

*Supported by the Office of Naval Research and in part by the Defence Research Board (Canada).

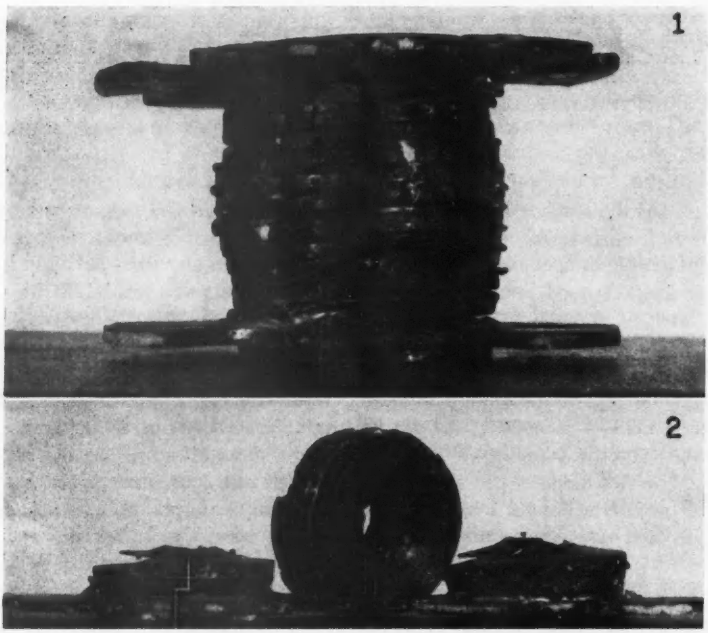

FIG. 1. Notice the bulging of the sides which is characteristic of a failure at very high fields.
FIG. 2. This is the same coil as in Fig. 1. The inner diameter has doubled, and the originally flat turns have been warped inward. The force of the field has also fractured the coil symmetrically.

This type of failure always occurs when the magnetic field goes beyond 700,000 to 800,000 oersteds. Careful heat treating will increase the maximum field slightly, but eventual failure is inevitable.

An entirely different type of failure is characteristic of lower field operation. The inner diameter of our magnet coil is covered carefully with a ceramic cement, which then is molded with a paper straw. The ceramic–straw assembly is allowed to harden for several days. In an experiment the maximum field is varied over a wide range. We find that eventually small bulging flaws appear on this inner coating. Shortly after the appearance of these flaws the magnet will explode, even at rather low fields.

Figure 3 is a photograph of a coil which has failed in this manner. The metal of this coil retained its mechanical strength. (Continued application of the high fields appears to anneal the beryllium–copper, even though the heating effect is negligible. This in itself appears to set a limit on the lifetime of a coil.) The failure seems to be due to sparking, which has cut a slot in the metal of about 2 mm deep and $\frac{1}{2}$ mm wide running in a line from turn to turn from the center to one end.

It is believed that this type of failure is due to a small flaw in the coil, perhaps a tool mark on the inner diameter. When the magnetic field is applied,

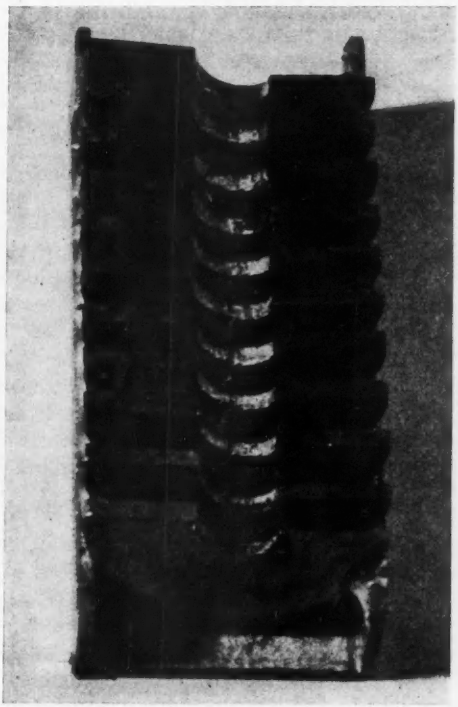

FIG. 3. This photograph gives a view of a coil which has failed at relatively low fields. The failure is probably due to a tool mark on the inner diameter. Careful surface preparation of the coil after heat treatment gives an improvement in the lifetime.

presumably a stress concentration appears at the flaw. This would try to relieve itself by propagating a crack radially. This in turn would cause a large voltage gradient at the end of the crack, and a spark could occur which would damage the insulation and would flaw the adjacent turn. The cracking–sparking effect is cumulative and the flaw runs to the end of the coil.

Careful attention to the machining and surface preparation seems to improve the life of the coils. A good coil can withstand several hundred pulses, although others will fail almost immediately. The lifetime of a coil is roughly inversely proportional to the highest field at which it is used. All coils fail eventually, and it is wise to use a fresh coil when starting an experiment.

FONER, S. and KOLM, H. H. 1956. Rev. Sci. Instr. **27**, 547.
——— 1956. M.I.T. Lincoln Laboratory Group Report M35, 67.
FURTH, H. P. and WANIEK, R. W. 1956. Rev. Sci. Instr. **27**, 195.

RECEIVED SEPTEMBER 12, 1960.
EATON ELECTRONICS RESEARCH LABORATORY,
MCGILL UNIVERSITY,
MONTREAL, QUE.

POTENTIAL ENERGY CONSTANTS, ROTATIONAL DISTORTION CONSTANTS, AND THERMODYNAMIC PROPERTIES OF STIBINE

S. SUNDARAM

INTRODUCTION

The present investigation on the stibine molecule is a continuation of a systematic study by Sundaram, Suszek, and Cleveland (1960), of the hydrides of the fifth group elements along with their deuterated and tritiated isotopic forms. A preliminary report, on the investigation of the spectrum of SbH_3, has been made by Smith (1951). It indicated the necessity for accurate high dispersion measurements to identify the individual lines and to treat the vibration–rotation problem in detail. Haynie and Nielsen (1953) have made such dispersion measurements on SbH_3 and SbD_3. They have corrected the band centers for anharmonicities so as to estimate with considerable accuracy the values of the normal frequencies. In the present investigation, the complete quadratic potential energy function for the stibine molecule and its isotopic forms has been determined from the vibrational spectral data.

POTENTIAL ENERGY CONSTANTS

The details, with regard to evaluating uniquely the six symmetrized force constants corresponding to a_1 and e types of vibrations of pyramidal XY_3 type molecules, have been given by Sundaram *et al.* (1960). The same procedure has been followed here using the harmonic wave numbers of SbH_3 and SbD_3 given by Haynie and Nielsen (1953). Using the analytical expressions relating the symmetry force constants (F) to the constants (f) in the quadratic potential energy function, the latter are completely determined. Table I

TABLE I

Vibrational spectral data for SbH_3, SbD_3, and SbT_3

	SbH_3[a]		SbD_3[a]		SbT_3[b]	
	ν	ω	ν	ω	ν	ω
a_1	1891	1989	1359	1409	1118	1153
	782	796	561	568.5	466	469
e	1894	1974	1362	1403	1125	1153
	831	845	593	600	486	490

[a]Reference Haynie and Nielsen (1953).
[b]Wave numbers obtained in the present investigation using the potential energy constants given in Table II (see text).

gives the vibrational wave numbers (ω) used in obtaining the potential energy constants. ν corresponds to the observed wave numbers and ω to those corrected for anharmonicity. The constants are summarized in Table II. The vibrational wave numbers given for SbT_3 in Table I are those calculated in the present study with the constants in Table II. The values of ν for SbT_3 are obtained using the relation

$$\omega_i^* = \nu_i^*(1+x_{ii}\nu_i^*/\nu_i)$$

TABLE II

Potential energy constants for the stibine molecule[a,b]

Stretching and interaction between stretchings (md/Å)		Bending and interaction between bendings (md Å/rad²)		Interaction between bending and stretching (md/rad)	
f_h	2.20857	f_{hh}	0.73975	f_h^{hh}	0.06164
f_h^h	−0.00398	f_{hh}^{hh}	0.01521	$f_h^{hh'}$	0.50895

[a]The notation used here is the same as in reference Sundaram *et al.* (1960).
[b]The number of significant figures is necessary to obtain internal consistency in calculations.

where x_{ii} and ν_i are respectively the anharmonicity factor and the observed frequency for the hydride, and ν_i^* and ω_i^* are the quantities for the tritiated molecule. It has been shown in the previous paper (Sundaram *et al.* 1960) that this assumption is quite reasonable. The constants given in Table II are transferable to molecules of the form $SbXY_2$ (X and Y = H or D or T) belonging to C_s symmetry and the results on these will be given elsewhere.

ROTATIONAL DISTORTION CONSTANTS

The method of Kivelson and Wilson (1952, 1953) has been applied here for the first-order perturbation calculation of the rotational distortion constants for the molecules SbH_3, SbD_3, and SbT_3. The moments of inertia tensor derivatives of the form $[J_{\alpha\beta}^t]_0$ were computed. One needs only $[J_{zz}^t]_0$, $[J_{xx}^t]_0$, and $[J_{xz}^t]_0$ for such symmetric top molecules. The quantities of the form

$$t_{\alpha\beta\gamma\delta} = \sum_{ik} [J_{\alpha\beta}^i]_0 (F^{-1}) [J_{\gamma\delta}^i]_0$$

are obtained using the symmetrized force constant matrix F. Following Wilson (1957), the constants D_J, D_{JK}, and D_K are calculated for the three molecules and these are given in Table III. There are no experimental values available in the literature for a comparison to be made.

TABLE III

Rotational distortion constants for SbH_3, SbD_3, and SbT_3 (Mc/sec)

Molecule	D_J	$-D_{JK}$	D_K
SbH_3	2.4715	4.1586	2.6991
SbD_3	0.6275	1.0572	0.6832
SbT_3	0.2832	0.4759	0.3061

THERMODYNAMIC PROPERTIES

From a knowledge of the accurately determined harmonic vibrational wave numbers, it has been possible to compute the thermodynamic functions of heat content, free energy, entropy, and heat capacity by statistical methods for these molecules. The harmonic wave numbers for SbT_3 are those given in Table I and the results for the thermodynamic properties based on these should be accurate to within 2%. The calculations of all these quantities have

been made for the ideal gaseous state, for 1 atm pressure for a rigid-rotor harmonic-oscillator approximation. The values are summarized in Tables IV to VI, for various temperatures from 100 to 1000° K, including 273.16° K and 298.16° K.

TABLE IV

Heat content, free energy, entropy, and heat capacity for SbH_3[a]

T(°K)	$(H°-E_0°)/T$	$-(F°-E_0°)/T$	$S°$	$C_p°$
100	7.95	38.41	46.36	7.95
200	8.04	43.94	51.98	8.52
273.16	8.29	46.48	54.77	9.46
298.16	8.40	47.21	55.61	9.83
300	8.41	47.26	55.67	9.85
400	8.94	49.75	58.69	11.20
500	9.52	51.81	61.33	12.41
600	10.09	53.59	63.68	13.48
700	10.64	55.19	65.83	14.42
800	11.28	56.74	68.02	15.29
900	11.65	57.99	69.64	15.88
1000	12.11	59.24	71.35	16.43

[a]The values are in cal deg^{-1} mole^{-1} for 1 atm pressure.

TABLE V

Heat content, free energy, entropy, and heat capacity for SbD_3[a]

T(°K)	$(H°-E_0°)/T$	$-(F°-E_0°)/T$	$S°$	$C_p°$
100	7.96	40.53	48.49	8.04
200	8.32	46.12	54.44	9.58
273.16	8.85	48.79	57.64	10.99
298.16	9.05	49.57	58.62	11.45
300	9.06	49.63	58.69	11.47
400	9.88	52.35	62.23	13.12
500	10.66	54.64	65.30	14.46
600	11.39	56.64	68.03	15.52
700	12.04	58.45	70.49	16.36
800	12.63	60.10	72.73	17.00
900	13.13	61.61	74.74	17.48
1000	13.59	63.02	76.61	17.87

[a]The values are in cal deg^{-1} mole^{-1} for 1 atm pressure.

TABLE VI

Heat content, free energy, entropy, and heat capacity for SbT_3[a]

T(°K)	$(H°-E_0°)/T$	$-(F°-E_0°)/T$	$S°$	$C_p°$
100	7.99	41.78	49.77	8.23
200	8.63	47.47	56.10	10.44
273.16	9.34	50.27	59.61	12.05
298.16	9.59	51.10	60.69	12.55
300	9.60	51.16	60.76	12.59
400	10.56	54.04	64.60	14.29
500	11.46	56.51	67.97	15.63
600	12.23	58.66	70.89	16.57
700	12.90	60.60	73.50	17.26
800	13.49	62.37	75.86	17.78
900	14.00	64.01	78.01	18.16
1000	14.42	65.48	79.90	18.45

[a]The values are in cal deg^{-1} mole^{-1} for 1 atm pressure.

Similar calculations of the rotational distortion constants and thermodynamic properties for the partially deuterated and tritiated molecules will be reported elsewhere. Determinations of the mean square amplitudes from the force fields for all these pyramidal XY_3 (X = N, P, As, Sb; Y = H, D, T) type molecules are in progress.

ACKNOWLEDGMENT

This work was aided by a grant from the National Research Council, and the author is thankful for this assistance.

HAYNIE, W. H. and NIELSEN, H. H. 1953. J. Chem. Phys. **21**, 1839.
KIVELSON, D. and WILSON, E. B., JR. 1952. J. Chem. Phys. **20**, 1575.
——— 1953. J. Chem. Phys. **21**, 1229.
SMITH, D. C. 1951. J. Chem. Phys. **19**, 384.
SUNDARAM, S., SUSZEK, F., and CLEVELAND, F. F. 1960. J. Chem. Phys. **32**, 251.
WILSON, E. B., JR. 1957. J. Chem. Phys. **27**, 986.

RECEIVED OCTOBER 17, 1960.
DIVISION OF PHYSICS,
BRITISH COLUMBIA RESEARCH COUNCIL,
UNIVERSITY OF BRITISH COLUMBIA,
VANCOUVER 8, B.C.

SENSITIVITY OF VG-1A IONIZATION GAUGE CALCULATED FROM THE PROBABILITY OF IONIZATION OF GASES

S. N. GHOSH AND B. N. SRIVASTAVA

INTRODUCTION

Among the various gauges used for measuring very low pressures, the ionization gauge is found to be the most satisfactory in the range of 10^{-4} to 10^{-8} mm of mercury. Different types of ionization gauges have been devised by different investigators with a wide range of variation in their construction and sensitivity. One of these gauges is the type VG-1A which is a modified form of the gauge originally devised by Morse and Bowie (1940) and which is manufactured by Consolidated Vacuum Corporation, Rochester, U.S.A. Young and Dushman (1945) have measured the sensitivity of different ionization gauges for inert gases, Hg, H_2, and N_2 and have found that in comparison with other ionization gauges the type VG-1 is the most sensitive. In this paper, the sensitivity of type VG-1A gauge for a large number of gases obtained by Ghosh and Sheridan (1957 and private communication) is compared with those calculated from the probability of ionization of gases by electron bombardments. The gases investigated are inert gases, H_2, N_2, Cl_2, CO, NO, CO_2, and hydrocarbons (CH_4, C_2H_4, C_2H_6, and C_3H_8).

SENSITIVITY OF VG-1A IONIZATION GAUGE FROM ION GAUGE AND McLEOD GAUGE READINGS

In column 2 of Table I, the ratios of VG-1A ionization gauge and McLeod gauge readings for different gases as observed by Ghosh and Sheridan (1957

TABLE I

Sensitivity of VG-1A ionization gauge from ion gauge and McLeod gauge readings

Gases	Observed ratio of ion gauge to McLeod gauge readings	Calculated sensitivity (S) of VG-1A gauge for 1-ma grid current (microampere per micron)	Sensitivity for the gas relative to argon (r)
He	6	3.3	0.13
Ne	3.2	6.3	0.25
A	0.81–0.77	25.3	1.00
Kr	0.50	40.0	1.58
Xe	0.29	68.6	2.72
Air	1.0	20.0	0.79
H_2	1.8	11.1	0.44
N_2	1.0–0.91	21.0	0.83
Cl_2	2.8	7.14	0.28
CO	1.42	14.1	0.56
NO	1.71	11.7	0.46
CO_2	1.35	14.8	0.58
CH_4	1.76	11.3	0.45
C_2H_4	1.20	16.7	0.66
C_2H_6	2.3	8.7	0.34
C_3H_8	2.2	9.1	0.36

and private communication) are given. (The ionization gauge was calibrated against the McLeod gauge for air.) The connection of the ionization gauge is of the type (b) given by Dushman (1949), so that the electrons are collected by the grid and the ions to the plate. Since a good average value of the sensitivity for VG-1A ionization gauge below 1 micron is 20 microamperes per micron per ma current (data sheet for the ionization gauge tube type VG-1A, Consolidated Vacuum Corporation, Rochester, U.S.A.), the sensitivity of this gauge for other gases can be obtained by dividing 20 by the values given in column 2; the results are shown in column 3. The values of r (sensitivity of the gauge for a particular gas relative to argon) are given in column 4.

SENSITIVITY OF VG-1A IONIZATION GAUGE FROM THE PROBABILITY OF IONIZATION OF GASES

The sensitivity of the VG-1A ionization gauge can also be obtained from the probability of ionization of gases by electron bombardments (Reynolds 1931) and is given below.

In Fig. 1 the probability of ionization for different gases as a function of electron velocity, obtained by various investigators (Tate and Smith 1932; Smith 1930; Compton and Van Voorhis 1925, 1926; Jesse 1925; and Hughes and Klein 1924) is given. Tate and Smith (1932) and Smith (1930) have obtained data at 0° C, while Compton and Van Voorhis (1925, 1926) derived results at 25° C. Other investigators (Jesse 1925 and Hughes and Klein 1924) have probably made observations at room temperature. In plotting the above probability curves no temperature correction has been made.

It should be noted that in the experimental determination of the probability of ionization of gases per cm path by electron bombardments, the electrons of constant velocity traverse the collision chamber only once. On the other hand,

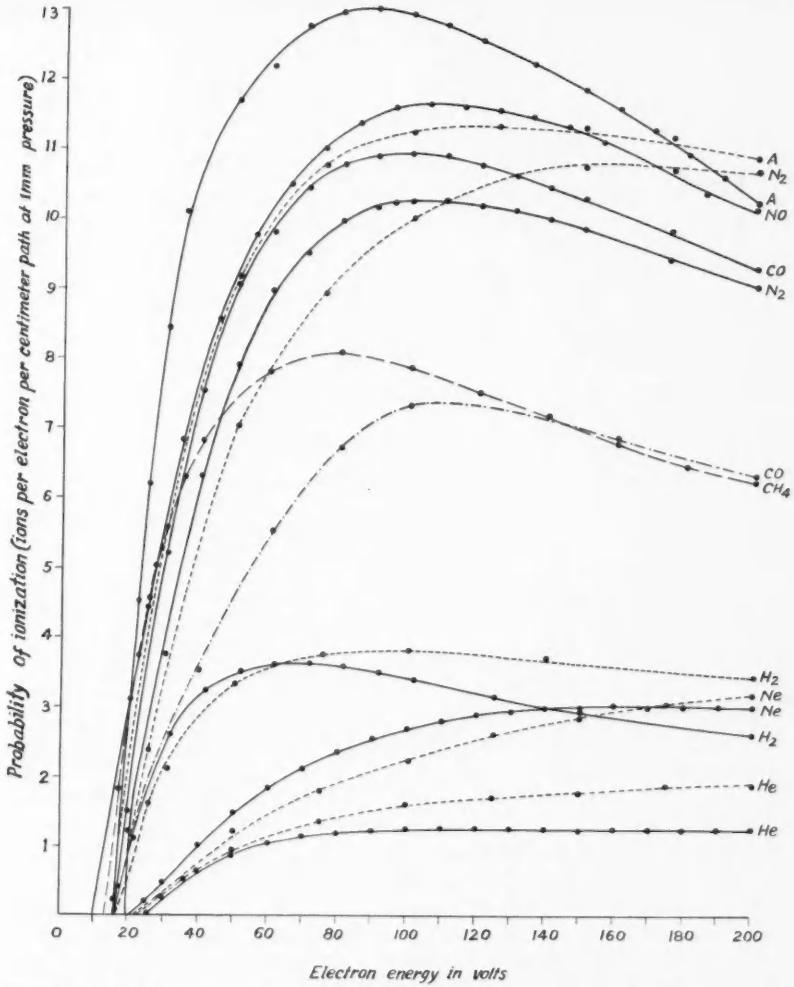

FIG. 1. The probability of ionization of gases as a function of electron energy. Full line curves are obtained by Tate and Smith (1932) and Smith (1930); dash curves by Compton and Van Voorhis (1925, 1926); dot and dash curve by Jesse (1925), and long dash curve by Hughes and Klein (1924).

in an ionization gauge an electron is accelerated in a varying field and makes at least one round trip from grid to collector and then back to the grid.

Assuming the electrodes are concentric cylinders and radial fields linear, the field through which the electrons move and the distance traversed by them are given in Fig. 2. The dimensions and normal operating voltages of VG-1A ionization gauge as given by the manufacturer are shown below:

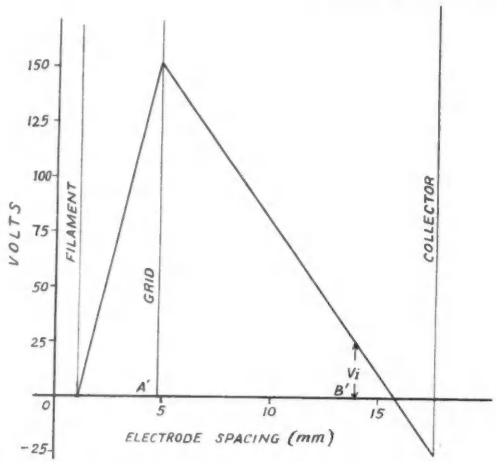

FIG. 2. Field distribution inside a VG-1A ionization gauge.

Inner diameter of the collector	= 1.375 in.
Diameter of the grid	= 9.53 mm
Filament diameter	= 2.1 mm
Filament voltage	= 3.0 to 7.5 v
Grid voltage	= +150 v
Grid current	= 1 ma
Collector voltage	= −25 v

Most of the ions are produced in the space $A'B'$ because the electrons after passing through the grid acquire sufficient energy to ionize the gas. (The ions formed between grid and cathode are collected by the filament and do not affect the ionic current.) The voltage at the plane B' corresponds to the ionization potential of the enclosed gas. As already mentioned, the effective distance for ionization of the gas inside the ionization gauge by an electron is at least a distance of 2 $A'B'$ or some multiples of it.

The amount of ionization of the gas by an electron in the space $A'B'$ can be determined by obtaining the area included by the ionization probability curve between ionization potential and maximum accelerating grid voltage E_g (150 ev), and then by multiplying the result by the distance $A'B'$. In column 2 of Table II, the area of the integrated curve for 1 ma electron (grid) current reduced to 1 micron pressure is given. The distance $A'B'$ for different gases is given in column 3. In column 4, the ionic (plate) current i_p' for 1-ma grid current is obtained by multiplying the values in column 2 and 3. In column 5 the average values of i_p' obtained by different investigators are given. In column 6, the values of i_p obtained by Ghosh and Sheridan (1957 and private communication) which are the sensitivity (S) of the gauge for the different gases are given. The ratio $\alpha = i_p/I_p'$ which gives the possible number of multiples of $A'B'$ that an electron makes before it is captured by the grid

TABLE II

Sensitivity of VG-1A ion gauge from the probability of the ionization of gases

Gases	Area of integration probability curve up to 150 ev for 1-ma electron current	Distance $A'B'$ (cm)	Calculated ionic current i_p' (μa)	Average i_p' (μa)	Ionic current measured by Ghosh and Sheridan (μa)	$\alpha = i_p/i_p'$	Calculated S for VG-1A ion gauge (μa per micron)	S of VG-1 ion gauge given by Dushman (μa/micron)
He (C.V.)	1.82		1.64					
(Smith)	1.32	0.903	1.19	1.41	3.33	2.4	2.82	2.88
Ne (C.V.)	2.25		2.14					
(Smith)	2.80	0.951	2.66	2.40	6.25	2.6	4.80	4.65
A (C.V.)	12.85		12.4					
(Smith)	15.50	0.975	15.1	13.75	25.3	1.8	27.50	22.6
H_2 (C.V.)	4.22		4.22					
(Smith)	4.02	1.00	4.02	4.12	11.0	2.7	8.24	8.6
N_2 (C.V.)	10.68		11.45					
(Smith)	11.90	0.975	11.60	11.02	21.0	1.9	22.04	18.2
CO (T.S.)	12.38		12.6					
(Jesse)	7.61	1.02	7.76	10.18	14.1	1.4	20.36	—
NO (T.S.)	13.2	0.975	12.9	12.9	11.7	0.9	25.80	—
CH_4 (H.K.)	9.21	0.987	9.09	9.09	11.3	1.3	18.18	—

NOTE: C.V. refers to Compton and Van Voorhis (1925, 1926); Smith refers to (1930); T.S. refers to Tate and Smith (1932); and H.K. refers to Hughes and Klein (1924).

is shown in column 7. Except in the case of CO, NO, and CH_4 the calculated value of α comes out to be about 2, its variation is from 1.8 to 2.7. However, since the number of trips which an electron makes between grid and collector is an even multiple of $A'B'$, it follows that in most cases the electron makes only one round trip before it is captured by the grid. The calculated values of the sensitivity of VG-1A gauge for different gases from the ionization probability curve obtained by multiplying the average value of i_p' by 2 are given in column 8 of Table II. It is to be noted from the last column of Table II that Dushman's (1949, page 350) value for the sensitivity of VG-1 ionization gauge is slightly lower.

The values of r which, as shown before, is the ratio of S for the gas to its value for argon were determined previously by Young and Dushman (1945), Langmuir and Jones (1928), and Reynolds (1931). These values and the values obtained by Ghosh and Sheridan (1957 and private communication) are given in Table III. In columns 6 and 7 of this table, the values of r calculated from the ionization probability curve and those given by the manufacturer are shown.

TABLE III

Comparison of values of r given by different investigators

Gases	r (L.J.) at 100 ev	r (Y.D.) at 150 ev	r (R.) at 125 ev and 250 ev	r (G.S.) at 150 ev	r from probability of ionization curve up to 150 ev	r (M.)
He	0.14	0.13	.10–.13	0.13	.08–.14	0.09
Ne	0.21	0.21	.12–.24	0.25	.17–.18	—
A	1.00	1.00	1.00	1.00	1.00	1.00
Kr	—	1.56	—	1.56	—	—
Xe	—	2.29	—	2.27	—	—
H_2	0.34	0.39	—	0.44	.26–.34	0.28
N_2	0.90	0.84	.73–.81	0.83	.77–.83	0.7
CO	—	—	—	0.56	.73	0.7
NO	—	—	0.56	0.46	.94	—
CO_2	—	—	—	0.58	—	0.74
CH_4	—	—	—	0.45	.68	—

NOTE: L.J. Langmuir and Jones (1928).
Y.D. Young and Dushman (1945).
R. Reynolds (1931).
G.S. Ghosh and Sheridan (1957 and private communication).
M. Manufacturer (Consolidated Vacuum Corporation, Rochester, U.S.A.).

DISCUSSION

It is clear from Table III that for He, Ne, A, H_2, and N_2 there is a fair agreement between the values of r calculated from the ionization probability curves and those measured by different investigators. The values of r obtained by Ghosh and Sheridan (1957 and private communication) are roughly the same as those obtained by Young and Dushman (1945).

In the data manual supplied by the manufacturer it is remarked that for H_2 and CO_2, the gauge was influenced by the gettering action (data sheet for the ionization gauge tube type VG-1A, Consolidated Vacuum Corporation, Rochester, U.S.A.), and hence the sensitivity given by the manufacturer can not

be relied on. It is difficult to measure the pressure of these gases with an ionization gauge because these gases react chemically or electrochemically with the cathode or other metal elements of the gauge. Also, the McLeod gauge is not sensitive enough to give correct readings for compressible gases like CO, NO, and CO_2 at very low pressures. In the case of hydrocarbons, the vapor reacts with tungsten filament forming carbides thereby affecting their resistance as well as their emissivity.

COMPTON, K. T. and VAN VOORHIS, C. C. 1925. Phys. Rev. **26**, 436.
——— 1926. Phys. Rev. **27**, 724.
DUSHMAN, S. 1949. Scientific foundation of vacuum technique, 2nd ed. (John Wiley & Sons, New York), pp. 334, 350.
GHOSH, S. N. and SHERIDAN, W. F. 1957. J. Chem. Phys. **26**, 480.
——— Private communication.
HUGHES, A. and KLEIN, E. 1924. Phys. Rev. **23**, 450.
JESSE, W. P. 1925. Phys. Rev. **26**, 208.
LANGMUIR, I. and JONES, H. A. 1928. Phys. Rev. **31**, 357.
MORSE, R. S. and BOWIE, R. M. 1940. Rev. Sci. Instr. **11**, 91.
REYNOLDS, N. B. 1931. Physics, **1**, 182.
SMITH, P. T. 1930. Phys. Rev. **36**, 1924.
TATE, J. and SMITH, P. T. 1932. Phys. Rev. **39**, 270.
YOUNG, A. H. and DUSHMAN, S. 1945. Phys. Rev. **68**, 274.

RECEIVED SEPTEMBER 28, 1960.
J. K. INSTITUTE OF APPLIED PHYSICS,
UNIVERSITY OF ALLAHABAD,
ALLAHABAD, INDIA.

LETTERS TO THE EDITOR

Under this heading brief reports of important discoveries in physics may be published. These reports should not exceed 600 words and, for any issue, should be submitted not later than six weeks previous to the first day of the month of issue. No proof will be sent to the authors.

Frequency Measurement of Standard Frequency Transmissions[1, 2]

Measurements are made at Ottawa, Canada, using N.R.C. caesium-beam frequency resonator as reference standard (with an assumed frequency of 9 192 631 770 c.p.s.). Frequency deviations from nominal are quoted in parts per 10^{10}. A negative sign indicates that the frequency is below nominal.

Date, November 1960	MSF, 60 kc/s	GBR, 16 kc/s		WWVB, 60 kc/s
		7-hour average*	24-hour average	
1	N.M.	N.M.	N.M.	N.M.
2	N.M.	N.M.	N.M.	N.M.
3	N.M.	N.M.	N.M.	N.M.
4	N.M.	N.M.	N.M.	N.M.
5	N.M.	N.M.	N.M.	N.M.
6	N.M.	N.M.	N.M.	N.M.
7	N.M.	N.M.	N.M.	N.M.
8	N.M.	N.M.	N.M.	N.M.
9	N.M.	N.M.	N.M.	N.M.
10	N.M.	N.M.	N.M.	N.M.
11	N.M.	N.M.	N.M.	N.M.
12	−154	−167	−166	N.M.
13	−153	−162	−164	N.M.
14	−160	−165	−167	N.M.
15	N.M.	N.M.	N.M.	N.M.
16	−180	−178	N.M.	N.M.
17	−165	−172	−176	N.M.
18	−164	−166	−165	−151
19	−158	−163	−164	N.M.
20	−153	−161	−159	N.M.
21	−162	−155	−159	−148
22	−159	−159	−160	−148
23	−153	−158	−157	−149
24	−157	−159	−157	−147
25	N.M.	−153	−154	−149
26	N.M.	−151	−154	N.M.
27	N.M.	−154	−153	N.M.
28	−157	−148	−150	−147
29	−156	−148	−153	−148
30	−148	−152	−150	−146
Average	−159	−160	−159	−148
Midmonthly mean of WWV	−149			

NOTE: N.M. no measurement.
*Time of observations: 00.00 to 05.30 and 22.30 to 24.00 U.T.

RECEIVED DECEMBER 16, 1960.
DIVISION OF APPLIED PHYSICS,
NATIONAL RESEARCH COUNCIL,
OTTAWA, CANADA.

S. N. KALRA

[1]Issued as N.R.C. No. 6125.
[2]Cf. Kalra, S.N. 1959. Can. J. Phys. *37*, 1328.

NOTES TO CONTRIBUTORS

Canadian Journal of Physics

MANUSCRIPTS

General.—Manuscripts, in English or French, should be typewritten, double spaced, on paper 8½×11 in. **The original and one copy are to be submitted.** Tables and captions for the figures should be placed at the end of the manuscript. Every sheet of the manuscript should be numbered. Style, arrangement, spelling, and abbreviations should conform to the usage of recent numbers of this journal. Greek letters or unusual signs should be written plainly or explained by marginal notes. Characters to be set in boldface type should be indicated by a wavy line below each character. Superscripts and subscripts must be legible and carefully placed. Manuscripts and illustrations should be carefully checked before they are submitted. Authors will be charged for unnecessary deviations from the usual format and for changes made in the proof that are considered excessive or unnecessary.

Abstract.—An abstract of not more than about 200 words, indicating the scope of the work and the principal findings, is required, except in Notes.

References.—References should be listed **alphabetically by authors' names,** unnumbered, and typed after the text. The form of the citations should be that used in current issues of this journal; in references to papers in periodicals, titles should not be given and only initial page numbers are required. The names of periodicals should be abbreviated in the form given in the most recent *List of Periodicals Abstracted by Chemical Abstracts.* All citations should be checked with the original articles and each one referred to in the text by the authors' names and the year.

Tables.—Tables should be numbered in roman numerals and each table referred to in the text. Titles should always be given but should be brief; column headings should be brief and descriptive matter in the tables confined to a minimum. Vertical rules should not be used. Numerous small tables should be avoided.

ILLUSTRATIONS

General.—All figures (including each figure of the plates) should be numbered consecutively from 1 up, in arabic numerals, and each figure referred to in the text. The author's name, title of the paper, and figure number should be written in the lower left corner of the sheets on which the illustrations appear. Captions should not be written on the illustrations.

Line drawings.—Drawings should be carefully made with India ink on white drawing paper, blue tracing linen, or co-ordinate paper ruled in blue only; any co-ordinate lines that are to appear in the reproduction should be ruled in black ink. Paper ruled in green, yellow, or red should not be used. All lines must be of sufficient thickness to reproduce well. Decimal points, periods, and stippled dots must be solid black circles large enough to be reduced if necessary. Letters and numerals should be neatly made, preferably with a stencil (**do NOT use typewriting**) and be of such size that the smallest lettering will be not less than 1 mm high when the figure is reduced to a suitable size. Many drawings are made too large; originals should not be more than 2 or 3 times the size of the desired reproduction. Whenever possible two or more drawings should be grouped to reduce the number of cuts required. In such groups of drawings, or in large drawings, full use of the space available should be made; the ratio of height to width should conform to that of a journal page (4½×7½ in.), but allowance must be made for the captions. **The original drawings and one set of clear copies (e.g. small photographs) are to be submitted.**

Photographs.—Prints should be made on glossy paper, with strong contrasts. They should be trimmed so that essential features only are shown and mounted carefully, with rubber cement, on white cardboard, with no space between those arranged in groups. In mounting, full use of the space available should be made. **Photographs are to be submitted in duplicate;** if they are to be reproduced in groups one set should be mounted, the duplicate set unmounted.

REPRINTS

A total of 100 reprints of each paper, without covers, are supplied free. Additional reprints, with or without covers, may be purchased at the time of publication.

Charges for reprints are based on the number of printed pages, which may be calculated approximately by multiplying by 0.6 the number of manuscript pages (double-spaced typewritten sheets, 8½×11 in.) and including the space occupied by illustrations. Prices and instructions for ordering reprints are sent out with the galley proof.

Contents

Printed in Canada *by* University of Toronto Press